CFD STUDY AND MODELLING OF INLET JET MIXING IN SOLAR DHWS

COMPUTATIONAL FLUID DYNAMICS STUDY AND MODELLING OF INLET JET MIXING IN SOLAR DOMESTIC HOT WATER TANK SYSTEMS

BY

DANISH JALAL NIZAMI, B.E, (MECH. ENG.)

A Thesis

Submitted to the school of Graduate Studies

In Partial Fulfillment of the Requirements

For the Degree

Master of Applied Science

McMaster University

MASTER OF APPLIED SCIENCE (2010) McMaster University

(Mechanical Engineering) Hamilton, Ontario

TITLE: Computational Fluid Dynamics Study and Modelling of Inlet Jet Mixing in Solar Domestic Hot Water Tank Systems

AUTHOR: Danish Jalal Nizami, B.E in Mechanical Engineering (Bangalore University, India)

SUPERVISORS: Professor Dr. Marilyn F. Lightstone

NUMBER OF PAGES: xiii, 155

ABSTRACT

Thermal stratification in solar energy storage tanks plays an important role in enhancing the performance of solar domestic hot water (SDHW) system. The mixing that occurs when hot fluid from the solar collector enters the top of the tank is detrimental to the stratification. Mathematical models that are used for system analysis must thus be able to capture the effects of this inlet jet mixing in order to accurately predict system performance. This thesis presents a Computational Fluid Dynamics (CFD) study of the heat transfer and fluid flow in the thermal storage tank (TST) of a solar domestic hot water system employing a vertical inlet jet geometry. The focus of the thesis is on the studying the effects of inlet jet mixing on the thermal stratification in the tank. Predictions of transient temperature profiles were assessed by comparing to experimental data from the literature. CFD was then used to study how the predicted mixing in the TST was affected by parameters such as the inlet velocity and temperature, pipe diameter and the selected turbulence model. From this study of the mixing, a one dimensional empirical model was developed to predict the temperature distribution inside the TST. The model was found to provide improved predictions of the transient axial temperature distribution in comparison to the plug-flow model which is commonly used in the broader system analysis codes.

Acknowledgement

I would like to thank Dr. Marilyn F. Lightstone for her supervision and support. The financial support of Solar Building Research Network and Natural Resource Canada are also acknowledged.

DEDICATED TO THE LOVING MEMORY OF MY DEAR FATHER

TABLE OF CONTENTS

LIST OF FIGURES

LIST OF TABLES

NOMENCLATURE

a_1	constant of the SST model
A	area of cross-section, m^2
C	heat capacitance ratio
C_μ	constant of the k-ε model
$C_{\varepsilon 1}$	constant of the k-ε model
$C_{\varepsilon 2}$	constant of the k-ε model
C_p	specific heat capacity, J/kg-K
d	inlet pipe diameter, m
F_1	first blending function of the SST model
F_2	second blending function of the SST model
g	acceleration of gravity, m/s^2
h	length, m
k	turbulence kinetic energy, m^2/s^2
$\dot{m}$	mass flow rate, kg/s
n	current time step
$\overline{p}$	mean pressure, Pa
P	pressure, Pa

Pr	Prandtl number of fluid
P_k	production term in the transport equation of turbulence kinetic energy
P_{kb}	buoyancy production term
P_ω	production term in the transport equation of turbulence eddy frequency
q	heat transfer, W/s
Q_s	volume flow rate, l/min
Re	Reynolds number
Ri	Richardson number
S_M	source in momentum equation
S_E	source in energy equation
$S_{M,buoy}$	buoyancy source term in momentum equation
t	time, s
T	temperature, K
T'	temperature fluctuation, K
U_{inst}	instantaneous velocity, m/s
$\overline{U}$	mean velocity, m/s
u	velocity fluctuation, m/s

$\bar{u}$ mean velocity fluctuation, m/s

x Cartesian coordinate

y Cartesian coordinate

z Cartesian coordinate

Greek Symbols

α constant of the k-ω model, in Chapter 5, thermal diffusivity, m^2/s

α' eddy diffusivity, m^2/s

β constant of the k-ω model, the SST model and in Eq (3.6), thermal expansion coefficient, K^{-1}

β^* constant of the original k-ω and transformed k-ε model

Γ thermal conductivity, W/K-m

γ constant of the SST model

Δ denotes difference when used as suffix

δ_{ij} Kronecker delta

δ_1 region and extent in meters of the region shown in figure 5.1

δ_2 region and extent in meters of the region shown in figure 5.1

δ_3 region and extent in meters of the region shown in figure 5.1

δ_4 region and extent in meters of the region shown in figure 5.1

ε In chapter 3, turbulence eddy dissipation, m^2/s^3 and elsewhere heat exchanger effectiveness

μ dynamic viscosity of the fluid, Pa-s

μ_t dynamic turbulence eddy viscosity, Pa-s

μ_t^H thermal eddy diffusivity, Pa-s

ν kinematic viscosity of the fluid, m^2/s

ν_t kinematic turbulence eddy viscosity, m^2/s

ε heat exchanger effectiveness

ρ density of fluid, Kg/m^3

σ_k constant of the SST model, the k-ε model, the k-ω model

σ_ω constant of the SST model and the k-ω model

τ_{ij} Reynolds stress/ SGS stress tensor, m^2/s^2

Ω vorticity, 1/s

ω turbulence eddy frequency, 1/s

Superscripts and Subscripts

c collector loop

ent entrainment

i i-coordinate

in	tank inlet
ini	initial
j	j-coordinate
m	modified
r	tank region considered in the Richardson number
p	out of the plume
pi	pipe
ref	reference
s	storage loop
t	tank and in chapter 3 turbulence
x	heat exchanger
xin	heat exchanger inlet
xout	heat exchanger outlet

CHAPTER 1

Solar Domestic Hot Water Tank Systems

1.1 Background

The high cost involved in conventional energy resources and the fact that most of them are non-renewable, provides motivation for the use of non-conventional energy resources. Solar energy is a renewable energy resource which could be further utilized in areas such as domestic hot water heating. The problem of irregular availability associated with solar energy necessitates the use of an efficient energy storage system. There are various ways in which energy can be stored but sensible heat storage is the most common form because of its simplicity and cost effectiveness.

This study deals with sensible heat storage in SDHW systems. The major focus of this thesis is on modeling of SDHW systems with a vertical inlet jet coupled with a natural convection heat exchanger (NCHE).

1.2 Classification of SDHW Systems

A simple SDHW system, as shown in Figure 1.1, consists of a solar collector, pump, storage tank, controller and piping. The solar collector collects the solar irradiation and transfers the heat to the working fluid in the collector loop. A controller functions as an operator of the pump depending on the difference between the temperature of the fluid entering and exiting the collector. The energy collected by the collector fluid is transferred to the TST. When hot water is required by the household, the fluid from the

TST is transported to the auxiliary heater, where it is further heated to meet the temperature requirement of the load.

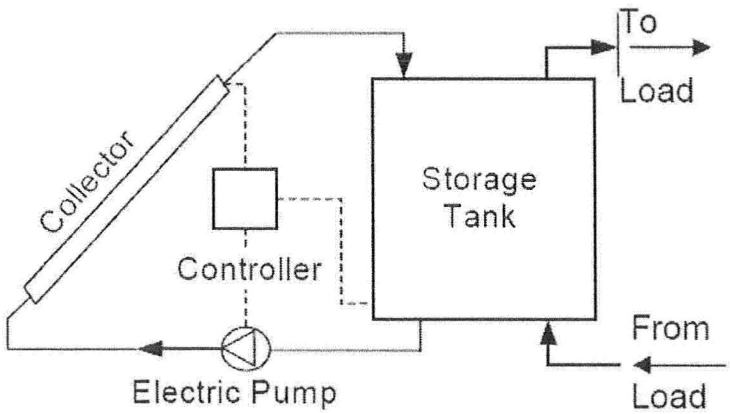

Figure 1.1: SDHW System [1].

For freeze protection purposes, a glycol/water mixture may act as the working fluid in the collector loop, thus necessitating the use of a heat exchanger between the collector loop and the storage tank.

Various kinds of SDHW systems have been developed and introduced in the last century. These systems are generally classified as passive or active as shown in Figure 1.2. The systems in which solar collectors are positioned on the top of the roof and the TST is located below the collectors, usually in the basement of the house are termed as active systems. Figure 1.2 (a) depicts a typical active system. The working fluid is pumped depending on the availability of solar irradiation. Such systems are generally designed for cold countries, since the placement of TST in a closed environment avoids energy losses. The systems in which TST is placed above the solar collectors are termed as passive systems, as shown in Figure 1.2 (b). This configuration uses buoyancy forces to circulate the fluid through the system. Such systems have a major market in warm countries, where losses to the environment are not excessive. Moreover, passive systems are simple and more efficient since they are not dependant on an external power source.

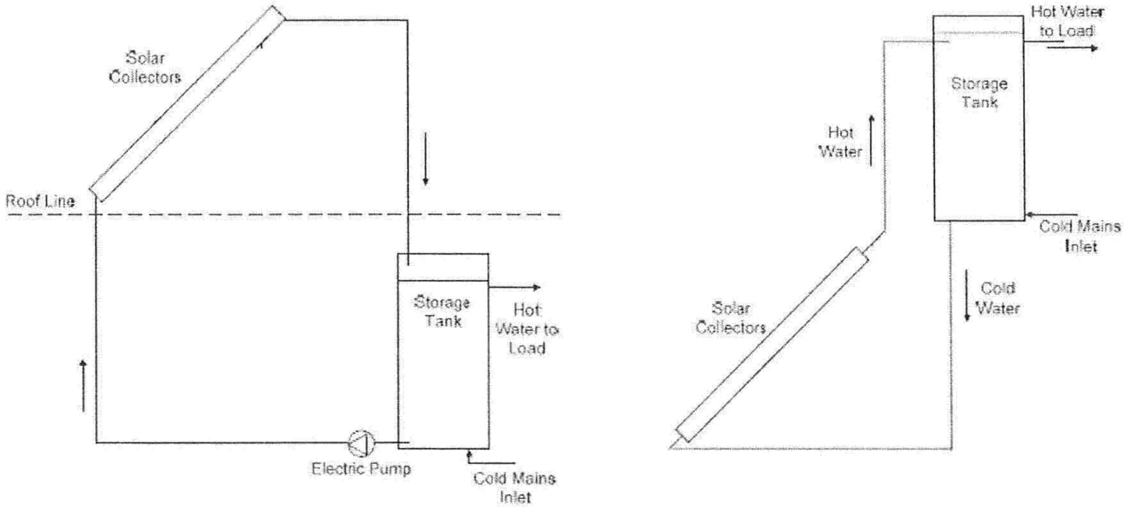

(a) (b)

Figure 1.2: (a) Active System, (b) Passive System [1].

SDHW systems can also be classified based on the circulation loops. The systems shown in Figure 1.2 depict typical direct systems. In such systems, water is circulated through the collector and is stored in the TST for later use by the household. In contrast, systems in which the fluids in the collector loop and the TST loop are separated by the use of a heat exchanger are termed indirect systems. Figure 1.3 shows typical indirect systems. The use of indirect systems is very common in countries where the temperature drops below the water freezing point and the fluid used in the collector loop has sub a zero freezing temperature.

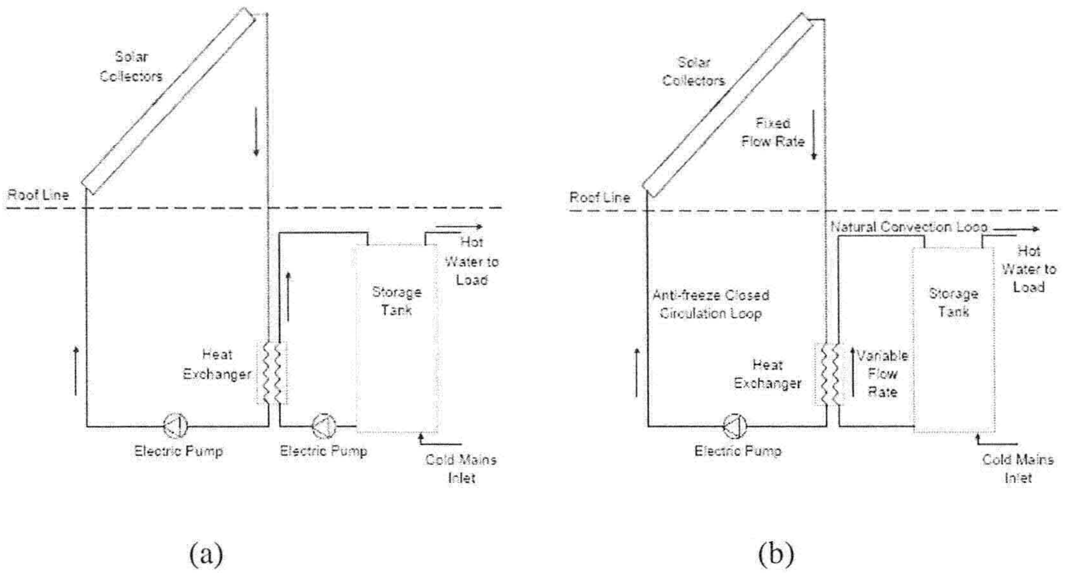

Figure 1.3: Indirect Systems with (a) Forced Flow, (b) Thermosyphon Flow [1].

A range of heat exchangers can be used in indirect systems. These include: immersed coil exchanger systems, mantle heat exchanger systems and side-arm heat exchanger systems. A detailed review has been presented by Han *et al* [2]. The current research, however, focuses on systems using side-arm heat exchangers, as depicted in Figure 1.3. The indirect systems with forced convection in both loops (Figure 1.3 (a)) are the most commonly used systems in North America. The collector fluid generally employed in such systems is a propylene glycol/water mixture. The advantages of these systems, such as low cost, lower maintenance and easy retrofitting, have been discussed throughout the literature. Further research on the side arm heat exchanger systems has led to more advanced systems: SDHW with natural convection heat exchanger (NCHE), as shown in Figure 1.3 (b). The pump in the storage loop is removed to take the advantage of flow arising from density differences between the hot and cold fluid. The incorporation of the thermosyphon effect makes the system more cost effective in terms of power consumption, maintenance cost and retrofitting charges.

The flow in the TST loop of the SDHW system with a NCHE occurs when the shear pressure drop is less than or equal to the net hydrostatic pressure drop in the TST loop. During operation, the shear pressure drop increases and reduces the flow until a balance is reached. However, as the tank is heated, the net hydrostatic pressure will reduce resulting in reduced flow across the heat exchanger. SDHW systems with a NCHE are the subject of numerous studies and different ways to characterize the performance of NCHE have been proposed. A review on such systems can be found in the work of Purdy *et al.* [3], Lin *et al.* [4], Cruickshank and Harrison [5] and Nizami *et al.* [6]. The models presented by Cruickshank and Harrison [5] have been used to develop the flow in this study and will be discussed in Chapter 4.

1.3 Outline of Thesis

This thesis is divided into four sections: a review of the literature, an evaluation of the CFD methodology and turbulence modeling, the numerical study of SDHW tank systems and the development of the system models.

Chapter 2 presents the literature review on the research on SDHW systems. The effect of stratification in TST is presented. Various parameters affecting stratification and the two dimensional and one dimensional numerical modeling on TST are discussed.

Chapter 3 presents the conservation equations which are involved in the CFD modeling of TST. The various boundary conditions involved in this study are also presented along with important aspects of the numerical discretization of the conservation equations.

Chapter 4 presents the CFD study of the SDHW system. The effect of various CFD parameters on the vertical inlet jet is discussed.

Chapter 5 presents the effect of various physical parameters on the vertical inlet jet. Empirical models for characterization of the vertical inlet jet and the validation of the proposed empirical models with the CFD results are also presented.

Chapter 6 presents the final conclusion and recommendations for future work.

CHAPTER 2

Literature Review

2.1 Overview

In Chapter 1, the TST system was introduced. The performance of TST systems have been extensively investigated experimentally and numerically in the last century. In this chapter the parameters affecting the performance of thermal storage systems are discussed and the results of various experimental and numerical studies are highlighted.

2.2 Thermal Stratification in a TST

Thermal stratification is the temperature gradient in the TST which allows the separation of fluid at different temperatures demarcated by an intermediate region or thermocline. The definition of stratification in TST is quite broad and includes the conditions shown in Figure 2.1. The tank shown in figure 2.1 (a) represents a highly stratified tank, Figure 2.1 (b) represents a moderately stratified tank and Figure 2.1 (c) represents a fully mixed tank or the tank with no stratification. All three tanks contain the same amount of energy.

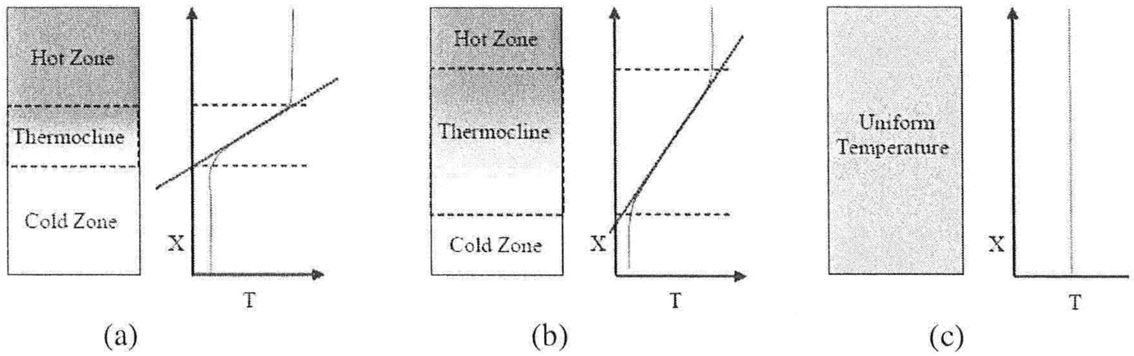

Figure 2.1: Stratification [1].

The effect of stratification on the performance of TST has been a subject of various studies in the last forty years. Holland and Lightstone [7] showed that the solar fraction (F_r) of the TST systems can be improved up to 37% for fully stratified tank when compared to the fully mixed tank [7], figure 2.2. The increase in the performance was attributed to low flow rate at inlet. The low flow rate at inlet reduces the mixing caused by the inlet jet momentum and hence better stratification. Macroscopically, stratification separates hot and cold fluid in the tank thus allowing the hot water from the top of the tank to be transported to the auxiliary unit, where it requires less energy to reach the load temperature. Also, cold water from the stratified tank is transported to the collector; hence increasing the efficiency of the collector.

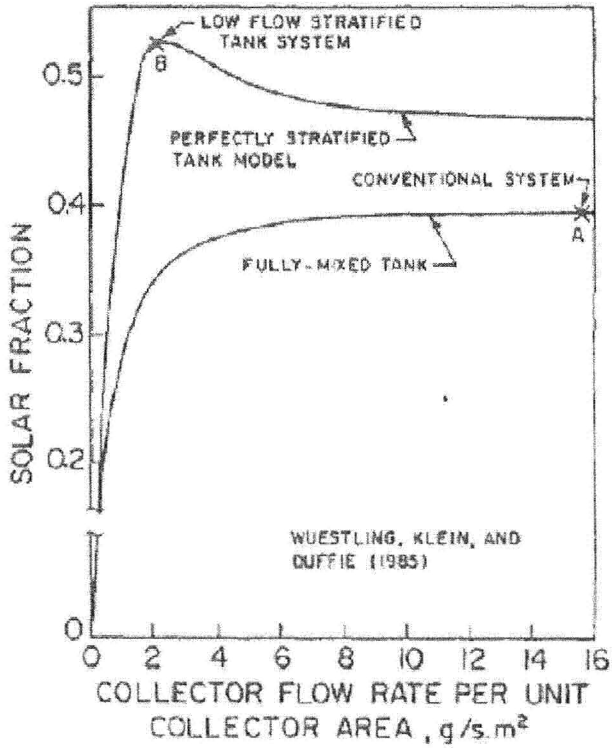

Figure 2.2: Annual Solar Fraction vs. Collector Flow rate [7].

The existing performance indices used to characterize the performance of the stratified thermal storage tanks are generally based on the first and second law of thermodynamics. However, a widely accepted basis to analyze the performance of thermal storage tanks does not exist [8]. Rosen [8] used exergy analysis to show that the energy availability increased with increased stratification. He concluded that stratification improves the TST performance and emphasized the use of exergy analysis for comparing and improving the efficiencies of TST. Later, Panthalookaran *et al.* [9] pointed out the disputes on the definition of efficiencies in the scientific community, which were based on exergy analysis and stated that emphasizing that the quality of the stored energy (second law of thermodynamics) may conflict with the better extraction efficiency (first law of thermodynamics) and would result in the reduction of the net effectiveness of the system. Hence, he combined the two laws of thermodynamics and proposed a storage evaluation number; defined separately for charging and discharging, as a function of entropy generation in real, stratified and mixed storage tanks (second law of thermodynamics) and change in the energy level in the real and ideal systems (first law of thermodynamics). A similar comment was made by Cabeza *et al.* [10] and Cruickshank [1] on the failure of the 2nd law based efficiency: the efficiency was not sensitive to the inlet mass flow rate. Cabeza *et al.* [10] also mentioned that at high discharge flow rates, the 2nd law of thermodynamics based efficiency showed high stratification which is contradictory to the stratification phenomena. Various proposed forms of performance indices are discussed later in this chapter in context to the discussion.

2.3 Factors Affecting Stratification

The primary factors which affect stratification in thermal storage tanks are:

- Heat losses to environment.
- Heat conduction within the water itself and through the walls.
- Inlet jet mixing.

Out of all the factors mentioned above, inlet jet mixing is a major cause of destratification in TST. Various techniques such as the use of baffles, manifolds and inlet diffusers have been employed and studied to counter the effect of the inlet mixing. The following discussion highlights the various studies which have been conducted to determine the factors which affect the stratification.

The important dimensionless numbers which are generally associated with the characterization of the performance of TST systems are Reynolds number, Grashof number, Richardson number, Froude number, Peclet number, Biot number and Fourier number. The scales: length (l), velocity (V), temperature (ΔT), and time (t) used by various authors to calculate dimensionless groups are different and therefore only the general definitions of the dimensionless are provided here. Equations for these dimensionless groups are given below. The Reynolds number compares the effect of inertia and viscous force in a convective flow, while in the buoyant flow; Grashof number compares the buoyancy force and the viscous force in the fluid element. The Richardson number compares the buoyancy force and the inertia force on the fluid element. The Peclet number compares the convection and the diffusion of the heat in the fluid element. The Froude number is inverse square root of the Richardson number.

Fourier number is the dimensionless time. It characterizes the heat conduction through the fluid element and compares the heat conduction rate to the energy stored in the element. Biot number compares the heat resistance inside of and at the surface of the body.

$$Re = \frac{\rho V l}{\mu} \tag{2.1}$$

$$Gr = \frac{g\beta(\Delta T)L^3}{\nu^2} \tag{2.2}$$

$$Ri = \frac{Gr}{\mathrm{Re}^2} \tag{2.3}$$

$$Fr = \sqrt{\frac{1}{Ri}} \tag{2.4}$$

$$Pe_L = \frac{lV}{\alpha} \tag{2.5}$$

$$Bi = \frac{hl}{\Gamma} \tag{2.6}$$

$$Fo = \frac{\alpha t}{l^2} \tag{2.7}$$

Lavan and Thomson [11] studied experimentally the discharging process of TST with a horizontal inlet. They stated that to promote stratification, the inlet hot water should always be injected at the top of the tank, while the position of the outlet does not affect stratification. The extraction efficiency, which they defined based on the first law of thermodynamics as the ratio of the energy extracted to the total energy of the thermal system, was determined as a function of the Reynolds number based on the tank diameter, the Grashof number based on tank diameter and the height to diameter ratio of the TST. They stated that with increasing length to diameter ratio of the TST, the achieved stratification also increases. They also mentioned that no mixing occurs when the extraction efficiency was above 45-50 and they reported improvement in stratification with the use of horizontal distributor.

Sliwinski *et al.* [12] performed an experimental study on TST with horizontal inlet. They accounted for stratification in terms of mixing length and expressed it as a function of the Richardson number; which was defined based on the inlet velocity, the tank height and temperature difference between the initial temperature in the tank and temperature of the fluid at the inlet. They also proposed a relationship for the sharpness of the thermocline with the Richardson number and the Peclet number; defined based on the tank diameter. They concluded that for thermal stratification to occur the length to diameter ratio of the TST should be more than 2 and the Richardson number should be above 0.24.

Zurigat *et al.* [13, 14] studied different inlet configurations: radial diffuser, side inlet with perforated baffle and impingement (inlet pipe directed towards the top wall) inlet. They concluded that mixing is negligible for all the inlet configurations mentioned above when the Richardson number is above than 3.5. The definition of the Richardson number was similar to that used by Sliwinski *et al.* [12]. For Richardson number below 3.5 the best performance was obtained with the impingement type inlet. Later, however, Ghajar and Zurigat [15] found numerically that the effect of mixing is negligible for Richardson numbers above 10. The discrepancy arose from the uncertainties in the experiments.

Wildin and Truman [16] performed an experimental and a numerical study on cylindrical tanks with radial diffusers and concluded that satisfactory stratification can be achieved at flow rates corresponding to an inlet Froude number of 2. They also mentioned that the mixing at the inlet is also a weak function of the inlet Reynolds number.

Davidson *et al.* [17] and Adams and Davidson [18] investigated experimentally TST with flexible manifolds, rigid manifolds and vertical inlet with no manifolds. They characterized the stratification in terms of a mixing number: defined as the height weighted average energy calculated from the vertical temperature profile. They concluded that the mixing number provides a realistic approach in designing stratified storage tanks and results of flexible manifold showed 48% improvement in stratification compared to conventional vertical inlets.

Hahne and Chen [19] studied the effect of charging temperature, velocity, flow rate and length to diameter ratio and used the charging efficiency to characterize the performance of TST system. The definition of charging efficiency was similar to the one used in the work of Wildin and Truman [16]; it was defined as the ratio of the net storage thermal energy in TST at the end of the charging process and the thermodynamic maximum stored energy. They proposed a relationship for the charging efficiency in terms of the Richardson number, the Peclet number, the Fourier number and the length to diameter ratio. In their study they concluded that the charging efficiency remains constant at temperature differences greater than 20 K and the effect of the velocity can be neglected. With their study on the length to diameter ratio they concluded that a length to diameter ratio of 3 to 4 is recommended. On the effect of the Peclet number they concluded that for Richardson numbers more than 0.25, the effect of the Peclet number on the charging efficiency is negligible. Their conclusion is in agreement with the findings of the experimental study of Sliwinski *et al.* [12] and the analytical study of Yoo and Pak [20]. They also concluded that the effect of the Fourier number on the charging efficiency is smaller compared to the Richardson number and the Peclet number.

Spall [21] investigated the effect of the Reynolds number and the Richardson number on TST with side inlet and concluded that the effect of the Reynolds number on stratification is negligible while only the Richardson number is responsible for inlet mixing. He also concluded that mixing is apparent for Richardson numbers (defined based on the inlet slot height and temperature difference between the initial TST condition and the temperature of the fluid at the inlet) less than 1.0. The conclusion of Spall [21] was in agreement with the conclusion of Mo and Miyatake [22]. Whereas Cai *et al.* [23] suggested that both the Reynolds number and the Richardson number influence the stratification inside the tank. They suggested a Richardson number greater than 5.0 and a Reynolds number less than 1000 for better stratification.

Berkel *et al.* [24] investigated experimentally, numerically and analytically a two layer stratified rectangular storage tank with a side inlet. They concluded that a Richardson number of 10 to15 is an appropriate design condition.

Yee and Lai [25] studied the effect of horizontal inlet with porous manifold and baffle. In their study they concluded that the Richardson number (definition similar to Sliwinski *et al.* [12]) should be more than unity for attaining a stratified tank. The results were in agreement with the study of Guo and Wu [26] and Wildin and Trumen [27]. The stratification was improved as the baffle was moved downwards into the tank. However, moving the baffle beyond half the dimensionless distance showed no improvement in the result.

Anderson and Furbo [28] and Knudsen [29] numerically investigated the effect of large hot draw off on different inlet designs. Anderson and Furbo concluded that with poor inlet design, yearly thermal performance can be degraded up to 23% due to mixing. Knudsen concluded that the performance of TST can be reduced up to 20% when the hot draw off was increased by 40% of the total tank volume. Similar numerical investigation was carried by Shah and Furbo [30] and defined the performance of charging in terms of entropy efficiency and exergy efficiency. They found that both the performance indices increase as a function of the Richardson number and the percentage volume extracted. A relationship was not established and further study was recommended.

Homan [31] studied analytically the charging and discharging process of direct TST systems. The resulting ratio of total entropy generation for ideally stratified tank and fully mixed tank was proposed as a function of the Peclet number and it is shown to vary with $\sqrt{\frac{8}{\pi Pe}}$. Based on this value, he suggested that there can be significant improvement in the efficiency of the thermal energy storage.

In summary, the discussed literature pertains to the effect of the height to diameter ratio, inlet conditions, and the performance of various designs to avoid mixing at the inlet. A summary on the effect of dimensionless numbers on the inlet mixing is shown in table 2.1.

Study	**Dimensionless number**	**Result**
Sliwinski *et al.* [12], Hahne and Chen [19] and Yoo and Pak [20]	Richardson Number	Mixing is negligible above Ri equal 0.25
Zurigat *et al.* [13, 14]	Richardson Number	Mixing is negligible below Ri equal 0.35
Ghajar and Zurigat [15] and Berkel *et al.* [24]	Richardson Number	Mixing is negligible above Ri equal 10
Cai *et al.* [23]	Richardson Number and Reynolds Number	Mixing is negligible above Ri equal 5 and Re less than 1000
Spall [21], Mo and Miyatake [22], Yee and Lai [25], Guo and Wu [26] and Wildin and Trumen [27]	Richardson Number	Mixing is negligible above Ri equal 1

Table 2.1.

Two other factors which are important in understanding the design criterion for SDHW systems are the ambient losses and heat conduction within the wall and water.

Studies (Jularia and Gupta [32], Abdoly and Rapp [33], Shyu *et al.* [34], and Nelson *et al.*[35, 36, 37] have shown that ambient losses are the major source of thermocline degradation in TST and are more detrimental when compared to conduction within the water layers. In an experimental and numerical study on the effect of the wall conductivity on stratification, Miller [38] stated that walls with higher thermal conductivity degrade thermocline faster. Therefore, materials with thermal conductivity less than water should be employed in TST. Sliwinski *et al.* [12] and Sherman *et al.* [39] also made a similar comment on the thermal conductivity of the wall material. On the analytical and experimental study of the TST, Cole and Bellinger [40] stated that the specific heat capacity of the tank should be less than that of water. Abdoly and Rapp [33] in their theoretical and experimental study mention that in TST with length to diameter ratio greater than 10, diameter greater than 1.5 ft (0.46 m)., and insulation resistance of 20 hrft^2 ^{0}F/B.t.u. (3.52 m^2-C/W) ambient losses are minimized. Shyu *et al.* [34] on their study for static conditions (no flow at inlet and outlet) stated that thick tank walls tend to degrade the thermocline fast. They suggested the use of insulation on the inside wall of the tank. Nelson *et al.* [36] and Ghaddar and Al-Maarafie [41] made the same observation on their numerical studies regarding degradation of thermocline with thick walls. Shyu *et al.* [34] and Nelson *et al.* [35] stated that insulation tends to increase the thermal conductance down the wall, however the effect on thermocline degradation is less when compared to tanks with no insulation. Nelson *et al.* [36, 37] on their experimental and numerical studies concluded that length to wall thickness ratio greater than 200 does not affect stratification for static conditions, while for values greater than 300, it does not effect the dynamic condition. Furthermore, they confirmed that for dynamic conditions, mixing at the inlet is the major source of destratification and the effect of the tank wall material is negligible. However, under static conditions the effect of the tank wall conductance cannot be ignored. The results of Nelson *et al.* [36, 37] were in agreement with the results of Lightstone [42] who determined that the effect of wall conductance under dynamic conditions is negligible. Yee and Lai [25] concluded from their numerical study that the Biot number should be less than one to attain stratification. Al-Nimr [43] studied analytically the storage tank and stated that the depth of influence of the inlet temperature increases with wall thickness. However, the effect diminishes for Peclet numbers higher than 10.

2.4 Computational Fluid Dynamics Modeling of TST

Two dimensional CFD analysis has been used to study TST systems for a number of years. Results of some of the studies have been presented in the previous sections. This section highlights the parameters used in those studies.

Hahne and Chen [19] used stream and vorticity functions for laminar flows and studied the effect of the Richardson number and the Reynolds number on the charging efficiency of the inlet. Bouhdjar and Harhad [44] used laminar models to study the tank's aspect ratio and the thermal storage performance of different working fluids. Yee and Lai [25] used a laminar model to study the effect of the porous manifold in storage tanks. Cai *et al.* [23] accounted for turbulence using the Prandtl-Kolmogorov formulation of the turbulent viscosity. Spall [21] in his study commented on the sensitivity of the predicted thermocline thickness to the turbulence model and discretization schemes. He reported thinner thermoclines using the Reynolds Stress Turbulence model than using the standard k-ε model. He also reported thinner thermocline with the Third Order QUICKEST interpolation of the energy equation and the first order interpolation of the remaining equations. However, in the studies mentioned above, no comment on validation was reported.

Ghaddar and Al-Maarafie [41] used a laminar model to predict the flow in a storage tank with inlet diffuser. They reported deviation compared to the experimental results. Ghajar and Zurigat [15] performed laminar modeling with different inlet configurations and predicted that the thermal system was close to perfectly stratified for the conditions studied. They reported good agreement with the experimental results using a Second Order Upwind advection scheme. They also concluded that turbulence modeling had no effect on the result. Shah and Furbo [30] also used a laminar model and a Second Order Upwind advection scheme in the study of inlet configuration and reported poor agreement with experiments. Lightstone *et al.* [45] in their study on the vertical inlet compared the results of a laminar model and a simple eddy viscosity model with experiments and commented on the importance of including turbulence models. Shin *et al.* [46] used the standard k-ε and the RNG k-ε turbulence models on a storage tank with radial diffuser and reported insignificant difference between the results of the turbulence models. The deviation compared to the experimental measurements was reported due to the experimental uncertainties. Oliveski *et al.* [47] reported good results for high inlet Reynolds numbers using the k-ε model. They included the buoyancy term in the production and dissipation equations of the k-ε model and used Power Law interpolation for all the equations.

2.5 System Modeling of TST

Software such as WATSUN, TRANSYS and ESP-r are large system simulation codes and include submodels of TST. Since CFD modeling is computationally expensive, empirical models are developed for modeling heat transfer in TST. These empirical models are often used to solve the one dimensional energy equation for the TST to predict the temperature profile inside it. Several fully stratified models that do not account for fluid mixing, as well as fully mixed models were developed. Some of these models were proposed by Close [48], Duffie and Beckman [49], Sharp [50], Cabelli [51], Yoo and Pak [20, 52], and Al-Nimr [43]. However, the performance of a real TST is between perfectly stratified tanks and fully mixed tanks and several mixing models have also been developed. In this section a literature review on different empirical models which account for the inlet mixing will be discussed.

Cole and Bellinger [40] introduced the inlet mixing parameter which was defined as a function of the Fourier number and the Richardson number. The applicability of the mixing parameter was defined in the range of the Richardson number between 1 and 500.

Wildin and Truman [16] in their finite difference model introduced mixing by averaging the temperature over a few inlet segments as observed in their experiments. However, no indices for length of mixing were proposed.

Oppel *et al.* [53, 54] studied different inlet configurations: inlet with circular baffle, horizontal inlet and a dual radial diffuser, and proposed a turbulent mixing concept in the TST systems. They introduced the thermal eddy conductivity factor as a function of the Richardson and the Reynolds number. They showed that the thermal eddy conductivity varied through out the length of the TST and expressed the eddy conductivity as a decreasing hyperbolic function in the TST with maximum value at the top of the tank. Based on this concept, a number of models were proposed by various authors for different inlet configurations: Zurigat *et al.* [13, 14] proposed models for radial diffuser, side inlet, perforated inlet and impingement inlet. Ghaddar and Al-Maarafie [41] proposed a model based on the same concept; however they defined the eddy diffusivity as a function of the Peclet number. Al-Najem and El-Refaee [55] also applied the same concept using an exponentially decaying function for the eddy diffusivity in the tank for their Chapeau-Galerkin integral formulation. Zurigat *et al.* [14] pointed out that for high flowrates it was not possible to fit an inverse hyperbolic function, hence some manipulations were performed at the lower part of the tank, while maintaining the eddy diffusivity value at the inlet. Furthermore, Zurigat *et al.* [56] compared their model prediction with models proposed by Cole and Bellinger [40], Wildin and Truman [16], Sharp [50] and an analytical non-mixing model of Cabelli [51] for different inlet cases: impingement jet, side inlet and perforated baffle. They found that all the models provided good predictions for nearly perfectly stratified cases i.e. inlets with perforated baffle and impingement jet. However, poor predictions were obtained for side inlets where the buoyancy force was significant.

Nakahara *et al.* [57] proposed a mixing model for a side inlet TST. Based on their experimental and numerical study, they stated that temperature in the inlet mixing zone can be considered to be uniform and the depth of the inlet mixing zone was expressed as a function of the Richardson Number. Atabaki and Bernier [58] used the same concept for electric water heaters to determine the height of the mixing zone. Predictions from both of these studies did not show good agreement with the temperature in the mixing zone. The concept of identifying the mixing zone was also used by Alizadeh [59]. Instead of considering a uniform temperature in the mixing zone, he proposed turbulent and displacement mixing models in the mixing zone. The prediction of the temperature in the mixing zone was better than the predictions of the model proposed by Nakahara *et al.* [57] and Atabaki and Bernier [58]. However, both models proposed by Alizadeh [59] were based on a mixing assumption and not on the physics involved in mixing.

Nelson *et al.* [35, 36, 37] proposed a mixing model as the ratio of the sum of the heat capacities of the tank water in the mixing region and the inlet stream mixing with it to the heat capacity of tank water in the mixing zone as function of Reynolds number and Richardson number. They used experimental results to determine the depth to which the model hold valid, they relied on experimental results.

Oliveski *et al.* [47] in their comparative study of one dimensional model used the models proposed by Klien *et al.* [60] and Franke [61]. These models used computer artifices to correct the one dimensional energy equation with the argument that the highest temperature should be at the top of the tank. Oliveski *et al.* [47] reported that these models can predict results very close to the actual results. However, Oliveski *et al.* [47] along with Caldwell and Bahnfleth [62] and Atabaki and Bernier [58] stated that such models cannot be generalized as they do not take into account for the physics behind the mixing process.

Similar to the analytical non-mixing models of Cabelli [51] and Yoo and Pak [20, 52], Yoo *et al.* [62] proposed an analytical solution for the variable inlet condition, however the solution was not proposed for the extent of the jet affected region. Also, the jet affected region was considered to be a perfectly mixed region in their analysis.

All the mixing models discussed above are developed for the inlet condition where the temperature of the incoming water is hotter than the water temperature in the tank. A situation may arise when the incoming water is colder than the water in the tank. Under this condition, the mixing is detrimental as the buoyancy force acts in the direction of the jet and the jet penetrates deeper inside the tank when compared to the inlet condition where the incoming water is hotter. Models for such inlet condition for the vertical inlet were proposed by Pate [63] and Lightstone *et al.* [64]. They used the mass entrainment formulation in the jet affected region. The extent of this region was defined by the point where the jet temperature was equal to the temperature in the fluid in the tank.

2.6 Summary

Factors which destroy stratification and recommendations to avoid destratification have been revealed. The dimensionless number which plays the important role in characterization of inlet mixing is the Richardson number. The effect of the Reynolds number appears to have different views in the scientific community. The CFD studies of the TST systems reveal that for the systems with a physical control mechanism for limiting inlet mixing, laminar modeling provides a good prediction, however, for the tanks with inlet mixing occurring, turbulence modelling is required. With respect to the one dimensional modelling; incorporating the inlet mixing, it appears; models are designed for predicting highly stratified conditions or a particular inlet geometry which makes the TST system near to perfectly stratified or assumes a uniform temperature distribution in the jet affected region in the upper portion of the tank. The present author did not come across any inlet mixing models which can be directly applied to the vertical inlet TST systems, under conditions, where the inlet temperature is higher than the temperature in rest of the tank.

CHAPTER 3

MATHEMATICAL MODELING AND NUMERICAL METHODOLOGY

3.1 Introduction

This chapter presents the governing equations for incompressible fluid flow and heat transfer. The various turbulence models used in this study are presented. Solution to the governing equations and the boundary conditions are obtained using the commercial software ANSYS CFX – 11. The numerical methods used by the code are also briefly presented in this chapter.

3.2 Mathematical Modeling

The governing equations are given by conservation of momentum, mass and energy. For turbulent flows, the instantaneous velocity ($U_{i,inst}$) is decomposed to the mean velocity ($\overline{U_i}$) and the velocity fluctuation (u_i):

$$U_{i,inst} = \overline{U_i} + u_i \tag{3.1}$$

Substituting Eq. (3.1) and performing a time average results in the Reynolds Averaged Navier-Stokes (RANS) equations. These conservation equations are given below.

Conservation of mass:

$$\frac{\partial \overline{U}_j}{\partial x_j} = 0 \tag{3.2}$$

Conservation of momentum:

$$\frac{\partial \overline{U}_i}{\partial t}+\frac{\partial \overline{U}_j\overline{U}_i}{\partial x_j}=-\frac{1}{\rho}\frac{\partial \overline{p}}{\partial x_i}+\frac{\partial}{\partial x_j}\left[\nu\left(\frac{\partial \overline{U}_i}{\partial x_j}+\frac{\partial \overline{U}_j}{\partial x_i}\right)-\overline{u_i u_j}\right]+S_{M,buoy}+S_M \quad (3.3)$$

Conservation of energy:

$$C_p\frac{\partial(\rho T)}{\partial t}+C_p\frac{\partial\left(\rho\overline{U}_jT\right)}{\partial x_j}=\frac{\partial}{\partial x_j}\left[\Gamma\frac{\partial T}{\partial x_j}-\rho C_p\overline{u_jT'}\right]+S_E \quad (3.4)$$

Where p is pressure, ρ is the fluid's density, ν is the kinematic viscosity ($\nu = \mu/\rho$), C_p is the specific heat capacity and Γ is the molecular thermal conductivity.

If the fluxes in the gravitational direction are important, the pressure term of the momentum equation excludes the hydrostatic pressure gradient and the buoyancy source term is added in the momentum equation.

$$S_{M,buoy}=\left(\rho-\rho_{ref}\right)g \quad (3.5)$$

Where ρ_{ref} is the density at reference location specified in the domain. The density difference in the source term is either calculated based on local density at each node denoted herein as 'full buoyancy model' or is modeled using the Boussinesq approximation.

$$\rho-\rho_{ref}=-\rho_{ref}\beta\left(T-T_{ref}\right) \quad (3.6)$$

The term: $-\rho\overline{u_iu_j}$ is known as the Reynolds stresses tensor, τ_{ij}, whereas the term: $-\rho\overline{u_jT'}$ is called the turbulent heat flux. Mathematical modeling is required to determine the Reynolds stresses and the turbulent heat flux in order to close the RANS equations.

In general, the eddy viscosity (ν_t) representation of the Reynolds stress is:

$$-\overline{u_i u_j} = \nu_t \left(\frac{\partial \overline{U}_i}{\partial x_j} + \frac{\partial \overline{U}_j}{\partial x_i} \right) - \frac{2}{3} k \delta_{ij} \tag{3.7}$$

where k is the turbulent kinetic energy and δ_{ij} is the Kronecker delta. Various mathematical modeling methods have been proposed to model the eddy viscosity and close the RANS equations.

3.3 Two-equation Models

Two-equation models have been the most popular models for a wide range of engineering analysis and research. The most widely used two equation models are the k-ε and k-ω models. In these models, ε is the dissipation or rate of destruction of turbulent kinetic energy per unit time and ω is the inverse of turbulent time scale (time scale of dissipation).

There are some implicit assumptions made in formulating a two-equation model, which are fundamental to some classes of flows. For example, the basis of the two-equation models lies on the assumption that the turbulent fluctuations are locally isotropic or equal. While this can be true for small eddies at high Reynolds numbers, the large eddies are almost always anisotropic, because of the strain rate of the mean flow. Another important assumption is the equilibrium assumption, which states that the production and dissipation terms in the k-equation are approximately equal locally [65].

k-ε Model

A composition of various modeled terms in the transport equations of k and ε yields the standard k-ε model [66]:

$$-\tau_{ij} = \nu_t \left(\frac{\partial \overline{U_i}}{\partial x_j} + \frac{\partial \overline{U_j}}{\partial x_i} \right) - \frac{2}{3} k \delta_{ij} \tag{3.8}$$

$$\nu_t = C_\mu \frac{k^2}{\varepsilon} \tag{3.9}$$

$$\frac{\partial k}{\partial t} + \overline{U_i} \frac{\partial k}{\partial x_i} = -\tau_{ij} \frac{\partial \overline{U_i}}{\partial x_j} - \varepsilon + \frac{\partial}{\partial x_i} \left(\frac{\nu_t}{\sigma_\kappa} \frac{\partial k}{\partial x_i} \right) + \nu \frac{\partial^2 k}{\partial x_i^2} \tag{3.10}$$

$$\frac{\partial \varepsilon}{\partial t} + \overline{U_i} \frac{\partial \varepsilon}{\partial x_i} = -C_{\varepsilon 1} \frac{\varepsilon}{k} \tau_{ij} \frac{\partial \overline{U_i}}{\partial x_j} - C_{\varepsilon 2} \frac{\varepsilon^2}{k} + \frac{\partial}{\partial x_i} \left(\frac{\nu_t}{\sigma_\varepsilon} \frac{\partial \varepsilon}{\partial x_i} \right) + \nu \frac{\partial^2 \varepsilon}{\partial x_i^2} \tag{3.11}$$

The closure coefficients are given by [66]: C_μ=0.09, σ_κ=1.0, σ_ε=1.3, $C_{\varepsilon 1}$=1.44, $C_{\varepsilon 2}$=1.92. These coefficients are obtained by comparisons of the model predictions with experimental results on equilibrium turbulent boundary layers and the decay of isotropic turbulence [66].

***k-ω* Model**

As in the *k-ε* model, *k-ω* model uses the eddy viscosity for the modeling of the Reynolds stresses. But, in contrast to the *k-ε* model, which solves for the dissipation of kinetic energy, *ε*, the *k-ω* model solves for only the rate at which that dissipation occurs, *ω*. Dimensionally, *ω* can be related to *ε*, by: $\omega \propto \varepsilon / k$. The modeled transport equation for *k* and *ω* is given as [67]:

$$\frac{\partial k}{\partial t} + \overline{U_j} \frac{\partial k}{\partial x_j} = \frac{\partial}{\partial x_j} \left[\left(\nu + \frac{\nu_t}{\sigma_\kappa} \right) \frac{\partial k}{\partial x_j} \right] + \tau_{ij} \frac{\partial \overline{U_i}}{\partial x_j} - \beta^* k \omega \tag{3.12}$$

$$\frac{\partial \omega}{\partial t} + \overline{U_j} \frac{\partial \omega}{\partial x_j} = \frac{\partial}{\partial x_j} \left[\left(\nu + \frac{\nu_t}{\sigma_\omega} \right) \frac{\partial \omega}{\partial x_j} \right] + \alpha \frac{\omega}{k} \tau_{ij} \frac{\partial \overline{U_i}}{\partial x_j} - \beta \omega^2 \tag{3.13}$$

The eddy viscosity is given as:

$$\nu_t = \frac{k}{\omega} \tag{3.14}$$

The values of the closure coefficients are: α=5/9, β=3/40, β^*=9/100, σ_ω=1/2, σ_κ=1/2.

Despite their advantages, two equation models also have deficiencies that make their application to complex turbulent flows precarious. The standard *k-ε* model cannot be integrated on a solid boundary; either wall functions or some form of damping must be implemented when applied to a wall bounded flow. However, the *k-ω* model is more computationally robust for the integration to a wall.

SST *k-ω* Model

Some of the above deficiencies of *k-ε* and *k-ω* models were overcome by the SST *k-ω* model. The SST *k-ω* model is a hybrid model in which a *k-ω* formulation is used at the near wall region, and a *k-ε* formulation is used at the outer part of the boundary layer. The difference between the SST model and the standard *k-ω* model is in the different values of the model's constants and in the additional cross term in the *ω*-transport equation. First, the *k-ε* model is transformed into a *k-ω* formulation. The original *k-ω* model is multiplied by a function F_1, the transformed model by the function (1-F_1) and both the models are added. F_1 is called a blending function, because it provides the blending of the two regions. Function F_1 is unity in the near wall region, activating the *k-ω* model and zero at the outer part of the boundary layer, activating the *k-ε* model.

In the SST model, the eddy viscosity, ν_t, is a modified form of the eddy viscosity used in the standard *k-ω* model. It is based on the assumption that the shear stress in a boundary layer is proportional to the turbulent kinetic energy:

$$\nu_t = \frac{a_1 k}{\max\left(a_1 \omega; \Omega F_2\right)} \tag{3.15}$$

where $\alpha_1 = 0.31$, Ω is the absolute value of vorticity and F_2 is a blending function which behaves exactly like the blending function F_1. The function F_2 extends further out into the boundary layer than F_1. The formulations of the blending functions, F_1 and F_2 are given below:

$$F_1 = \tanh(\arg_1^4) \tag{3.16}$$

$$\arg_1 = \max\left(\min\left(\frac{\sqrt{k}}{0.09\omega y}; 0.45\frac{\omega}{y}\right); \frac{400\nu}{y^2\omega}\right) \tag{3.17}$$

$$F_2 = \tanh(\arg_2^2) \tag{3.18}$$

$$\arg_2 = \max\left(2\frac{\sqrt{k}}{0.09\omega y}; \frac{400\nu}{y^2\omega}\right) \tag{3.19}$$

The SST model equations follow:

$$\frac{\partial(\rho k)}{\partial t} + \frac{\partial\left(\rho \overline{u_j} k\right)}{\partial x_j} = P_k - \beta^* \rho \omega k + \frac{\partial\left[\left(\mu + \sigma_k \mu_t\right)\frac{\partial(k)}{\partial x_j}\right]}{\partial x_j} \tag{3.20}$$

$$\frac{\partial(\rho\omega)}{\partial t}+\frac{\partial\left(\rho\overline{u_j\omega}\right)}{\partial x_j}=\gamma P_\omega-\beta\rho\omega^2+2\rho\left(1-F_1\right)\sigma_{\omega 2}\frac{1}{\omega}\frac{\partial(k)}{\partial x_j}\frac{\partial(\omega)}{\partial x_j}+\frac{\partial\left[\left(\mu+\sigma_\omega\mu_t\right)\frac{\partial(\omega)}{\partial x_j}\right]}{\partial x_j}$$

(3.21)

The constants in the above equations are combinations of the original *k-ω* constants and the transformed *k-ε* model constants. Their values and brief description are provided in Table 3.1. If ϕ_1 represents any constant in the original *k-ω* model, ϕ_2 is any constant in the transformed *k-ε* model and ϕ is the corresponding constant in the SST model, their relation is:

$$\phi=F_1\phi_1+\left(1-F_1\right)\phi_2 \tag{3.22}$$

Symbol	Explanation
$\beta^*=0.9$	Destruction term constant
$\beta_1=0.075$	Destruction term constant
$\beta_2=0.0828$	Destruction term constant
$\gamma_1=5/9$	Production term constant
$\gamma_2=0.44$	Production term constant
$\sigma_{k1}=0.5$	Diffusion term constant
$\sigma_{k2}=1.0$	Diffusion term constant
$\sigma_{\omega 1}=0.5$	Diffusion term constant
$\sigma_{\omega 2}=0.856$	Diffusion term constant

Table 3.1.

3.4 Turbulent Heat Flux Model

The turbulent heat flux model uses the concept of a turbulent diffusivity. The turbulent heat flux $-\rho\overline{u_jT'}$ is modeled as:

$$-\rho\overline{u_j T'} = \mu_t^H \frac{\partial T}{\partial x_j} \tag{3.23}$$

Substituting the turbulent heat diffusivity, μ_t^H from the definition of the turbulent Prandtl number: $\Pr_t = \frac{\mu_t}{\mu_t^H}$, Eq. (3.23) is written as:

$$-\rho\overline{u_j T'} = \frac{\mu_t}{\Pr_t}\frac{\partial T}{\partial x_j} \tag{3.24}$$

Turbulent Prandtl number with a value of: $\Pr_t = 0.9$ is used [68].

3.5 Buoyancy Turbulence

For turbulent flows, the effect of buoyancy on fluid turbulence can be included in the turbulence modeling process. Depending upon which of the two models is used, i.e. the full buoyancy model or the Boussinesq model, the buoyancy production term and the dissipation term can be added to the two-equation models. These models essentially model the additional production of the turbulent kinetic energy term due to density gradients. If the full buoyancy model is used (i.e. the density is calculated directly without involving the Boussinesq approximation), the buoyancy production term, P_{kb} is modeled as [68]:

$$P_{kb} = -\frac{\mu_t}{\Pr_t \rho} g \cdot \nabla\rho \tag{3.25}$$

In the case of the Boussinesq buoyancy model (Eq. (3.6)), P_{kb} is modeled as:

$$P_{kb} = \frac{\mu_t}{\Pr_t \rho} \rho\beta g \cdot \nabla T \tag{3.26}$$

This buoyancy production term is included in the turbulent kinetic energy equation and it can also be included in the ε transport equation in the form of:

$$P_{\varepsilon b} = \max(0, P_{kb}) \tag{3.27}$$

In the case of ω based turbulence models, the buoyancy production term is derived from P_{kb} and $P_{\varepsilon b}$, based on the transformation: $\varepsilon = \beta' \omega k$.

3.6 Numerical Methodology

The commercial CFD software used in this study is ANSYS CFX-11.0. The code uses a finite volume discretization, with fully implicit time advancement scheme. In the following sections, there is a brief discussion on the points of the numerical methodology used in this study.

Advection Scheme

Advection refers to the transport of a quantity by the motion of the fluid. The advection scheme is the mathematical formula which is used to discretize the advection term in the governing equations.

There were three advection schemes used in the computations; the first order and the second order upwind schemes and the so called in ANSYS CFX-11.0 high resolution scheme. In a one-dimensional flow, the first order upwind scheme simply assumes that the value of a transported quantity at a node is equal to its upwind node value. Although it is a robust and a reasonable assumption, it tends to smear steep spatial gradients. Based on a Taylor's series expansion, the second order upwind scheme is formed, which is second order accurate in space. The second order upwind scheme tends to introduce discretization errors; dispersive in nature, especially at the rapid change of a solution in space. The three different advection schemes in this study as formulated by ANSYS CFX-11.0 can be represented by Eq. (3.28) [68]:

$$\phi_{ip} = \phi_{up} + \beta \nabla \phi . \vec{r} \tag{3.28}$$

where ϕ_{ip} is the value at the integration point, ϕ_{up} is the value at the upwind node and $\vec{r}$ is the vector from the upwind node to the integration point. Setting β (blending factor) equal to zero, Eq. (3.27) results to the first order upwind scheme. Specifying the value of β between 0 and 1 and $\nabla\phi$ equal to the average of the adjacent nodal gradient reduces the discretization errors [68]. If β is set to 1, Eq. (3.28) results in a second order accurate in space upwind scheme. The so called high resolution advection scheme in ANSYS CFX-11.0 is based on the principle of boundedness prescribed by Barth and Jesperson [69]. In this scheme β varies between 0 and 1 throughout the domain based on the local solution field. In regions of low variable gradients, the blending factor is close to 1.0 for accuracy. In areas where the gradients change sharply, the blending factor is closer to 0.0 to prevent overshoots and undershoots.

Time Advancement

In all the present simulations the time discretization was carried out using the second-order backward Euler scheme. In contrast to the other available option in ANSYS CFX-11.0, namely the first-order backward Euler scheme, the second-order backward Euler scheme does not introduce errors associated to numerical diffusion of the steep temporal gradients. The second-order backward Euler scheme is robust, implicit, and conservative in time and it does not create any time step limitation. Although it is second order accurate in time, it is not bounded and nonphysical solution oscillations are possible [68]. Since ANSYS CFX-11.0 is an implicit code, there is no requirement for a sufficiently low Courant number for stability.

3.7 Boundary Conditions

In the next sections, the boundary conditions used in the current computations are briefly discussed.

Wall Boundaries

At the walls of the computational domain, the no slip and the adiabatic boundary conditions were applied; they imply that the fluid velocity and the heat transfer, respectively, at the walls are set to zero:

$$\begin{aligned} U_{wall} &= 0 \\ q_{wall} &= 0 \end{aligned} \tag{3.29}$$

Inlet Boundaries

The inlet boundary condition for the continuity and momentum equations is given by the mass flow rate which is specified along with a direction component. The mass influx is calculated by:

$$\rho U = \frac{\dot{m}}{\int_S dA} \tag{3.30}$$

Where $\int_S dA$ is the integrated boundary surface area at a given mesh resolution.

Turbulence at the inlet was specified using turbulence intensity, I. The values of k and ε at the inlet were calculated as follows [68]:

$$k_{inlet} = \frac{3}{2} I^2 U^2 \tag{3.31}$$

$$\varepsilon_{inlet} = \rho C_{\mu} \frac{k^2}{\mu_t} \tag{3.32}$$

where,

$$I = 0.01 \text{ and } \mu_t = 1000 I \mu \tag{3.33}$$

The inlet boundaries are completed with the inlet temperature specification for the energy equation.

Outlet Boundaries

The only outlet boundary refers to the average static pressure. The outlet relative static pressure is constrained such that the average is the specified value [68]:

$$\overline{p}_{spec} = \frac{1}{A} \int_S p_n dA \tag{3.34}$$

The integral is over the entire outlet boundary surface. This condition is enforced by setting the pressure at each boundary integration point (ip) as:

$$p_{ip} = \overline{p}_{spec} + \left(p_{node} - \overline{p}_{node} \right) \tag{3.35}$$

In this way, the exit boundary condition pressure profile can float, but the average value is constrained to the specified value.

Symmetry Boundaries

A physical problem is symmetric about a plane when the flow on one side of the plane is a mirror image of the flow on the opposite side. When a symmetry boundary is applied at a plane, the fluxes normal to that plane are zero. In addition, for the velocity parallel to the symmetry line, zero gradient boundary condition is applied. Finally, the normal gradients of the Reynolds stresses are set to zero.

3.8 Summary

In this chapter, the governing equations together with the mathematical modeling approach and a brief discussion of the numerical methodology were presented. The turbulence models used were presented, i.e. the k-ε model, the k-ω model and the SST k-ω model, together with the turbulent heat flux model and the effect of the buoyancy term in the modeling procedure. Finally the numerical treatment of the spatial and the temporal terms was discussed, together with the applied boundary conditions.

CHAPTER 4

CFD Study of Solar Domestic Hot Water Tank System

4.1 Overview

This chapter presents the simulation results and analysis of the temperature and velocity fields in the vertical inlet SDHW systems. Two different cases of the vertical inlet TST systems are presented. One of the systems has fixed inlet temperature and flow rate through out the charging process. Henceforth, it will be referred as Case I. The experimental results of Leohrke and Holzer [70] were used for the validation study of Case I. The other system is with a NCHE; hence, the inlet conditions change throughout the charging process and will be referred as Case II. Grid independence was confirmed for simulation of both the systems. Sensitivities to turbulence models were studied for both the cases. Sensitivities to the advection scheme were performed for Case I. The advection scheme whose predictions were closer to the experimental results of Case I was used for Case II. The numerical results of Case II were compared to the experimental results of Cruickshank and Harrison [5].

4.2 Case I – Constant Inlet Condition

4.2.1 Details of Experimental Setup

The experiments of Leohrke and Holzer [70] consisted of charging experiments at room temperature. The experiments were conducted to assess the effect of inlet configuration on stratification inside the TST. Two different types of inlet configuration were studied:

vertical inlet with and without a cup diffuser. The inlet configuration whose experimental results were used for validation in this work was the vertical inlet without the cup diffuser. Figure 4.1 shows schematic of the experimental TST for Case I. The inlet temperature and velocity were constant throughout the charging process. Note that the inlet pipe was submerged in the TST by 50.8 mm. The TST was made of steel and was

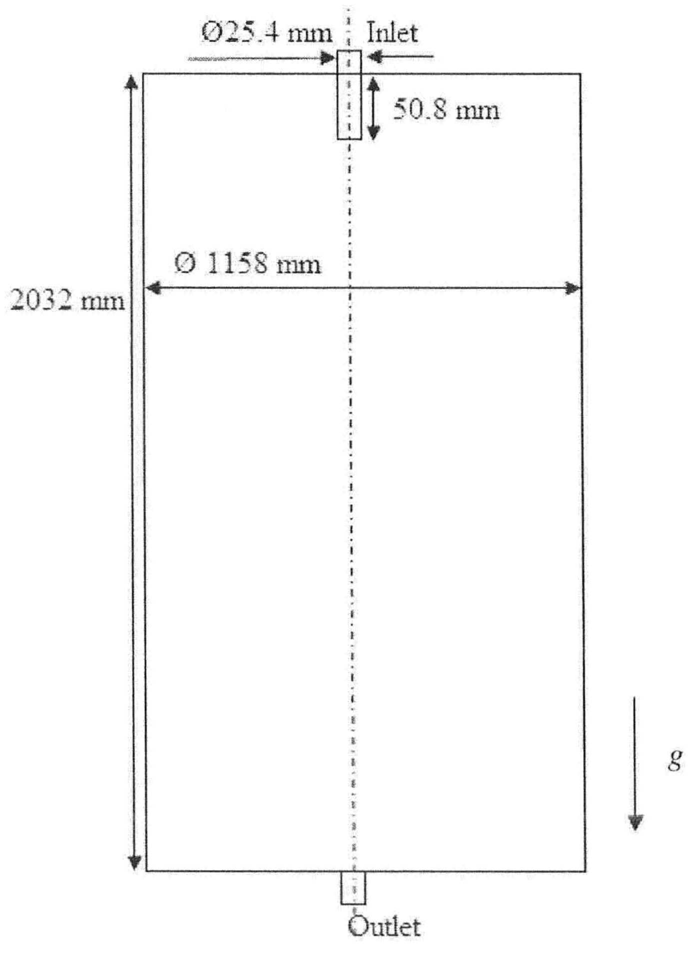

Figure 4.1: Schematic of Experimental TST Case I.

insulated on all the sides. There were ten thermocouples located at a distance of 420 mm way from the tank centerline. The thermocouples were 100 mm apart. The top most thermocouple was 32 mm below the tank top. The experimental uncertainty with the thermocouple was reported as $\pm$ 0.5^{0}C. The inlet velocity and temperature in the experiment with vertical inlet without the diffuser were 0.18 m/s and 40.0^{0}C, respectively. The initial temperature of the water in the TST was approximately 21.0^{0}C.

4.2.2 Simulation Details

Solution Domain and Mesh

The domain was based on the experimental setup as described above. Due to symmetry the flow was treated as two dimensional and the domain extended radially from the TST centerline to the wall. The temperature and velocity distributions inside the TST are mainly governed by the inlet jet mixing. Hence, in order to capture the details of the flow at the jet penetration region and keep the simulations computationally viable, a non uniform mesh was used that employed a fine mesh near the inlet region and a coarser mesh in rest of the TST. Figure 4.2 shows the grid distribution inside the domain.

In order to assess grid independence, four different grids were studied. The details of grid distribution are given in Table 4.1. Mesh 2 was used for further analysis of the system while Mesh 1, Mesh 3 and Mesh 4 were only used for the grid independence analysis. In Mesh 3, the minimum and maximum distance between two grids in the radial direction were 3.3 mm and 20.1 mm, respectively. Similarly, the maximum and minimum distances in the axial direction were 12.4 mm and 1.0 mm, respectively. The grid expansion ratio of 1.2 was used in the radial direction. The grid expansion ratio of 1.0001 was used in the axial direction.

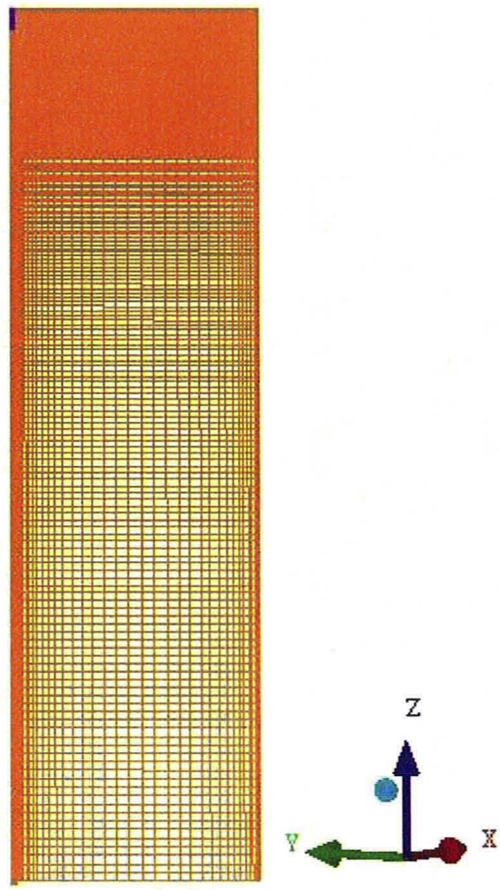

Figure 4.2: Case I Mesh.

Coordinate Directions	Mesh 1	Mesh 2	Mesh 3	Mesh 4
X (radial)	44	44	44	89
Z (axial)	166	317	401	317

Table 4.1.

Fluid Properties

Constant properties of water at 25^0C were used as given in Table 4.2.

Property	Mesh 1
Fluid	Water
Density	997.0 kg m^{-3}
Dynamic Viscosity	8.899×10^{-4} kg $m^{-1}s^{-1}$
Thermal Expansivity	0.000257 K^{-1}
Specific Heat Capacity	4178 J/kg K

Table 4.2.

Boundary and Initial Conditions

A symmetric boundary condition was used in the circumferential direction. No slip boundary condition was applied on all other surfaces of the domain. A velocity of 0.18 m/s, as observed in the experiments [70] was applied at the inlet of the pipe to drive the flow. The inlet Reynolds number was approximately 8000 based on the bulk velocity and hydraulic diameter of the inlet pipe.

The temperature of the charging fluid at the inlet was 40.0^{0}C and the temperature of the fluid in the domain was 21^{0}C as observed in the experiments [70]. The TST was insulated in the experiment and hence an adiabatic wall condition was applied on the TST's walls. The numerical scheme is fully implicit and does not require a small Courant number for stability. The time step was set to 0.2 seconds. The time step chosen was one fourth of the value on which previous simulations were performed on the same domain by Lightstone *et al* [45].

Advection Schemes and Mathematical Models

Sensitivity to the numerical advection schemes used for all the equations (continuity, momentum, energy and eddy viscosity) was tested by performing simulations using the first order upwind, the second order accurate and the high resolution schemes. The Boussinesq model was used to account for the buoyancy effect in the domain. Turbulence caused by the inlet jet was modeled using the SST model, the k-ω model and the k-ε model with the buoyancy term in the production and dissipation terms of the models. SST model without the buoyancy term was also considered. The details of the advection schemes and the turbulence models used are given in Table 4.3.

4.2.3 Results and Discussion for Case I

A series of simulation to assess the effects of grid sensitivity, turbulence model and advection scheme were performed. A summary of the test cases is provided in Table 4.3.

Mesh Sensitivity Analysis

The temperature predictions inside the TST using different meshes were compared. The results are shown in figure 4.3 and 4.4. All the four simulation; *1M1, 1M2, 1M3* and *1M4,* used the same advection scheme (high resolution) and turbulence model (SST with buoyancy). Results are shown at a distance of 42 cm away from the TST centerline. The results after 5 minute show that all the three meshes with axial refinement (*M1, M2* and *M3*) predict similar temperature profiles inside the TST. However, at later time; at 60 minute, the temperature prediction of Mesh 1 deviated from the predictions of the other two axially refined meshes (*M2* and *M3*). The maximum deviation of 0.8^0C was observed. The deviation in the results between Mesh 2 and Mesh 3 was less than 0.15^0C. The results from the radially refined mesh (Mesh 4) were consistent with the results of

Simulation	Mesh	Advection scheme	Turbulence Model
		Grid Sensitivity	
1M1	Mesh 1	High resolution	SST (buoyant)
1M2	Mesh 2	High resolution	SST (buoyant)
1M3	Mesh 3	High resolution	SST (buoyant)
1M4	Mesh 4	High resolution	SST (buoyant)
		Turbulence Model and Advection Scheme Analysis	
1S1	Mesh 2	1^{st} (o) upwind	SST (buoyant)
1S2	Mesh 2	2^{nd} (o) accurate	SST (buoyant)
1S3	Mesh 2	High resolution	SST (buoyant)
1S4	Mesh 2	High resolution	SST (non-buoyant)
1S5	Mesh 2	High resolution	k-ε (buoyant)
1S6	Mesh 2	High resolution	k-ω (buoyant)

Table 4.3.

Mesh 2 and Mesh 3 for the entire simulation time of 60 minutes. The maximum deviation of less than 0.2^0C was observed. Though the axially refined meshes, Mesh 2 and Mesh 3 showed consistent results for sixty minutes of simulation time, the results may not be grid independent after 60 minutes of simulation since the thermocline may penetrate into the region of the tank where the grid has been coarsened. This will result in numerical diffusion in that region. Therefore, all further studies were performed within the simulation time of 60 minutes on Mesh 2.

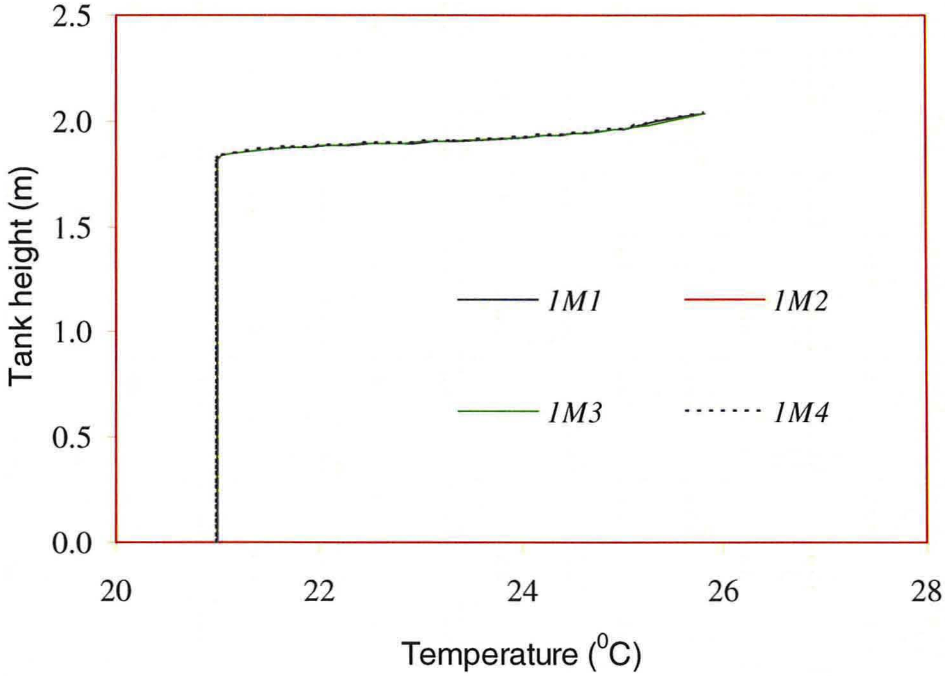

Figure 4.3: Temperature Predictions Inside the TST Case I at 5 Minute.

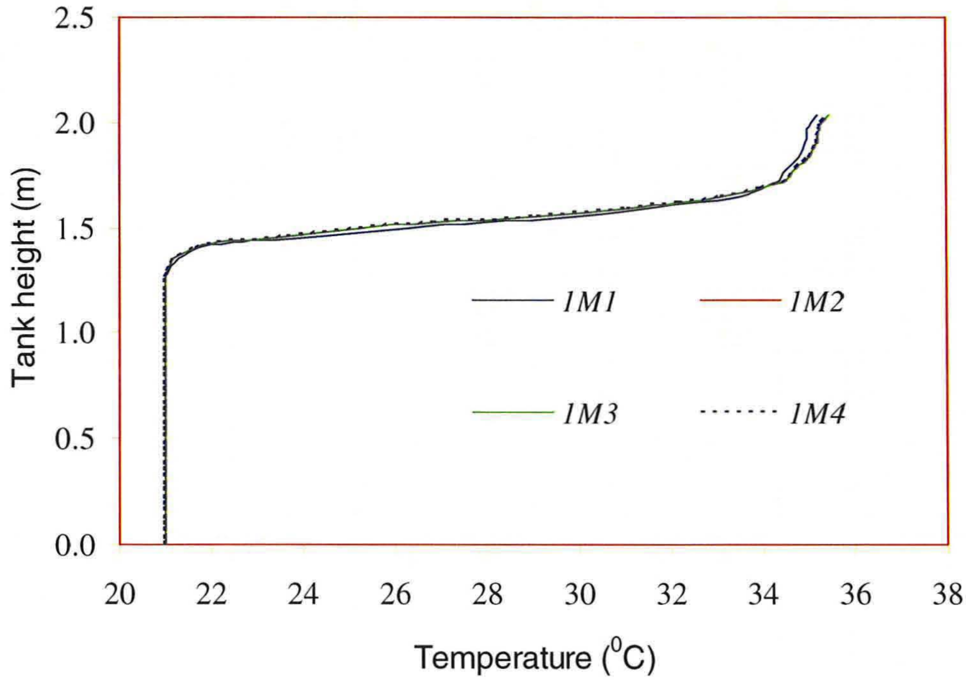

Figure 4.4: Temperature Predictions Inside the TST Case I at 60 Minute.

Turbulence Models and Advection Scheme Validation with the Experiment

Figures 4.5 to 4.12 compare the predicted temperature distribution inside the tank with the experimental results at different time intervals. Temperatures were predicted at a distance of 42 cm away from the TST centerline, which coincided with the radial location of the thermocouples. Comparing the results of the simulations *1S1*, *1S2* and *1S3*, which had different advection schemes but had the same turbulence models, it is evident that the prediction of the thermocline by *1S2* and *1S3* are similar and show deviations of less than 0.4^0C with each other. Predictions from both the schemes were very close to the experimental results, i.e. deviations were less than 1.5^0C. Simulation *1S1* gave a poor prediction of the thermocline. Although the numerical results at the upper part of the thermocline were initially close to the experiment, with time, the entire thermocline became steeper and the temperature at the upper part of the themocline was under-predicted. The prediction at the base of the thermocline was smeared throughout the simulation time. Initially, smearing is low but gradually increases with time, which is consistent with the false diffusion associated with the first order upwind solution.

The results of the simulations *1S3*, *1S5* and *1S6* in comparison to the results of simulation *1S4* clearly show the importance of including the buoyancy term in the production and dissipation terms of the turbulence models. The advection scheme used for all the four simulations was the high resolution. The predictions of simulations: *1S3*, *1S5* and *1S6* almost overlap and are in good agreement with the experimental results. The

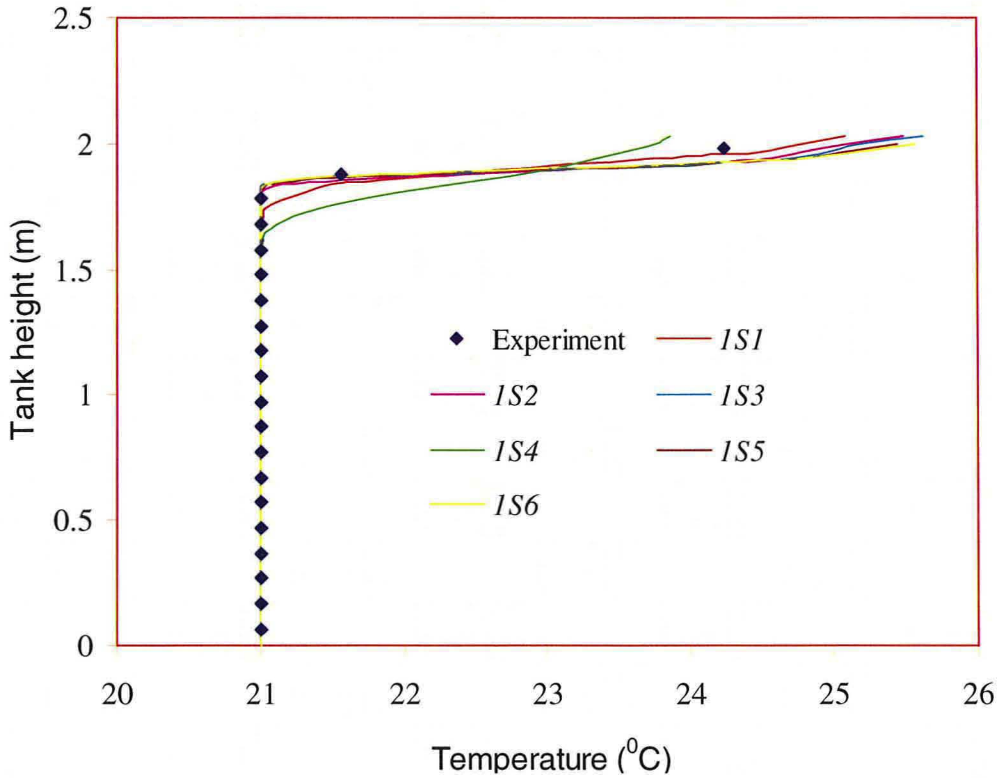

Figure 4.5 Temperature Predictions Inside the TST Case I at 5 Minute.

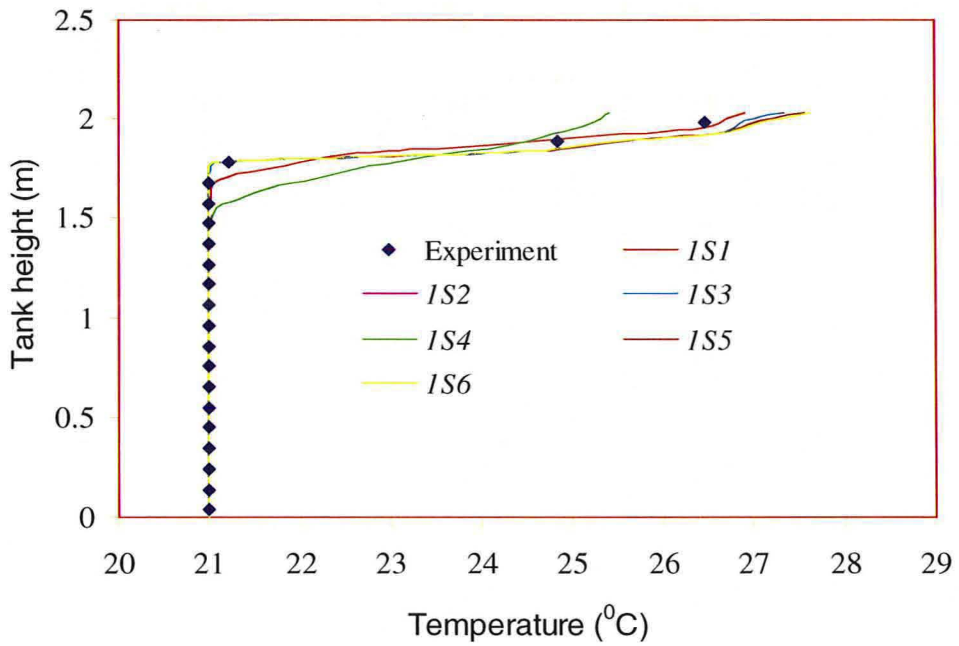

Figure 4.6: Temperature Predictions Inside the TST Case I at 10 Minute.

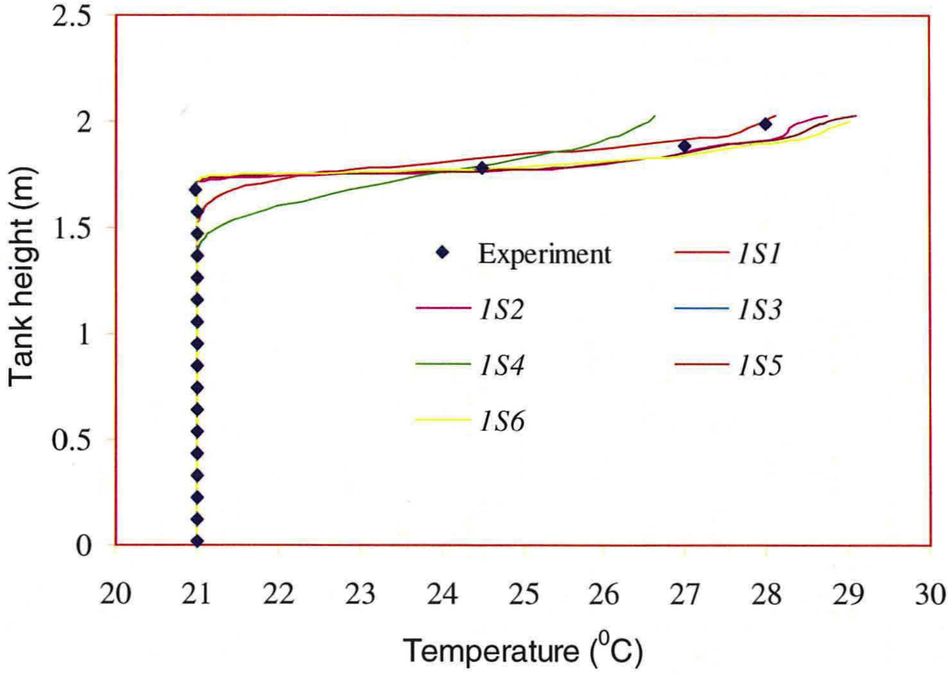

Figure 4.7: Temperature Predictions Inside the TST Case I at 15 Minute.

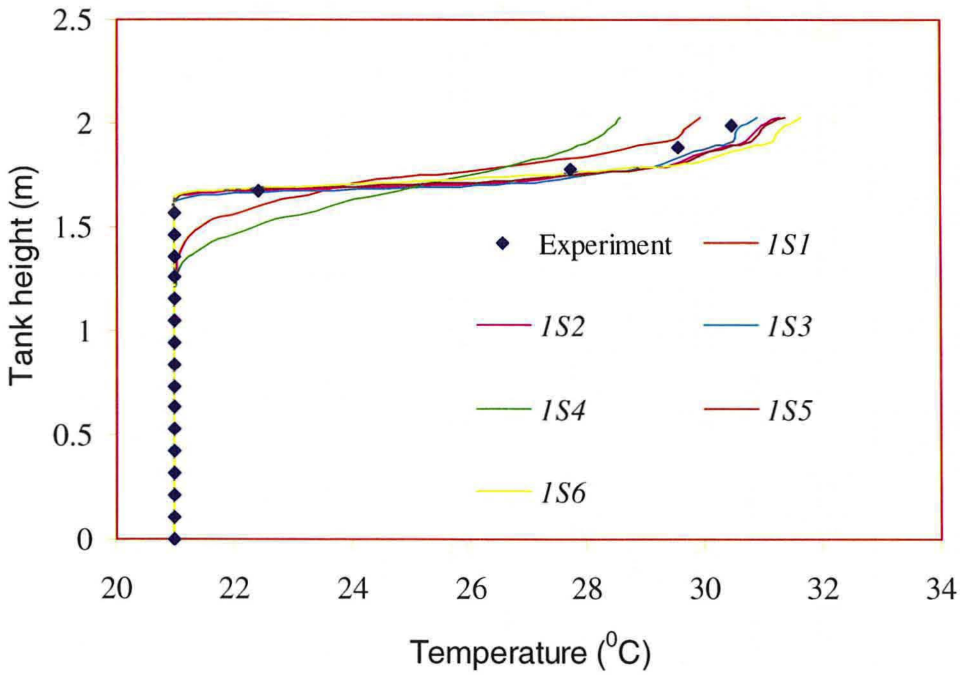

Figure 4.8: Temperature Predictions Inside the TST Case I at 25 Minute.

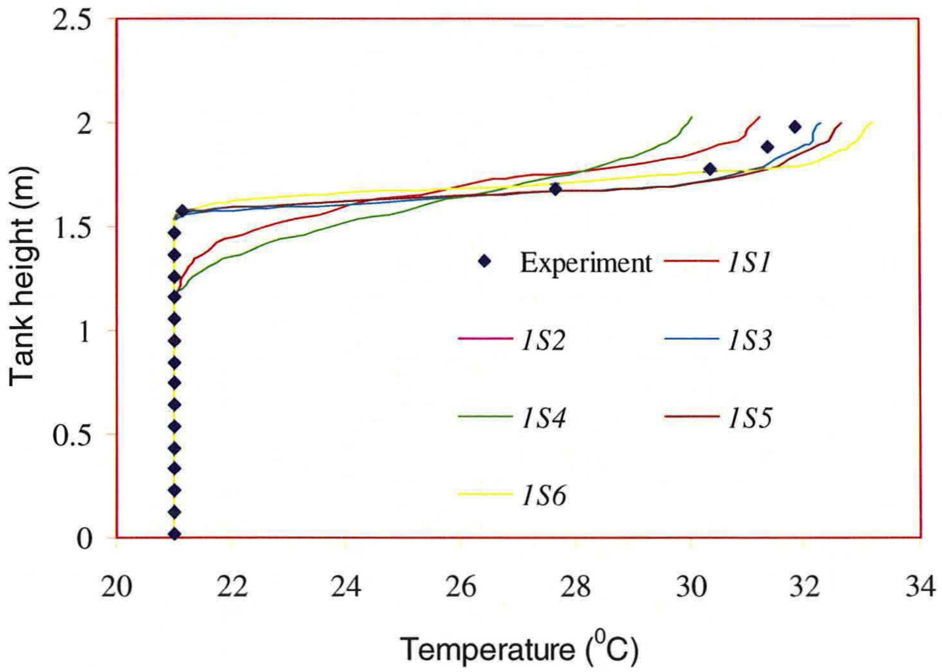

Figure 4.9: Temperature Predictions Inside the TST Case I at 35 Minute.

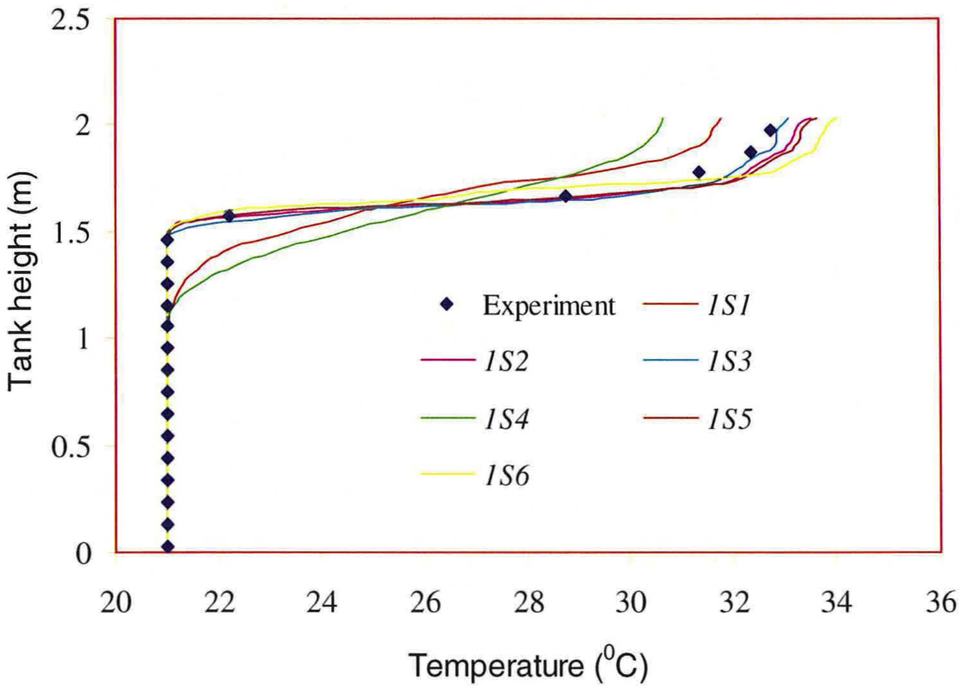

Figure 4.10: Temperature Predictions Inside the TST Case I at 40 Minute.

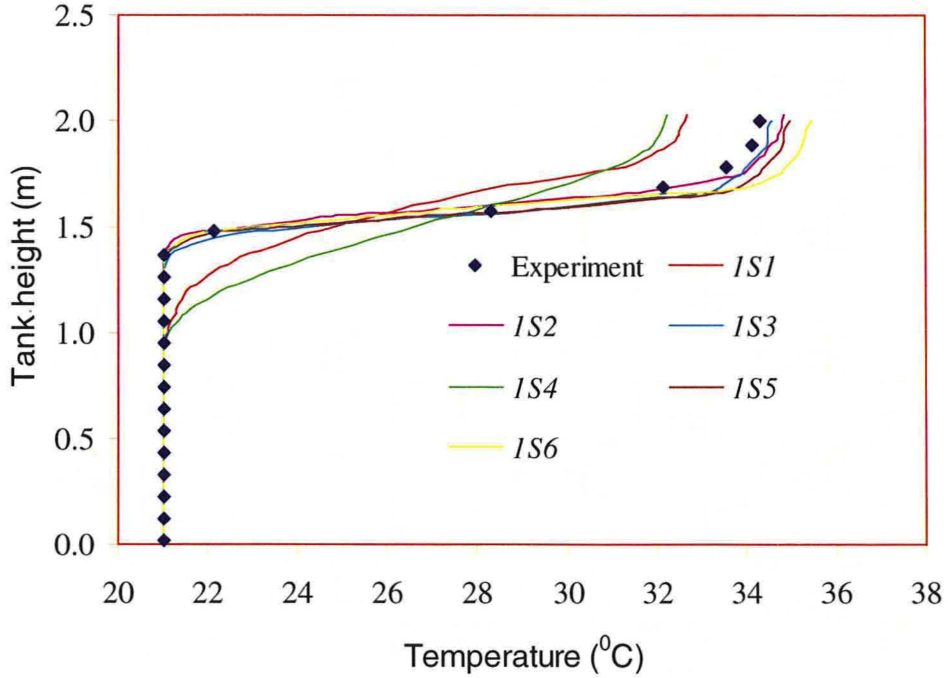

Figure 4.11: Temperature Predictions Inside the TST Case I at 55 Minute.

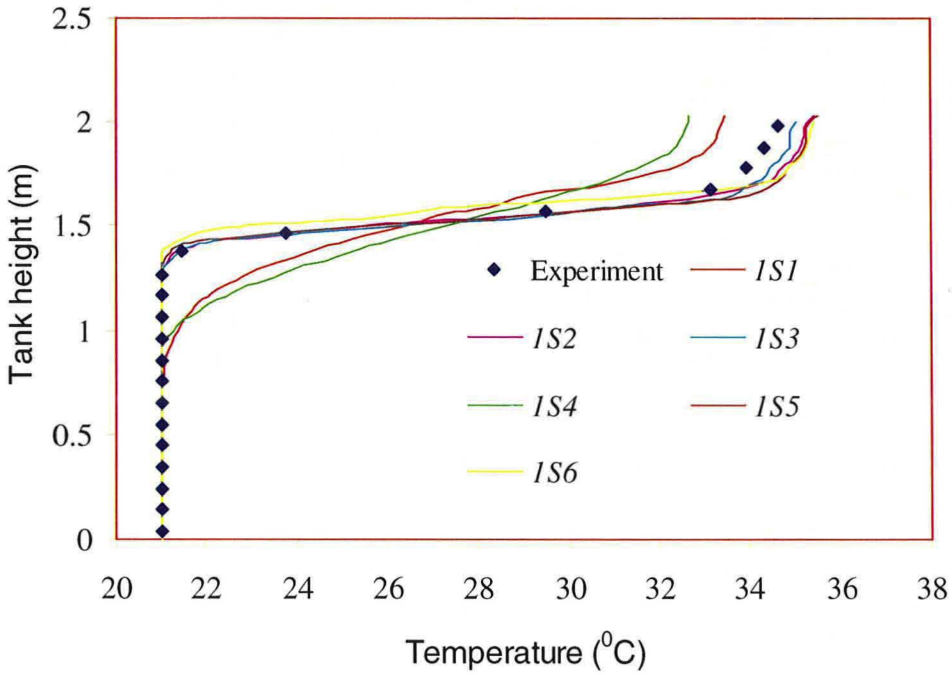

Figure 4.12: Temperature Predictions Inside the TST Case I at 60 Minute.

maximum deviation of 1.5^{0}C was observed in the results of the simulation *1S6* (*k-ω* (buoyant)). The prediction of *1S4* (SST (non-buoyant)) is poor. It predicted a deeper thermocline or more mixing in the upper part of the TST as compared to the experimental results. The results of simulations *1S3, 1S5* and *1S6* show that the presence of the buoyant force opposed the turbulence caused by the inlet jet and therefore there was less mixing in the jet affected region of the TST.

From the results it can be concluded that the higher order advection schemes and eddy viscosity based two equation turbulence models with turbulence buoyancy term included in the turbulence equations give good prediction of the temperature distribution inside the TST for the high inlet Reynolds number case.

4.3 Case II – Variable Inlet Condition

The second case considered in this study was a SDHW system with an NCHE. Inlet temperature and flow rate for such systems vary with time. Figure 4.13 shows a typical SDHW system with NCHE. The fundamentals of flow development for a SDHW system with an NCHE have been previously discussed in Chapter 1. Figure 4.14 shows the flow rate and the temperature at the inlet of the TST for a SDHW system with NCHE (for the case where there are no draw offs). The net hydrostatic pressure in the TST reduces with time as hot water is delivered to the TST. As a result, the flow rate reduces and the temperature increases across the heat exchanger in the TST loop. In addition to the advantages of the SDHW with NCHE presented in Chapter 1, such systems also ensure low inlet flow rates and the inlet temperature is typically higher than the temperature of the fluid in the vicinity of the jet penetration region in the storage tank. Hence, such systems are able to minimize the mixing caused by the positive buoyant plume (momentum of the jet and buoyancy force acts in the same direction) and negative buoyant plumes (momentum of the jet and the buoyancy acts in opposite direction).

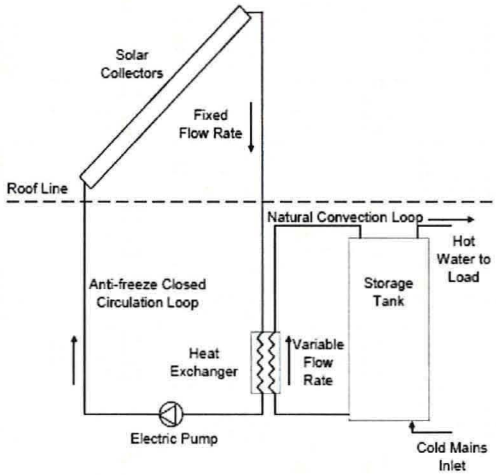

Figure 4.13: A typical SDHW System with NCHE [1].

4.3.1 Experimental Setup

Experiments were conducted by Cruickshank and Harrison [5] for the determination of the performance parameters of the natural convection compact plate heat exchanger used

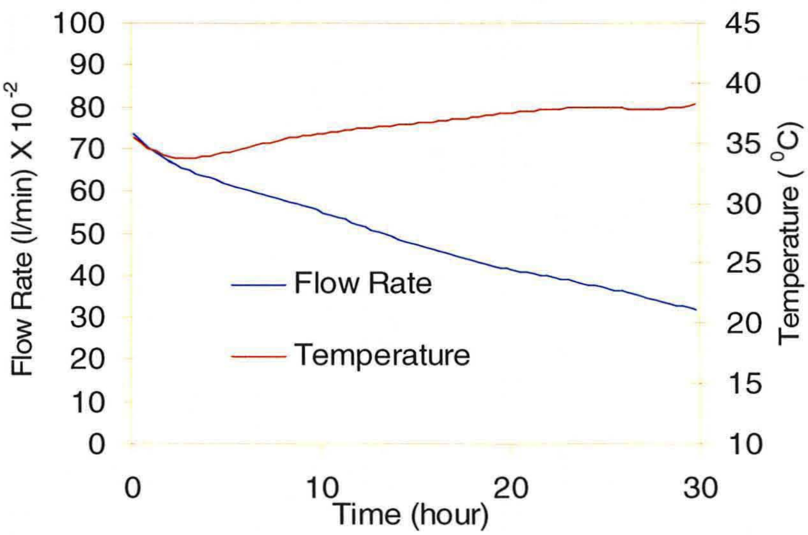

Figure 4.14: Inlet Boundary Condition Case II.

in their experiments. Experiments were performed with constant flow rate in the collector loop. Temperatures at the inlets and the outlets of the heat exchanger were measured with the aid of thermocouples. The flow rate in the TST loop was calculated using the energy balance across the heat exchanger. The average density of the fluid in the heat exchanger on the TST side was based on the average of the inlet and outlet temperature of the heat exchanger. The density of the fluid in the pipe on the TST side is based on the temperature of the fluid at the outlet of the heat exchanger on the TST side. The average density in the TST was calculated based on the average temperature recorded by thermocouples in the TST. Figure 4.15 shows a schematic of the experimental TST for Case II. The TST was made of steel with a glass lining and was insulated from all the sides. There were eight thermocouples spaced vertically 150 mm apart, as shown in Figure 4.15. The top most thermocouple was located at 300 mm below the top cover. The working fluid in the collector loop (not shown in the figure) was a glycol-water mixture. The flow rate and the temperature in the collector loop were constant. Experiments consisted of eleven charging tests at different collector side flow rates and temperatures. The particular test for which simulation results were validated had a flow rate of 0.90 liter/minute and the temperature of water-glycol mixture was 40.0^{0}C in the collector loop. The initial temperature of the water in the TST was approximately 5.0^{0}C. The Reynolds number, based on the inlet pipe hydraulic diameter and bulk flow, was approximately 1100 at the beginning of the flow. A compact brazed plate heat exchanger (not shown in the figure) with 20 plates was used. The heat transfer area was approximately 0.396 m^2. The heat exchanger was made of steel and was fully insulated. The height of the heat exchanger was 310 mm. The experimental performance parameters of the compact plate heat exchanger were developed by Cruickshank and Harrison [5] for their particular system and are given in Eqs. (4.1) and (4.3), where $\dot{m}_s$ is volume flow rate in L/min, ΔP is the net hydrostatic pressure (in N/m^2) in the storage loop. ρ_t, ρ_x and ρ_p (in kg/m^3) are the average densities in the storage tank, heat exchanger and the pipe, respectively. The variables h_t, h_x and h_p (in m) are the height of the storage tank, heat exchanger and pipe, respectively. The variable ε_{mod} is the modified heat exchanger effectiveness. The variable C_{mod} is the modified capacitance ratio of the heat exchanger.

$$\dot{m}_s = 0.0398\Delta P^{0.6505} \tag{4.1}$$

where,

$$\Delta P = (\rho_t h_t - \rho_x h_x - \rho_p h_p)g \tag{4.2}$$

$$\varepsilon_{mod} = -0.3488C_m^2 + 1.1402C_m \tag{4.3}$$

These performance parameters were determined as the functions of hydrostatic pressure difference in the TST loop and the flow condition in the collector loop. Such performance parameters eliminate the need for including the heat exchangers and the associate piping in the computational domain of the TST.

The current author had discussions with the experimentalist regarding the uncertainties in the experiments. It was revealed that due to the difficulty of positioning the thermocouple in the tank, the locations of thermocouple were approximate. Further, as mentioned above, the flow in the TST loop was based on the energy balance across the exchanger and it was not confirmed with physical measurement.

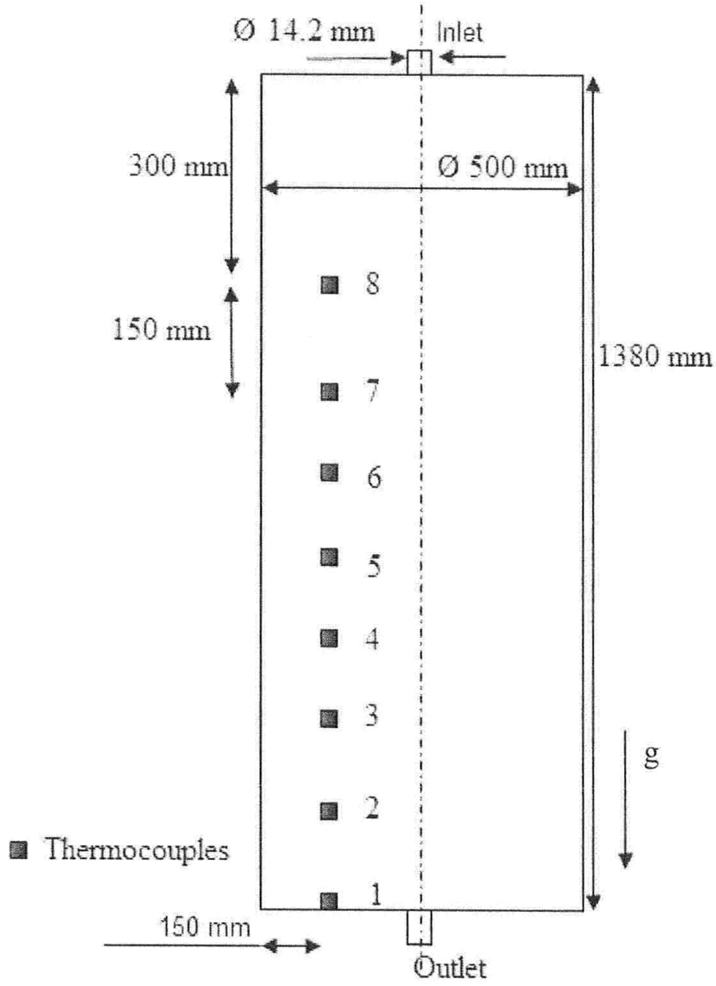

Figure 4.15: Schematic of the Experimental TST Case II.

4.3.2 Simulation Details

Solution Domain and Mesh

The solution domain for Case II was similar to Case I, however the dimensions of the domain were set to the values for the experimental setup of Cruickshank and Harrison [5]. Figure 4.16 shows the grid distribution inside the domain. A non-uniform meshing law was used to mesh the domain. The mesh was fine adjacent to the inlet, both in the x and y directions. In order to obtain grid independent results, four different mesh systems were studied. The details of the grid distribution in the respective direction are given in Table 4.4. Mesh 1 and Mesh 2 were used for further analysis of the system while Mesh 3 and Mesh 4 were only used for the grid independence analysis. The minimum and maximum distance between the grid points in radial direction was 2 mm and 21.04 mm, respectively, for Mesh 1. Similarly, the maximum and minimum distance in the axial direction was 21.0 mm and 3.0 mm, respectively. The maximum and minimum distance in axial direction between the grid points was 1.5 mm and 12 mm, respectively, for Mesh 2. The grid expansion ratio of 1.1 was used in the radial direction. The grid expansion ratio of 1.01 was used in the axial direction.

Coordinate Directions	Mesh 1	Mesh 2	Mesh 3	Mesh 4
X (radial)	26	26	26	53
Y (axial)	105	213	273	213

Table 4.4.

Fluid Properties

The initial temperature of the fluid in the TST was approximately 5^0C. The temperature of the fluid in the collector loop was approximately 40^0C. The expected temperature change in the domain was large; therefore rather than employing the Boussinesq approximation, the density was calculated directly as a function of temperature. The relationship between the two quantities was adapted from the work of Purdy *et al.* [3]. The relationship is shown in Eq. (4.4) where density (ρ) is in kg/m^3 and temperature (T) in Celsius. A constant dynamic viscosity equal to $8.899\text{x}10^{-4}$ kgm^{-1}sec^{-1} was used for all the simulations.

$$\rho = -0.0670346(T)^2 \quad 0.035868(T) + 1000.31 \tag{4.4}$$

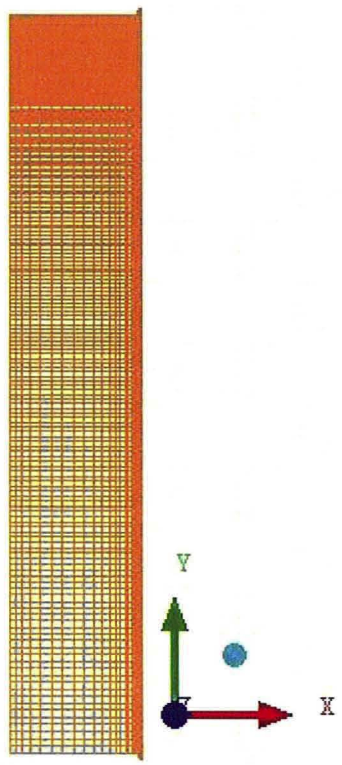

Figure 4.16: Mesh Case II.

Boundary and Initial Conditions

Symmetric boundary conditions were used in the circumferential direction. No slip boundary conditions were applied on all the other surfaces of the domain. Two different inlet boundary conditions for the transient values of the inlet mass flow and temperature were considered. The first inlet boundary condition is termed as *B1* and the second boundary condition is termed as *B2*. For *B1*, the experimental temperature recorded at the outlet of the heat exchanger and the experimental mass flow rate calculated in the TST loop was used. The inlet flow rate and the temperature for *B1* are shown in figure 4.14. For *B2*, the flow rate and the temperature were derived from Eqs. (4.1) and (4.3) and the heat exchanger effectiveness definition provided in Eq. (4.8). The mass flow rate and temperature at the inlet are given by Eqs. (4.7) and (4.12), respectively.

Rewriting Eq. (4.1):

$$Q_s = (0.0398 \cdot \Delta P^{0.6505})/(60*1000) \tag{4.5}$$

also,

$$\dot{m}_s = Q_s.\rho \tag{4.6}$$

Substituting Eq. (4.5) into Eq. (4.6), it becomes

$$\dot{m}_s = (0.0398 * \Delta P^{0.6505}) * \rho/(60*1000) \tag{4.7}$$

Heat exchanger effectiveness is defined as [5]:

$$\varepsilon = q_{actual} / q_{\max} \tag{4.8}$$

where

$$q_{\max} = \dot{m}_c * Cp_c * (T_{c_{in}} - T_{s_{in}}) \tag{4.9}$$

and

$$q_{actual} = \dot{m}_s * Cp_s * (T_{s_{out}} - T_{s_{in}}) \tag{4.10}$$

Substituting Eqs. (4.9) and (4.10) in Eq. (4.8) and rearranging:

$$T_{s_{out}} = \left(\varepsilon * \left(\frac{\dot{m}_c * Cp_c}{\dot{m}_s * Cp_s} \right) * (T_{c_{in}} - T_{s_{in}}) \right) + T_{s_{in}} \tag{4.11}$$

Substituting the value of ε from Eq. (4.3) into Eq. (4.11) and also $T_{s_{out}} = T_{tnk_{in}}$ yields:

$$T_{tnk_{in}} = T_{s_{out}} = \left(\left(-0.3488 * \left(\frac{\dot{m}_s * Cp_s}{\dot{m}_c * Cp_c} \right) + 1.1402 \right) * (T_{c_{in}} - T_{s_{in}}) \right) + T_{s_{in}} \qquad (4.12)$$

The flow rate in the collector loop was constant at 0.9 liter/min, and the temperature of the working fluid in the collector loop was constant at 40^0C. The initial temperature of the fluid in the domain was 5^0C, as observed in the experiments. The TST was insulated in the experiment and hence an adiabatic wall condition was applied on the TST walls. The time step was kept 0.2 s similar to the high inlet Reynolds number case (Case I).

Advection Schemes and Mathematical Models

The results of Case I (fixed inlet condition) showed that the second order accurate and high resolution advection schemes predicted accurate and similar results. Hence, the high resolution scheme was used for all the equations (continuity, momentum, and energy and eddy viscosity).

The study of turbulence models for Case I showed that the models, namely SST, k-ε and k-ω with the buoyancy term included in the production and dissipation term gave good results with the best predictions obtained using the SST and k-ε models. In consideration to this fact, SST and k-ε with buoyancy term were considered for Case II. Apart from these two turbulence model SST without buoyancy term was also considered. Since, the inlet Reynolds number was in the laminar range, laminar modeling of the domain was also considered. Justification for considering the SST without buoyancy term and the laminar model will be discussed in the model analysis section. The temperature difference was large (5^0C to 40^0C); hence the full buoyancy model was used to account for the buoyancy effect in the domain.

4.3.3 Results and Discussion for Case II

Similar to Case I, a series of simulations were performed to assess the effect of the turbulence models, the inlet boundary conditions and the grid sensitivity. A summary of the test cases is provided in Table 4.5.

Simulation	Mesh	Inlet Boundary	Turbulence Model
		Grid Sensitivity	
2M1	Mesh 1	*B2*	SST (non-buoyant)
2M2	Mesh 2	*B2*	SST (non-buoyant)
2M3	Mesh 3	*B2*	SST (non-buoyant)
2M4	Mesh 4	*B2*	SST (non-buoyant)
		Turbulence Model	
2S1	Mesh 1	*B1*	Laminar
2S2	Mesh 2	*B1*	SST (buoyant)
2S3	Mesh 1	*B1*	k-ε (buoyant)
2S4	Mesh 2	*B1*	SST (non-buoyant)
2S5	Mesh 2	*B2*	SST (buoyant)
2S6	Mesh 2	*B2*	SST (non-buoyant)

Table 4.5.

Note that in accordance with the way in which the experimentalist presented their results, temperature as function of time for a number different monitored location will be provided. This is in contrast to how the results for Case I were given in which 'snapshot' of the axial temperature distribution at specified times were presented.

Mesh Sensitivity Analysis.

The temperature at the locations, where the thermocouples were placed in the experiments, was monitored as a function of time. One extra monitor point (monitor point 9) was also introduced in the domain. The location of the monitor point 9 was 150 mm above the top most monitor point (monitor point 8) in the experiment. Figures 4.17 to 4.22 show the transient temperature prediction at monitor points 9 to 4, from all the four meshes. All the four meshes (*2M1, 2M2, 2M3* and *2M4*) used the same advection scheme (high resolution) and turbulence model (SST without buoyancy). Comparison of the axially refined meshes (*2M1, 2M2* and *2M3*) shows that all the three mesh show no deviation in the temperature prediction up to monitor point 7. However, the prediction with mesh 1 (*2M1*) showed a deviation of 1.2^0C as the thermal front reaches monitor point 6. The prediction from the other two axially refined meshes (*2M2* and *2M3*) showed consistent results up to monitor point 4. The results from the radially refined mesh (*2M4*) were also consistent with the results of *2M2* and *2M3.* The radially refined mesh (*M4*) showed a maximum deviation of 0.3^0C. Based on the distance of monitor point 7 (450 mm) from the top cover and the time taken by the thermal front (approximately 1.5 hr) to reach monitor point 7, it was decided to use Mesh 1 for further studies. However, the predictions from mesh 1 were only considered up to monitor point 7. For predictions beyond monitor point 7, mesh 2 was used.

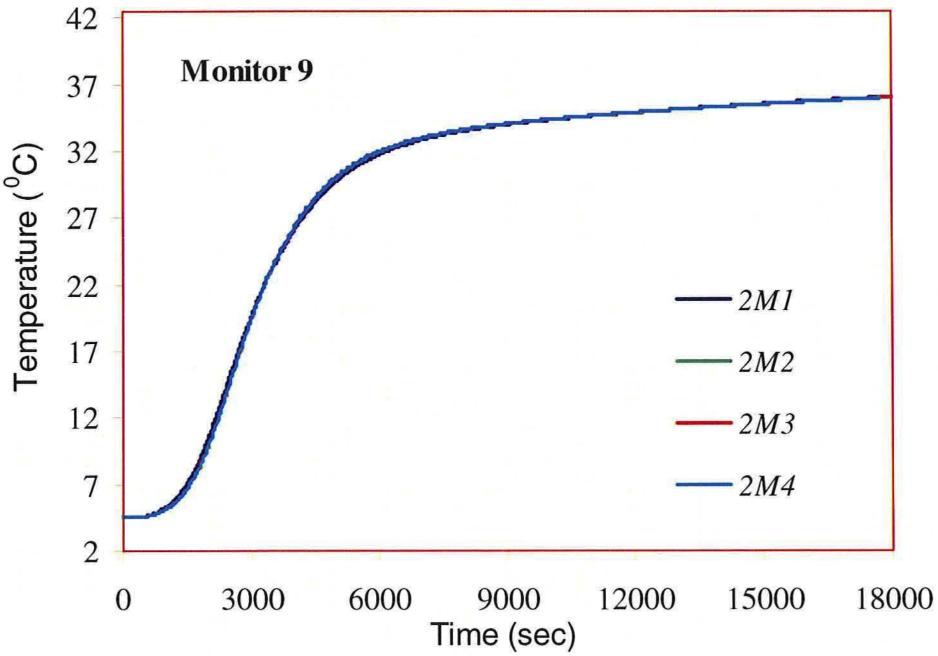

Figure 4.17: Transient Temperature at Monitor Point Nine Case II.

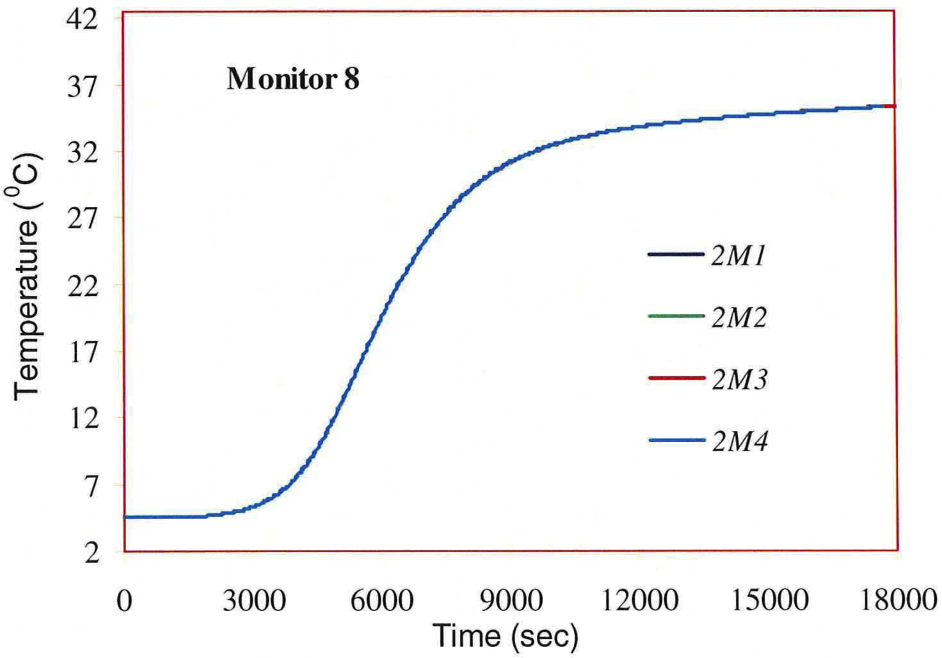

Figure 4.18: Transient Temperature at Monitor Point Eight Case II.

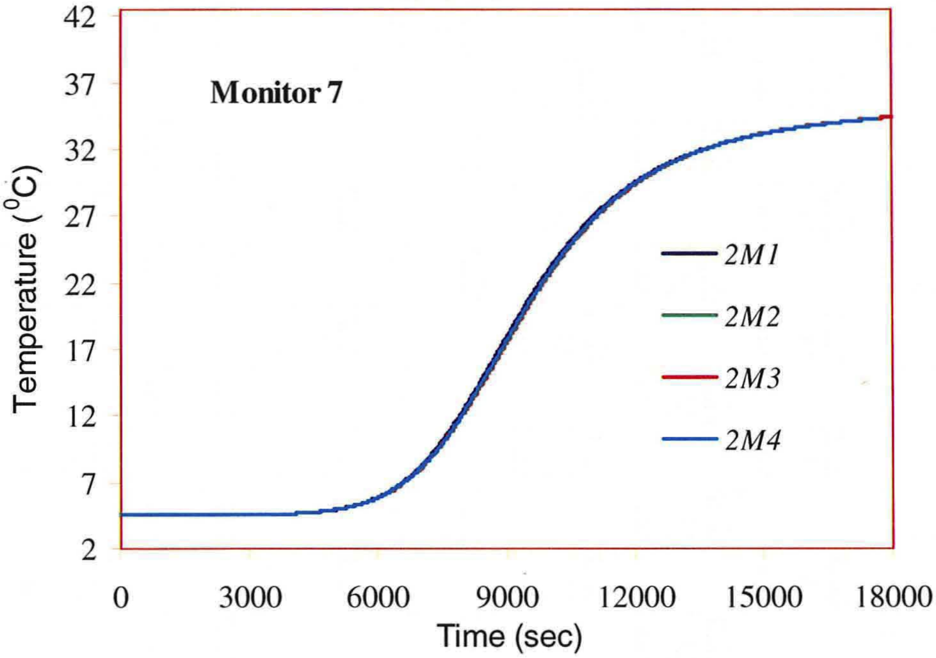

Figure 4.19: Transient Temperature at Monitor Point Seven Case II.

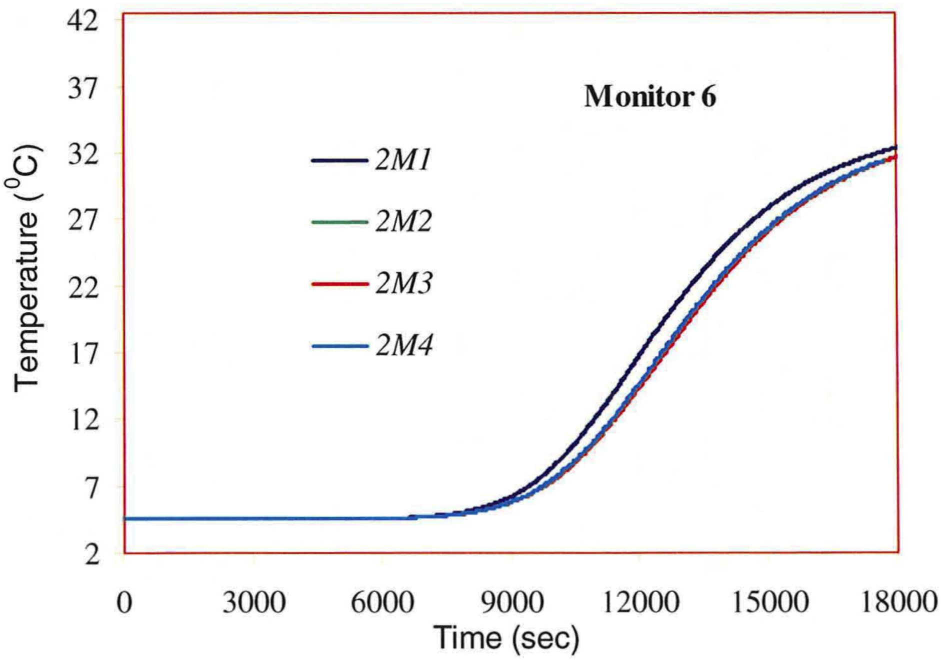

Figure 4.20: Transient Temperature at Monitor Point Six Case II.

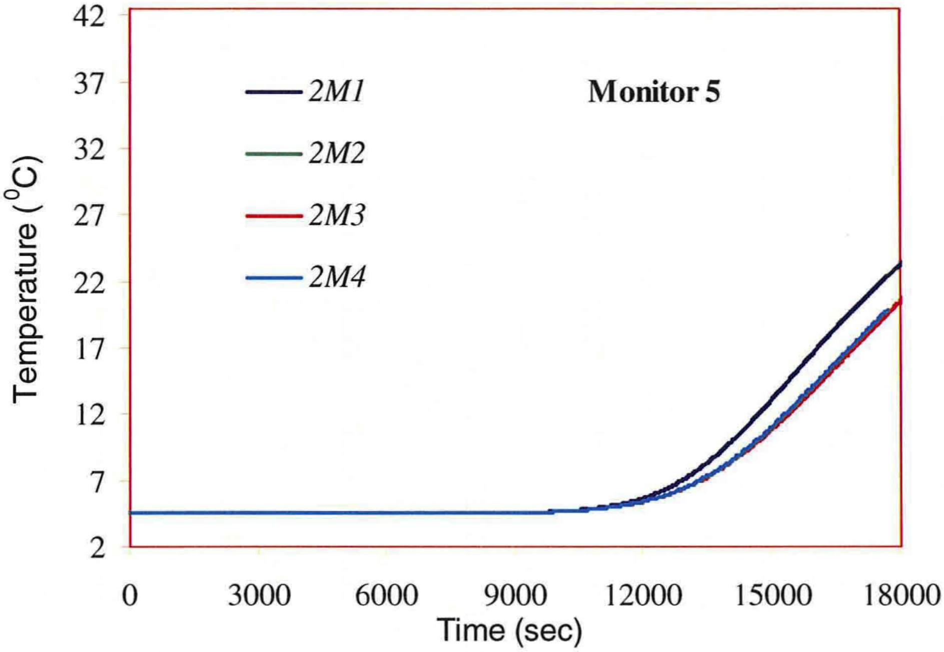

Figure 4.21: Transient Temperature at Monitor Point Five Case II.

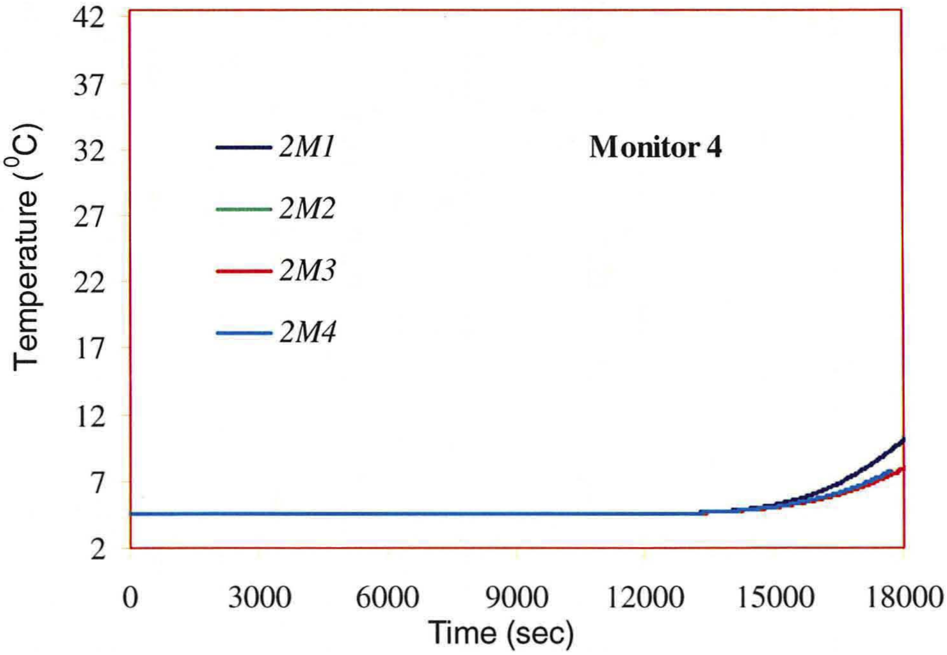

Figure 4.22: Transient Temperature at Monitor Point Four Case II.

Turbulence Models Validation with the Experiment

Figures 4.23 and 4.24 compare the predicted transient temperature at two monitored points with the experimental results of Case II. In contrast to the results of Case I, simulation *2S2* SST (buoyant) and simulation *2S3* with k-ε (buoyant), produced poor predictions. However, predictions from both these models were similar to each other as in the results from Case I. The presence of the buoyancy term in these two models appeared to suppress the turbulence and the result was closer to the laminar case *2S1*. Simulation *2S4* produced the best prediction of the slope of the thermocline. Although the results of *2S4* were under-predicted at monitor points 8, over-predicted at monitor point 7 and a maximum deviation of 4^0C was observed, the *temperature-time* relationship (slope of the curves) were in good agreement with the experiment.

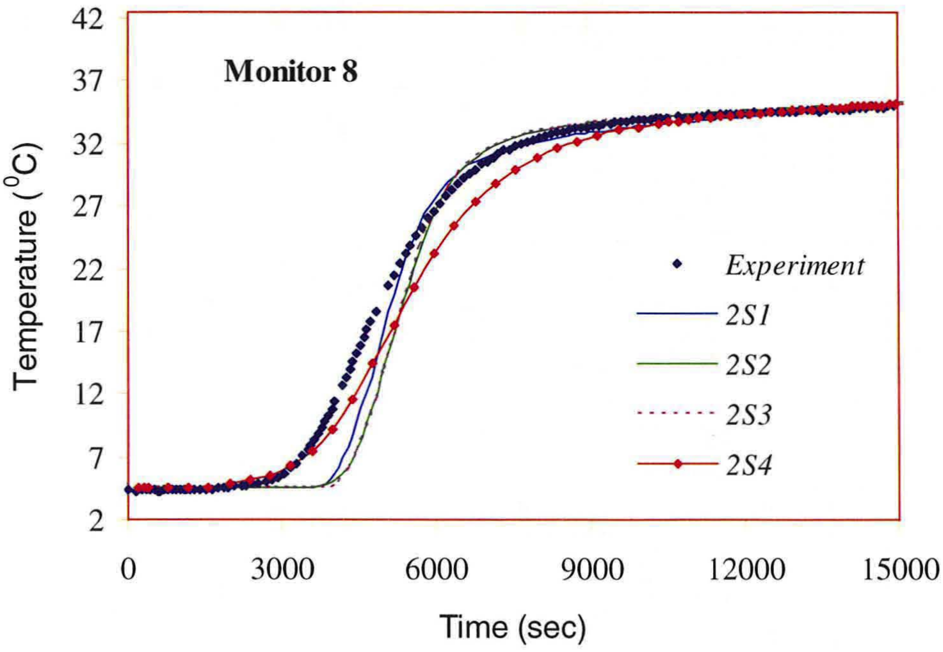

Figure 4.23: Transient Temperature at Monitor Point Eight Case II.

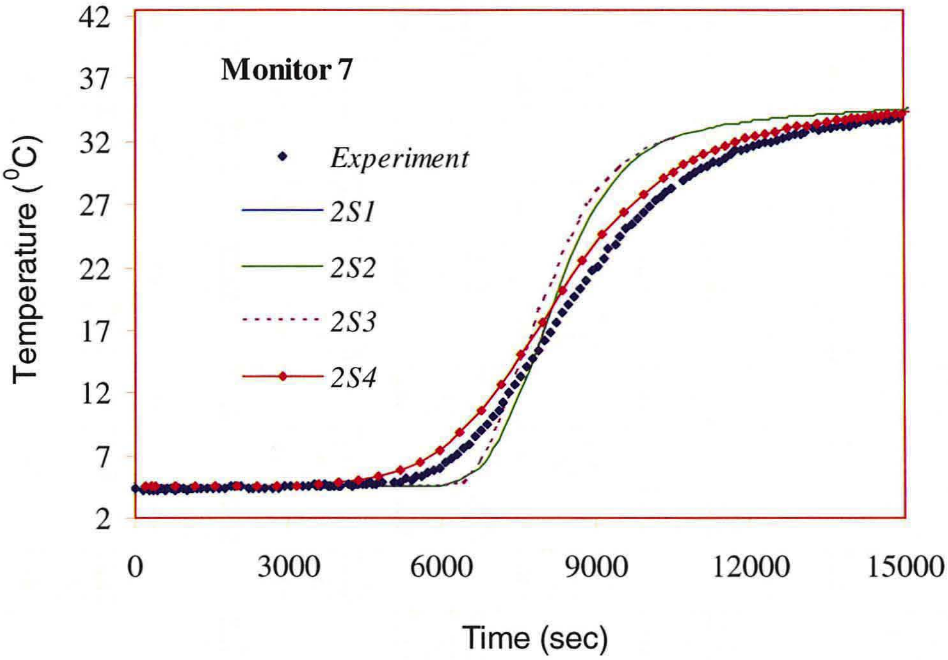

Figure 4.24: Transient Temperature at Monitor Point Seven Case II.

Since the results of simulations *2S2* and *2S3* were similar for monitor points 8 and 7, comparisons for the turbulence models in the rest of the TST were performed with simulations *2S2* and *2S4*. Figures 4.25 to 4.26 compare the transient temperature prediction at monitor points 6 and 5 with the experimental results. The results at these monitor points were over predicted, however the *temperature-time* relationship was consistent with the results at monitor points 8 and 7, i.e. the prediction of the change of temperature with time was better for the simulation *2S4* than *2S2*. After assessing the results at monitor points 6 and 5, it cannot be concluded whether the SST with the buoyancy term or the SST without the buoyancy term had better prediction. Therefore, to conclude which model had better prediction further analysis was performed.

Recall the experimental uncertainties discussed in the section experimental setup (Section 4.3.1):

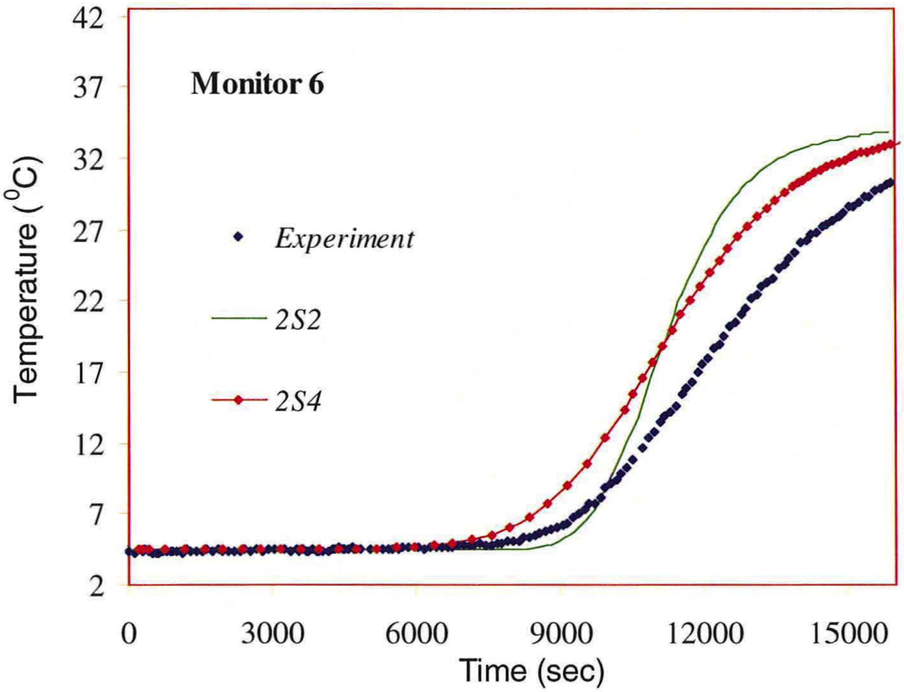

Figure 4.25: Transient Temperature at Monitor Point Six Case II.

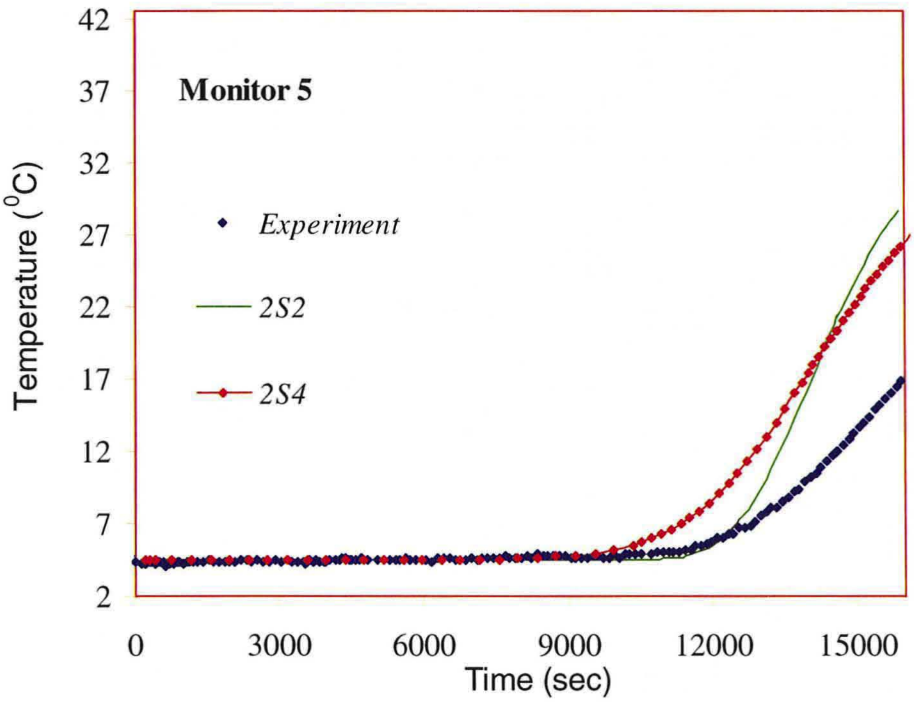

Figure 4.26: Transient Temperature at Monitor Point Five Case II.

1. Uncertainty associated with displacement of the thermocouples in the tank. In this regard a monitor point (6') was considered 75 mm below the monitor point 6. Figure 4.27 shows the comparison of the transient temperature at the monitor point 6, 6' and experimental monitor point 6. It can be seen that the temperature prediction at monitor point 6' is close to the experiment. Also, the temperature prediction at monitor point 6' shows *temperature-time* relationship similar to the experimental monitor point and monitor point 6. Therefore it can be concluded that a better alternative to analyze the temperature prediction in presence of the uncertainty is by considering the *temperature-time* relationship rather than considering the deviation in temperature at a particular location.

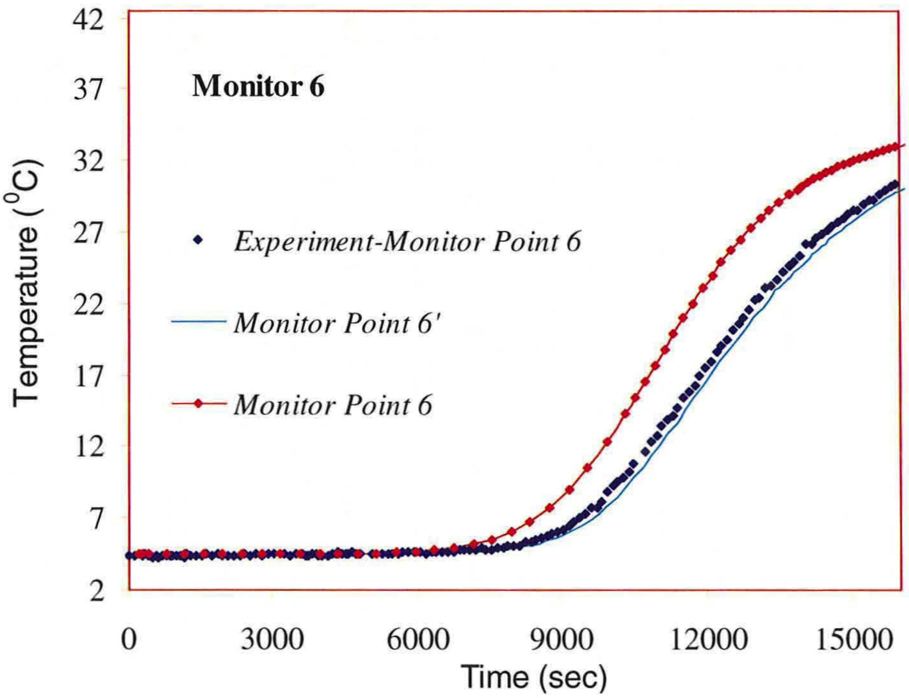

Figure 4.27: Transient Temperature at Monitor Point Six Case II.

2. The temperature at monitor points 7, 6 and 5 was over-predicted, the results suggested that the energy level in the experimental TST might be less than the energy level of the TST in the simulations, i.e. there may be a problem with the boundary condition *B1*. If it was true that the energy level of the TST in the simulation and the experiment was not equal, the cause of such discrepancy would be the heat exchanger's outlet temperature in the TST loop and the flow rate in the TST loop. The heat exchanger's outlet temperature in the TST loop was measured in the experiments and moreover, the simulation results of the temperature at different monitor points in the quasi-steady state, i.e. the state when the transient temperature at different monitors changed negligibly, are in agreement with the experimental results. Hence, it is concluded that the temperature of the fluid going into the TST was identical in the simulation and the experiment. In the experiment, the mass flow rate in the TST loop was calculated based on the energy balance with the collector loop of the heat exchanger. The calculated flow rate was not determined physically in the experiment as confirmed by the experimentalist. Hence, an analysis was performed to observe whether the *temperature-time* relationship observed with the inlet boundary condition *B1* could be maintained when the inlet flow rate is reduced and the inlet temperature is kept identical. The inlet temperature applied through the inlet boundary condition *B2* (inlet boundary condition based on the experimental correlation) was identical with the inlet temperature applied through the inlet boundary condition *B1*. However, the inlet flow rate applied through the inlet boundary condition B2 was 10 to 15% less than the flow rate applied through the inlet boundary condition B1. Further details on the result of the inlet boundary condition

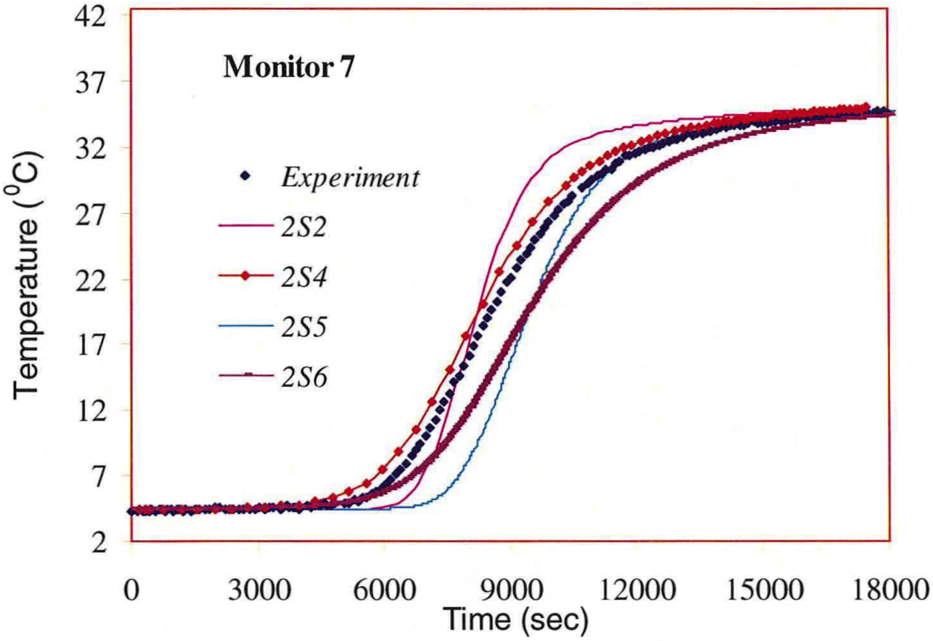

Figure 4.28: Transient Temperature at Monitor Point Seven Case II.

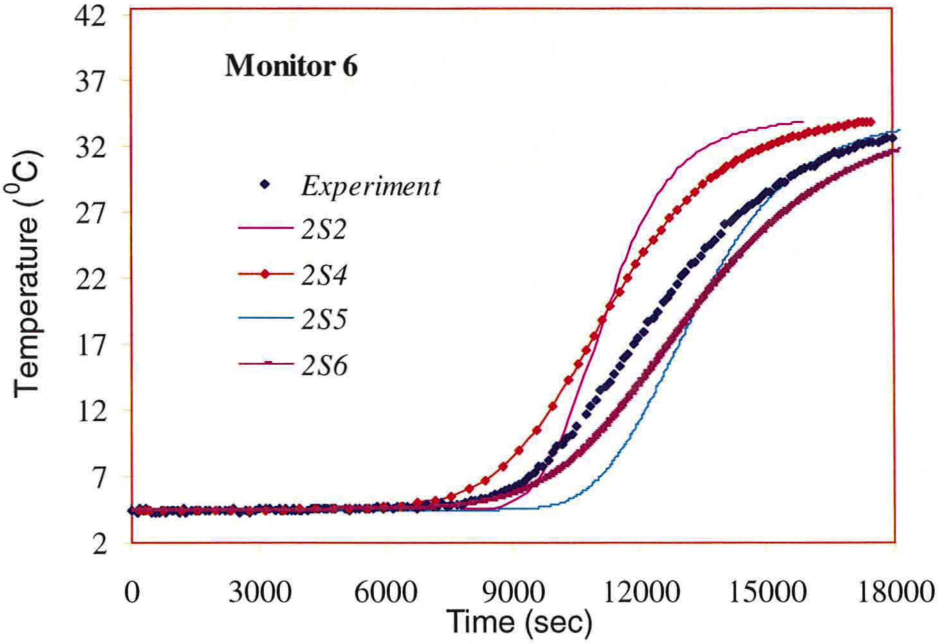

Figure 4.29: Transient Temperature at Monitor Point Six Case II.

B2 is provided in appendix A. Figure 4.28 and 4.29 show the comparison of the temperature prediction from simulations *2S2* (SST buoyant) and *2S4* (SST non-buoyant) with inlet boundary condition *B1*, simulations *2S5* (SST buoyant) and *2S6* (SST non-buoyant) with inlet boundary condition *B2* and the experimental prediction at monitor points 7 and 6, respectively. The results show that the *temperature-time* relationship of simulation *2S2* is similar to simulation *2S5* while simulations *2S4*, *2S6* and the experimental temperature prediction show similar *temperature-time* relationship.

From the analysis of the experimental uncertainties it was concluded that *temperature-time* relationship provide better analysis of results when compared to the analysis of temperature deviation at a particular location. Based on this argument it was concluded that at low inlet Reynolds number, the temperature predictions with SST non-buoyant is better than the SST buoyant.

Effect of the Turbulence Buoyancy Term on the Inlet Jet Mixing

In the previous section it was shown that the presence of the buoyancy term in the turbulence equations of the model causes less mixing represented by the steeper *temperature-time* relationship. Therefore, a comparative study was performed to highlight the mixing mechanism which resulted in the difference. The nature of the turbulence buoyancy term is to increase turbulence in the unstable stratified flow region to reduce turbulence in the stable stratified region. Figures 4.30 to 4.35 compare the temperature and normalized eddy viscosity (normalized with dynamic viscosity) distributions in the jet affected region near the inlet in the top region of the TST for simulations *2S5* and *2S6* at few initial time intervals. Vertical and horizontal lines were drawn in the contours at 19 mm and 50 mm away from TST center line and from TST top cover, respectively, to demarcate the plume region from the rest of the TST. It can be seen that at all time intervals, predictions of the eddy viscosity within the plume region are similar in both; *2S5* and *2S6* results. This resulted in the similar temperature distribution within the plume region for both the simulations. However, in the region outside the plume (shown with dotted circle), where the hot fluid coming out of the plume mixes with cold fluid in the TST, the prediction of the eddy viscosity in simulation *2S5* (without buoyancy) is higher (approximately 4 times higher) when compared to the eddy viscosity predictions of simulation *2S6* (with buoyancy). This resulted in the smearing of the temperature contour in simulation *2S5* when compared to the temperature contour from simulation *2S6*. For the same reason, the temperature distribution shown in figures 4.23 to 4.26 and figures 4.28 and 4.29 showed steeper slopes for the simulation with SST (without buoyancy) when compared to the simulation with SST (with buoyancy). The results also revealed that the effect of the turbulence buoyancy term is negligible on the jet penetration depth.

4.4 Conclusion

In this chapter the effect of various computational fluid dynamics parameters on the study of vertical inlet jet SDHW system was discussed. It was shown that for the high inlet Reynolds number, turbulence models with buoyancy term in the production and dissipation gave better prediction for the temperature distribution inside the TST, while for the low inlet Reynolds number, SST without the buoyancy term in the turbulence equations gave better prediction. It may also be added that the results with the second

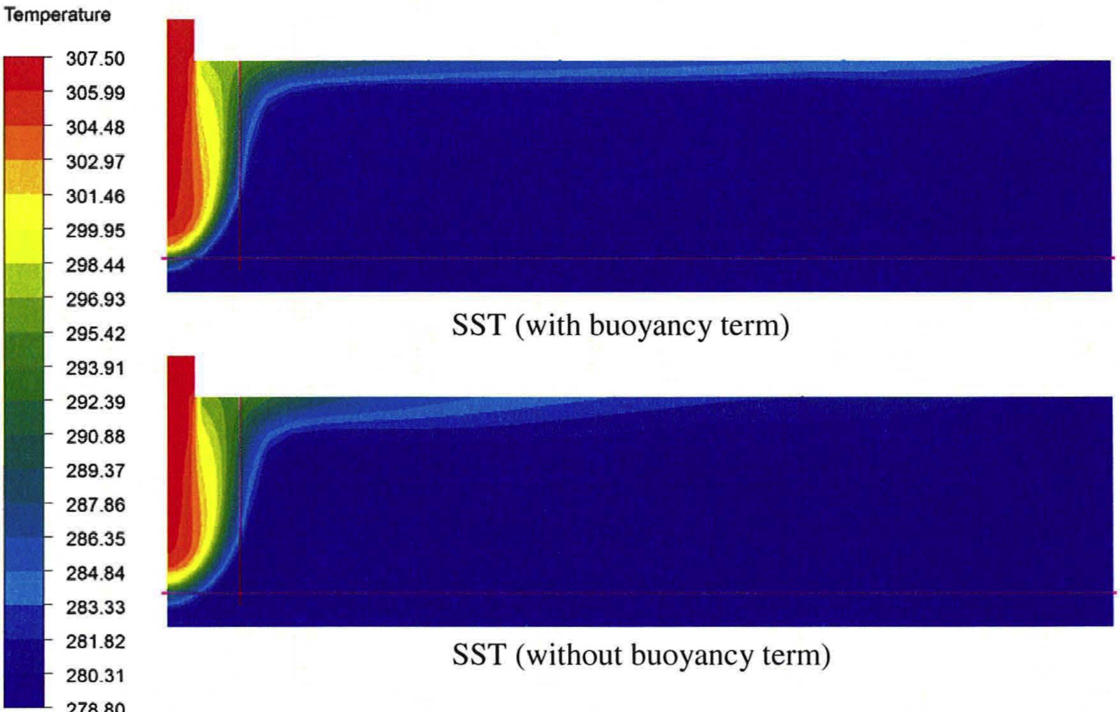

(a)

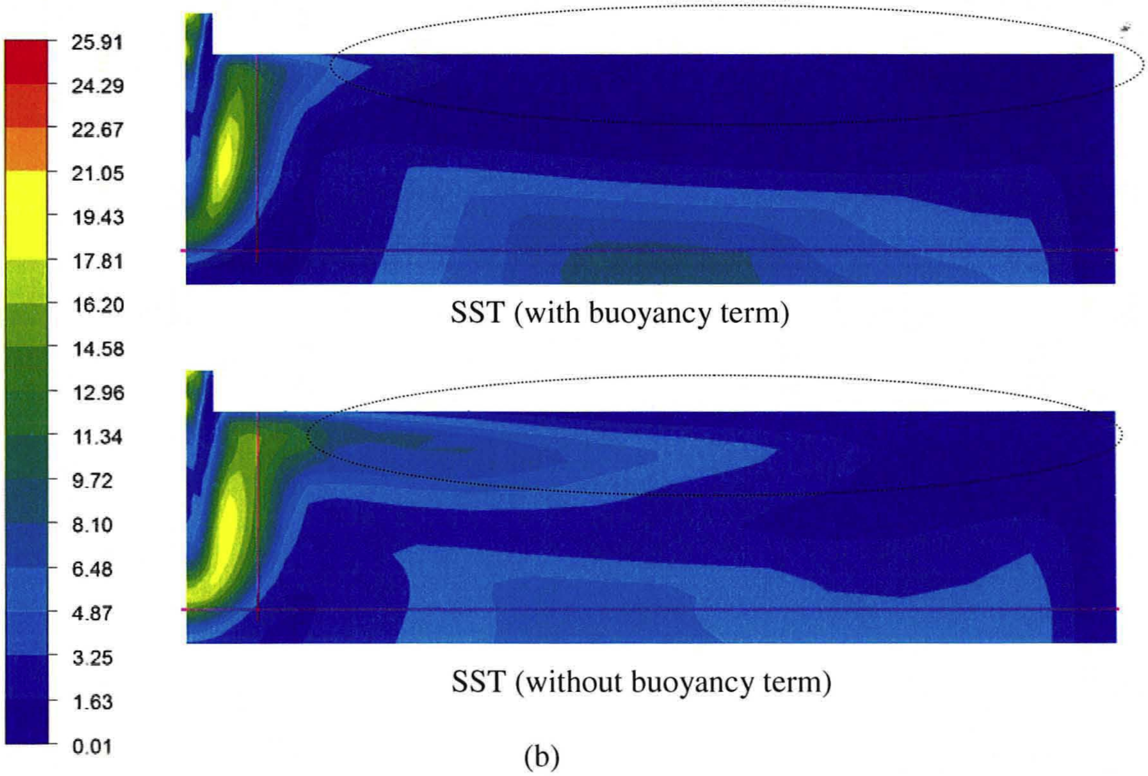

(b)

Figure 4.30: (a) Temperature (b) Eddy Viscosity at 30 s.

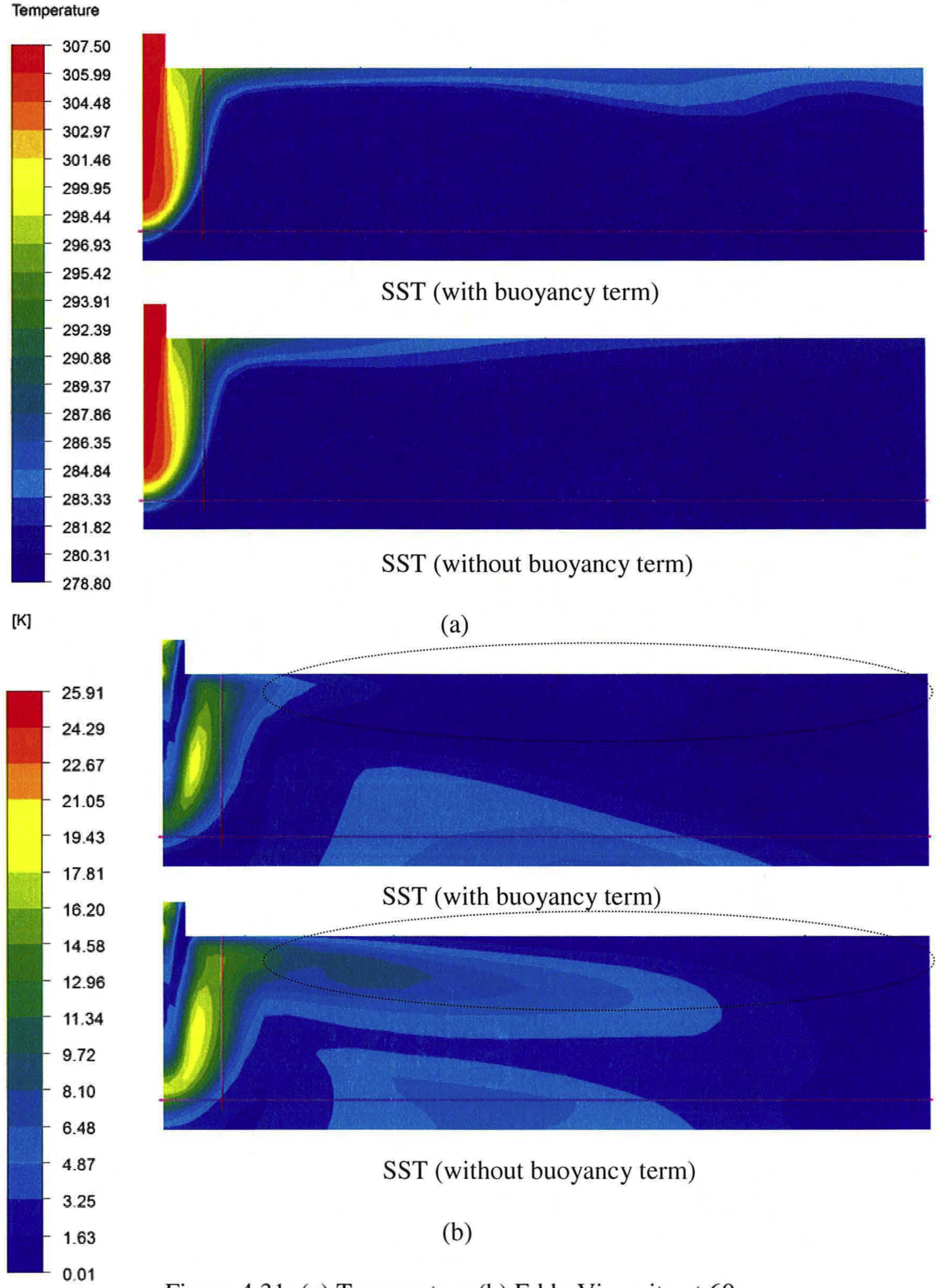

Figure 4.31: (a) Temperature (b) Eddy Viscosity at 60 s.

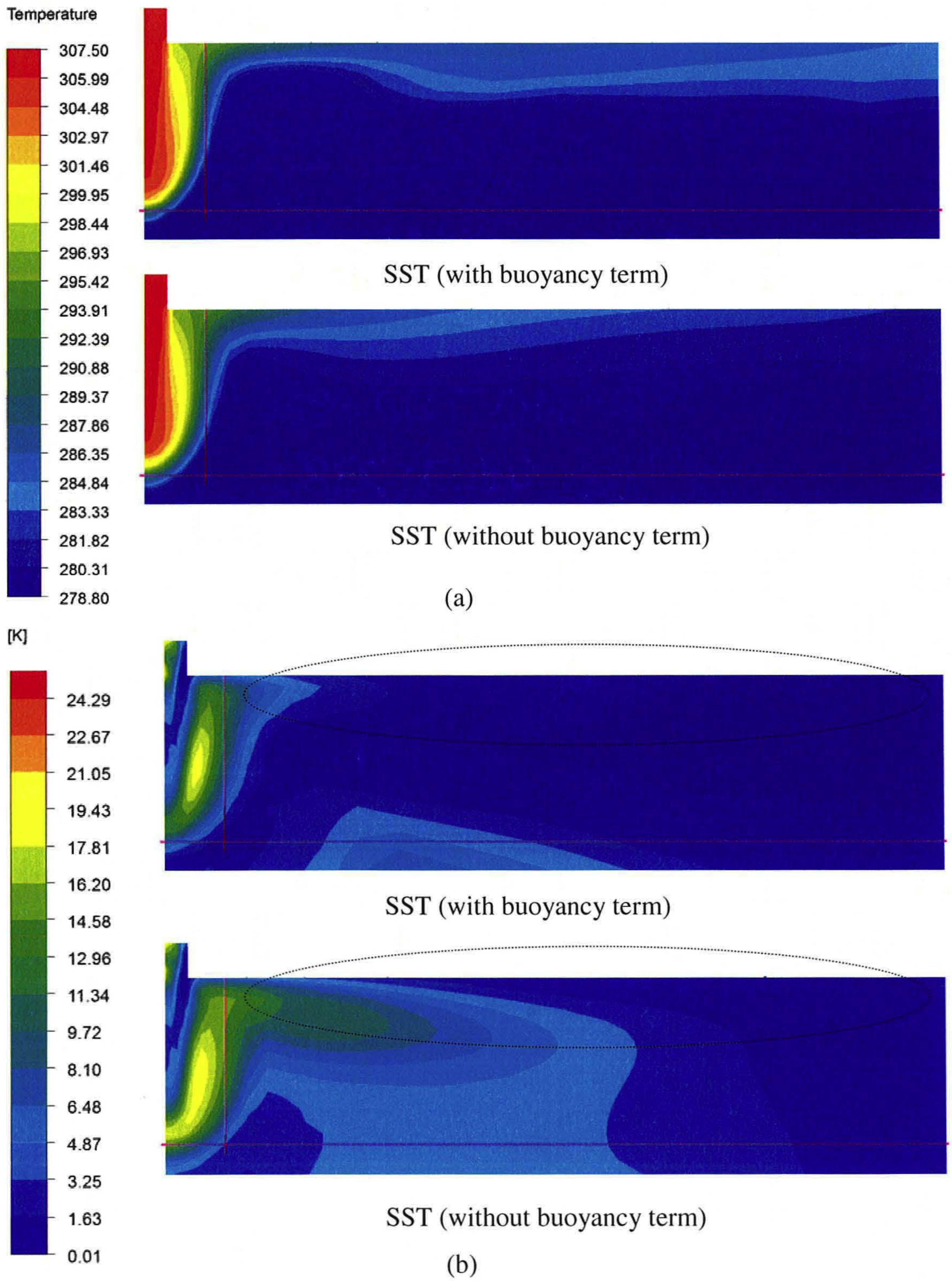

Figure 4.32: (a) Temperature (b) Eddy Viscosity at 90 s.

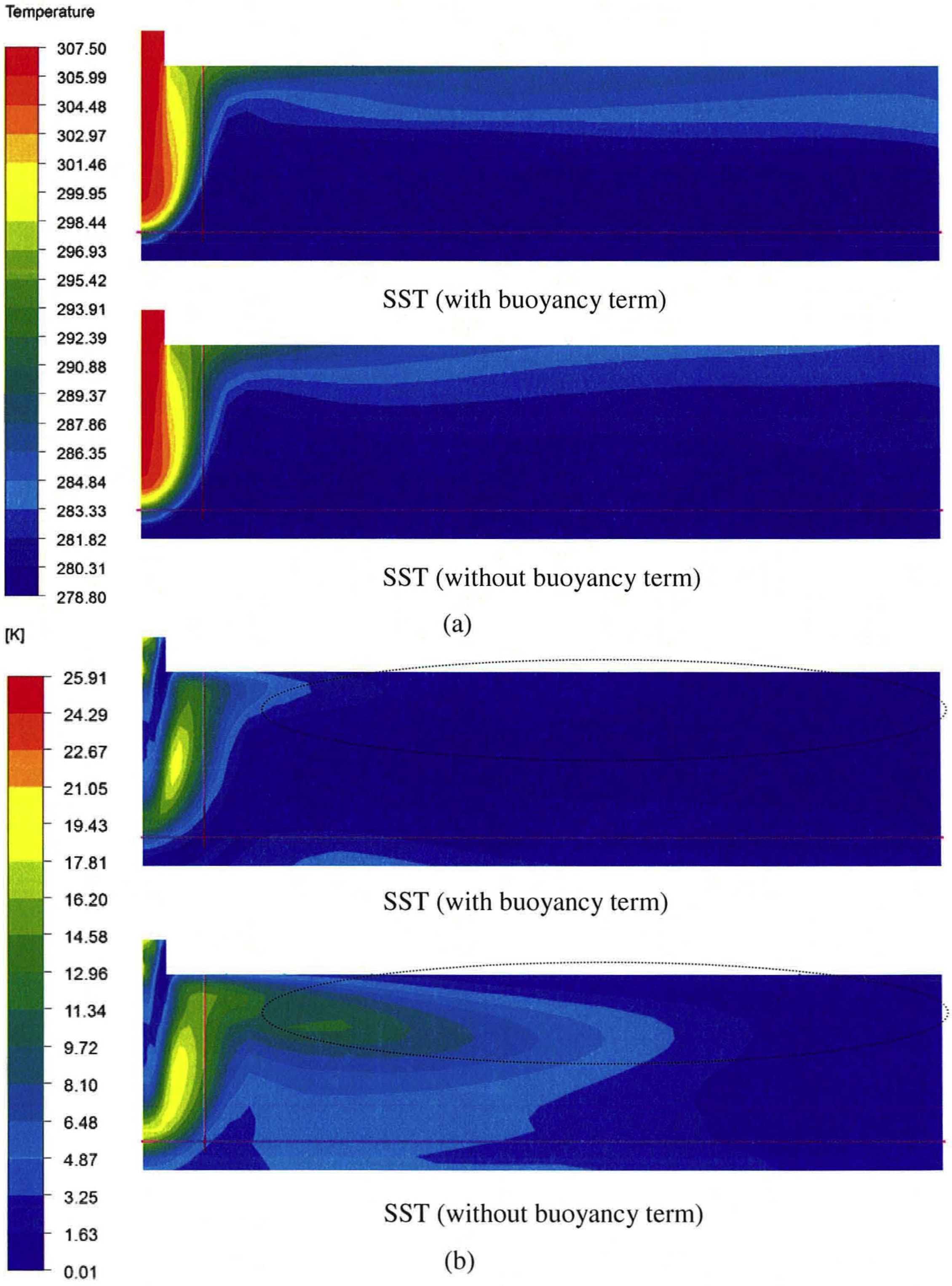

Figure 4.33: (a) Temperature (b) Eddy Viscosity at 120 s.

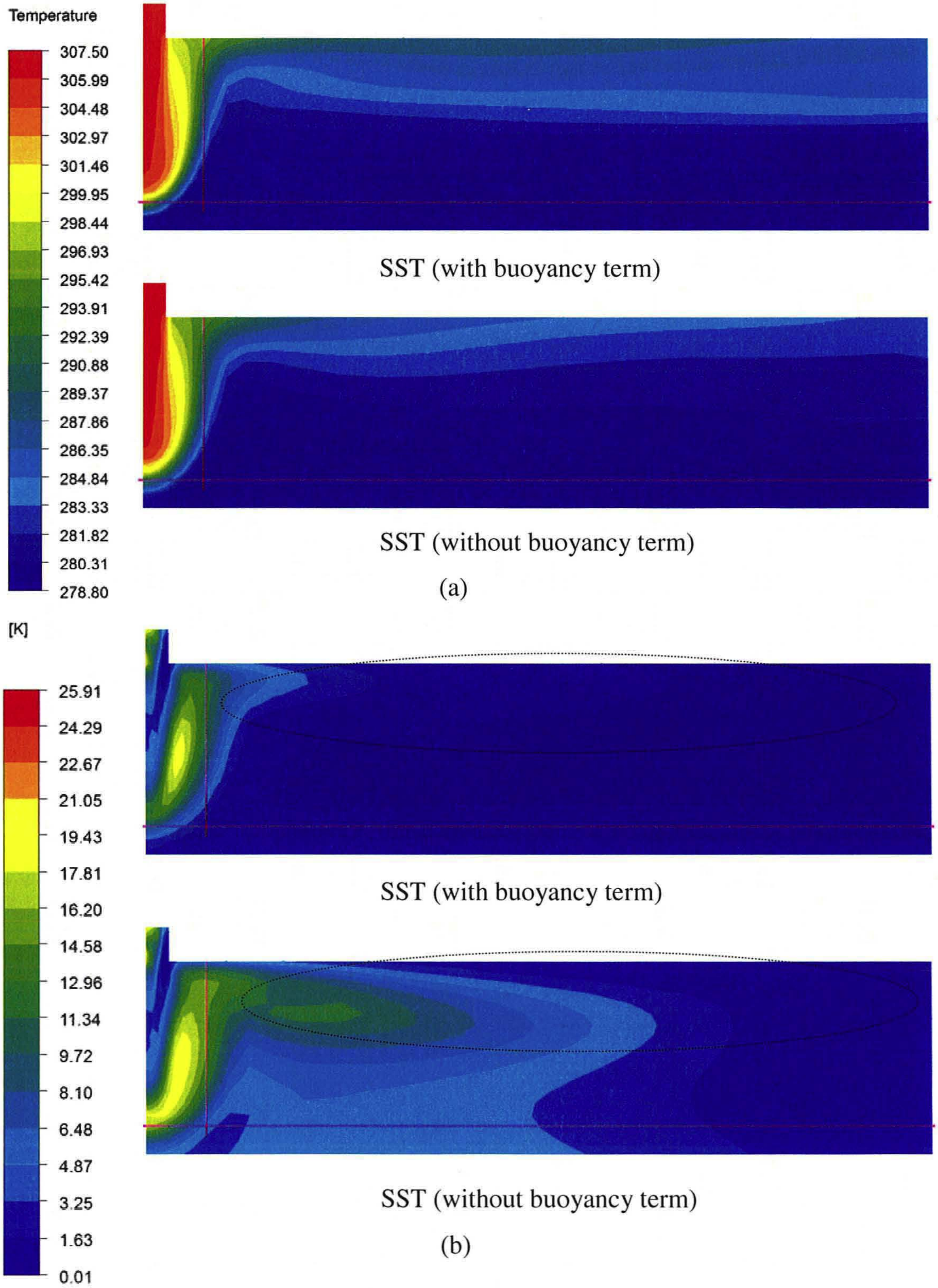

Figure 4.34: (a) Temperature (b) Eddy Viscosity at 150 s.

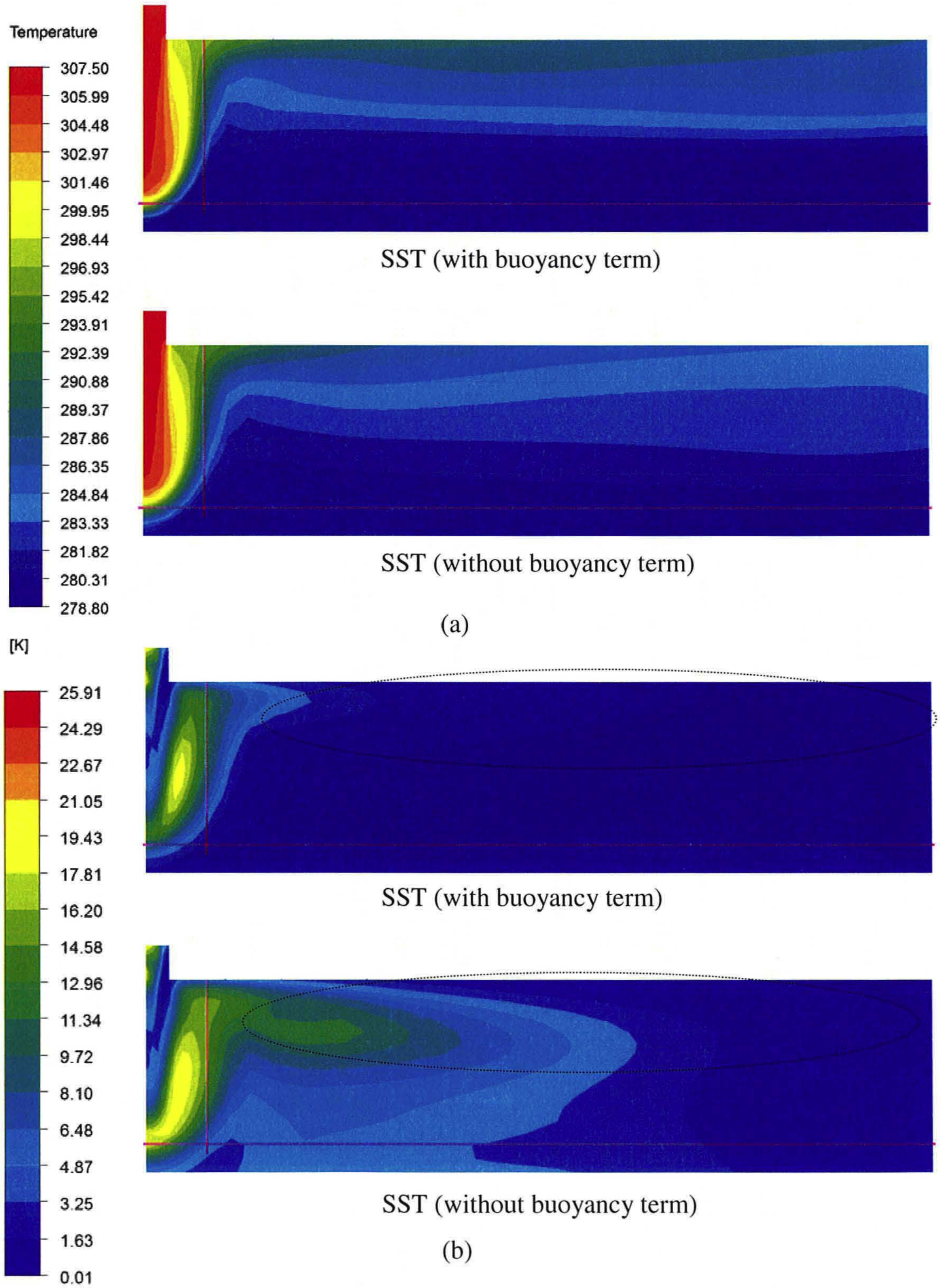

Figure 4.35: (a) Temperature (b) Eddy Viscosity at 180 s.

order accurate in space advection scheme and the high resolution scheme were more reliable than in the case of the first order upwind scheme.

CHAPTER 5

System Model

5.1 Overview

System simulation codes which are used to predict the long term performance of solar energy system over long time periods (i.e. annual performance) require simple models that can predict the thermal stratification in the TST. Two and three dimensional CFD simulations are computationally expensive and hence not suitable for incorporation into system codes. Chapter two presented the one dimensional models developed by various authors. Most of the inlet mixing models proposed by various authors considered horizontal inlets or inlet configurations which avoid mixing. Differences in the models pertain to the treatment of the mixing caused by the temperature difference between the inlet and the existing temperature in the tank. To the best of author's knowledge there is no one dimensional model which handles the mixing caused by the negative buoyant plume (The nomenclature: negative buoyant plume, is adapted from the studies of fountains, wherein a fountain whose momentum is in opposite direction to the direction of buoyancy is termed a negative buoyant fountain [71].). There is thus a need for development of integrated models that capture the essential physics of the fluid flow and heat transfer for mixing caused by the negative buoyant plume in a TST. In this chapter, the temperature and velocity distribution for both the cases, namely Case I (fixed inlet condition) and Case II (variable inlet condition) are closely examined to gain insight into the fluid flow and heat transfer physics. The parametric study on the behavior of the negative buoyant plume and the one dimensional modelling of the TST will be also presented.

5.2 One Dimensional Nature of the Fluid Temperature Distribution

Figures 5.1 to 5.4 show the transient temperature and velocity vectors inside the TST for Case I's (fixed inlet condition). Note that the magnitude of the velocity is indicated by the colour of the arrow, rather than the arrow length. This penetration depth of the jet (h_j) is also indicated on the figures. This depth is defined for the current study as the length extending from the inlet to the point where the jet changes its direction along the centerline. Recall that for Case I the incoming jet has high momentum and the temperature of the jet is higher than the temperature of the fluid in the TST. The high momentum jet penetrates a certain depth in the TST, however due to the temperature difference between the incoming fluid and the fluid in the TST, a buoyancy force develops creating a force that opposes the jet momentum, thus forming a negative buoyant plume. The upward moving plume entrains and mixes with the fluid from the adjacent TST region. Thus, the circulation region is formed near the inlet due to the negative buoyant plume. The extent of the circulation region is approximately equal to the depth of the penetration. Further, it can be observed that the penetration depth of the jet has increased with time as a result of the reduced buoyancy force near the top of the TST.

Figures 5.5 to 5.11 show the transient temperature and velocity vectors inside the TST on the xy plane and the penetration depth of the jet for Case II (variable inlet condition). The flow pattern or the mixing caused by the incoming jet is similar to Case I (fixed inlet condition); a circulation region with a radial temperature distribution extending up to the jet penetration and one dimensional temperature distribution in the remaining TST can be observed in all the transient results. At long times, when the temperature difference between the inlet jet and the surrounding fluid has decreased, the negative buoyant plume behavior is still evident. For example, at a time interval of 7200 s (figure 5.8) the temperature difference is approximately less than 1^0C but a circulation region can be observed. Figure 5.12 shows the jet penetration depth as a function of time. The effect of the reduction in the flow rate which reduced the momentum of the incoming jet is seen in figure 5.12

This section examined the flow pattern and the mixing caused by a vertical inlet jet for two different inlet conditions. For both the systems, the flow pattern was similar and was driven by the penetration of the negative buoyant jet into the fluid in the TST. A circulation region is formed at the top of the TST in the vicinity of the jet. The extent of the circulation region or the jet penetration depth is governed by the balance of jet momentum and the buoyancy force due to the temperature difference between the incoming jet and the TST fluid. Two distinct regions of temperature distribution are also observed. These are the circulation region where the radial temperature distribution exists, and a region below it where the temperature distribution is essentially one dimensional. Hence in order to develop a one dimensional empirical model to predict the temperature distribution inside a TST, a number of assumptions are made and certain parameters have to be determined. The details of the modelling concept are discussed in the next section.

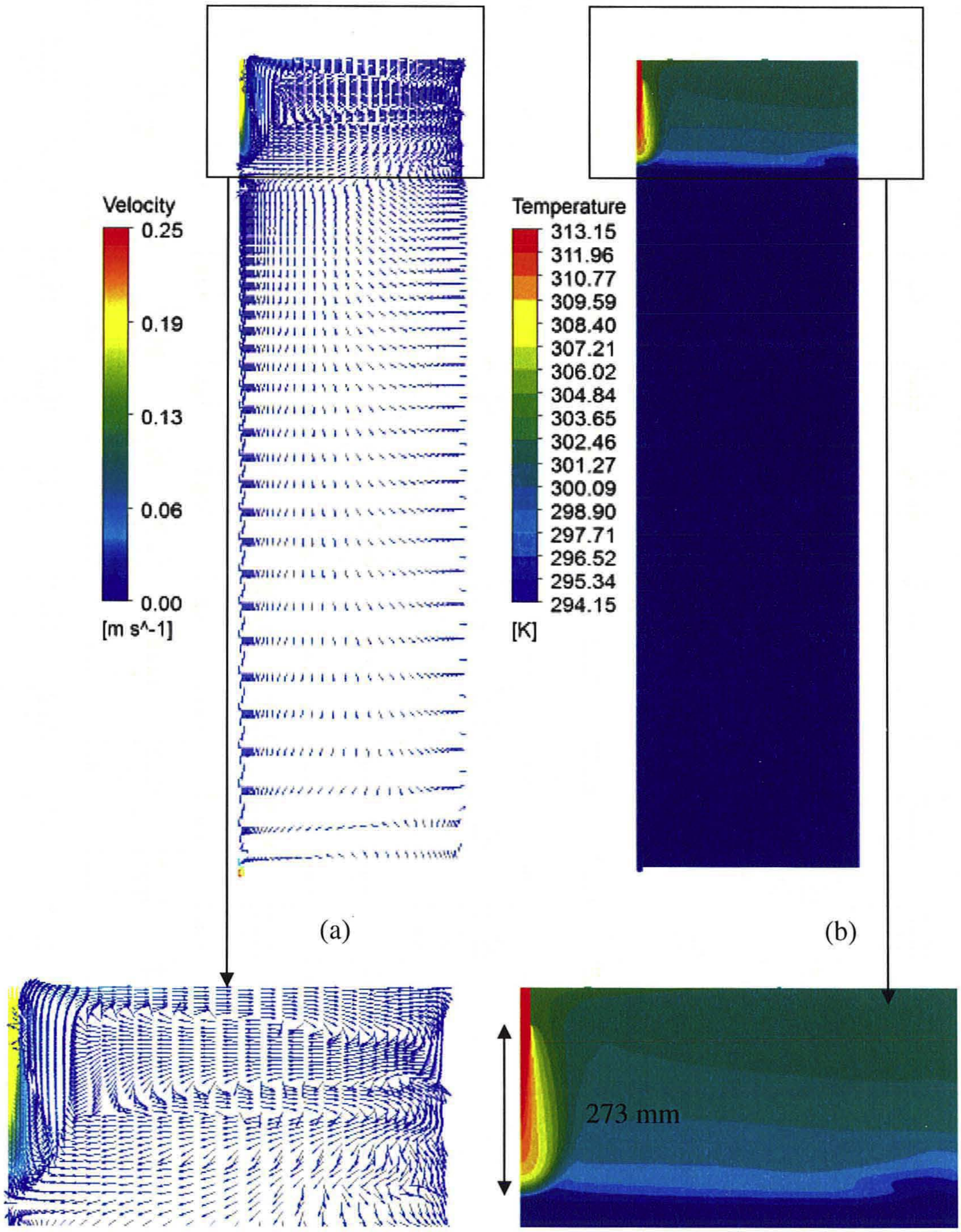

Figure 5.1: (a) Velocity Distribution, (b) Temperature Distribution after 900 s Case I.

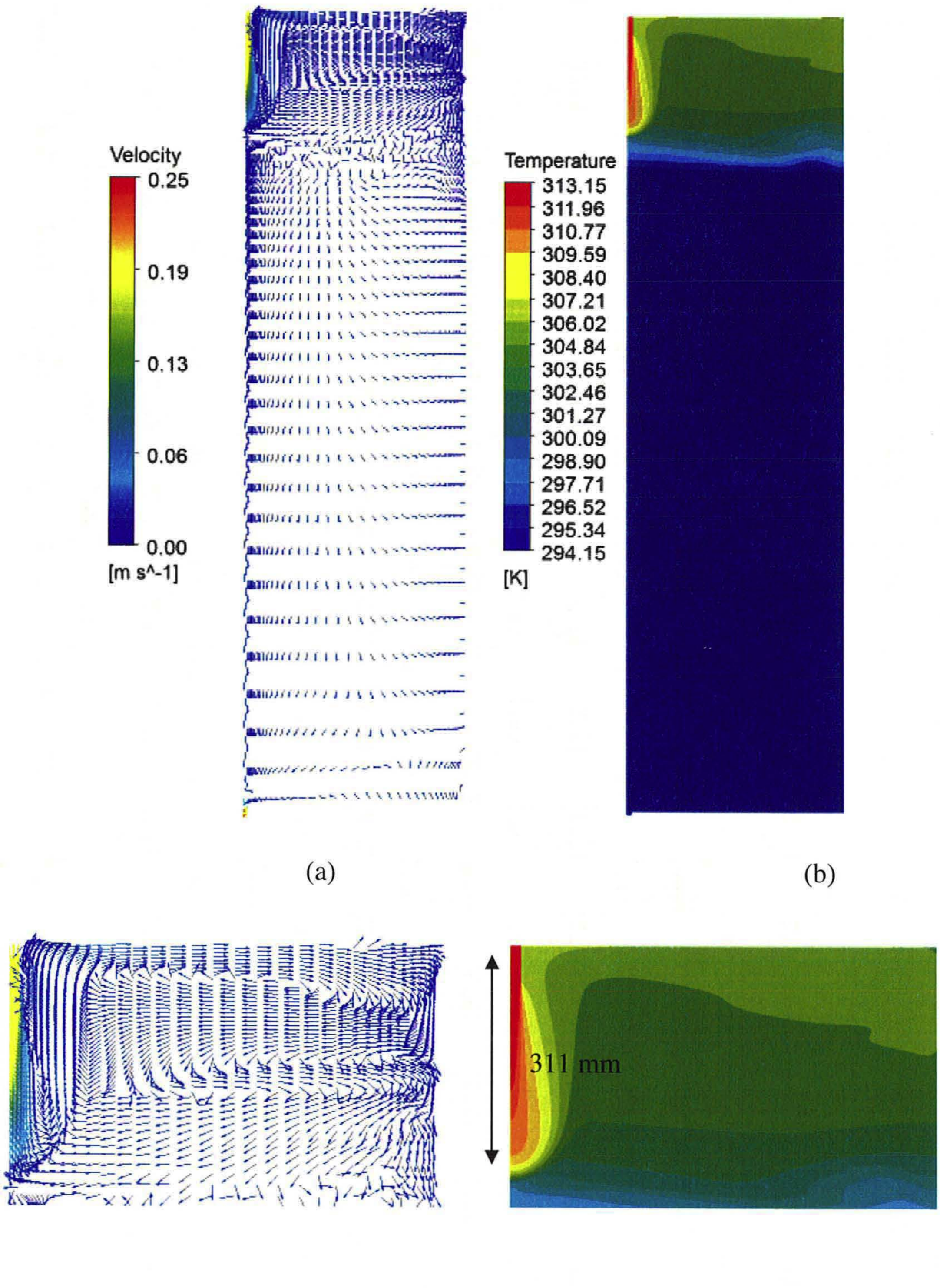

Figure 5.2: (a) Velocity Distribution, (b) Temperature Distribution after 1800 s Case I.

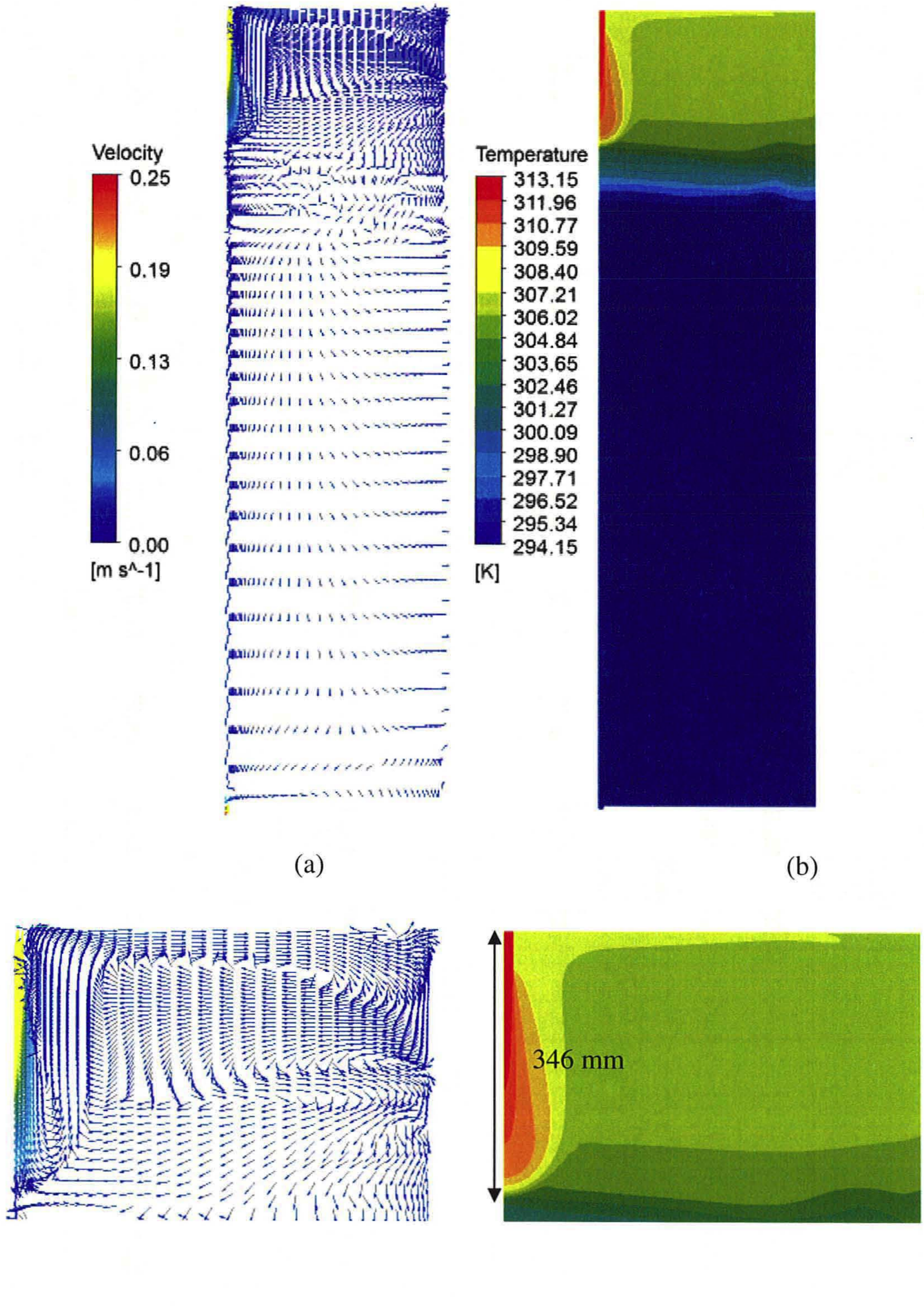

Figure 5.3: (a) Velocity Distribution, (b) Temperature Distribution after 2700 s Case I.

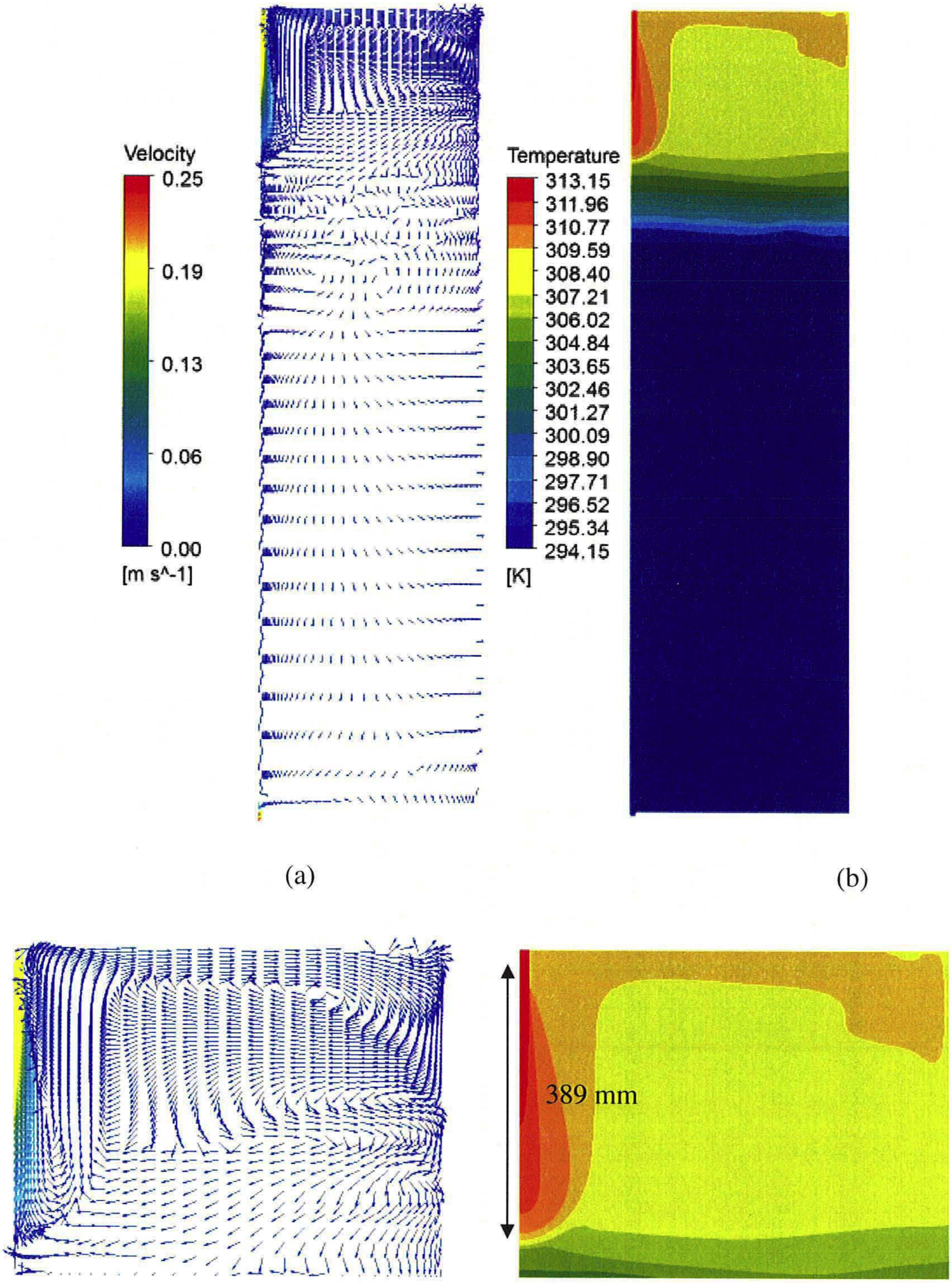

Figure 5.4: (a) Velocity Distribution, (b) Temperature Distribution after 3600 s Case I.

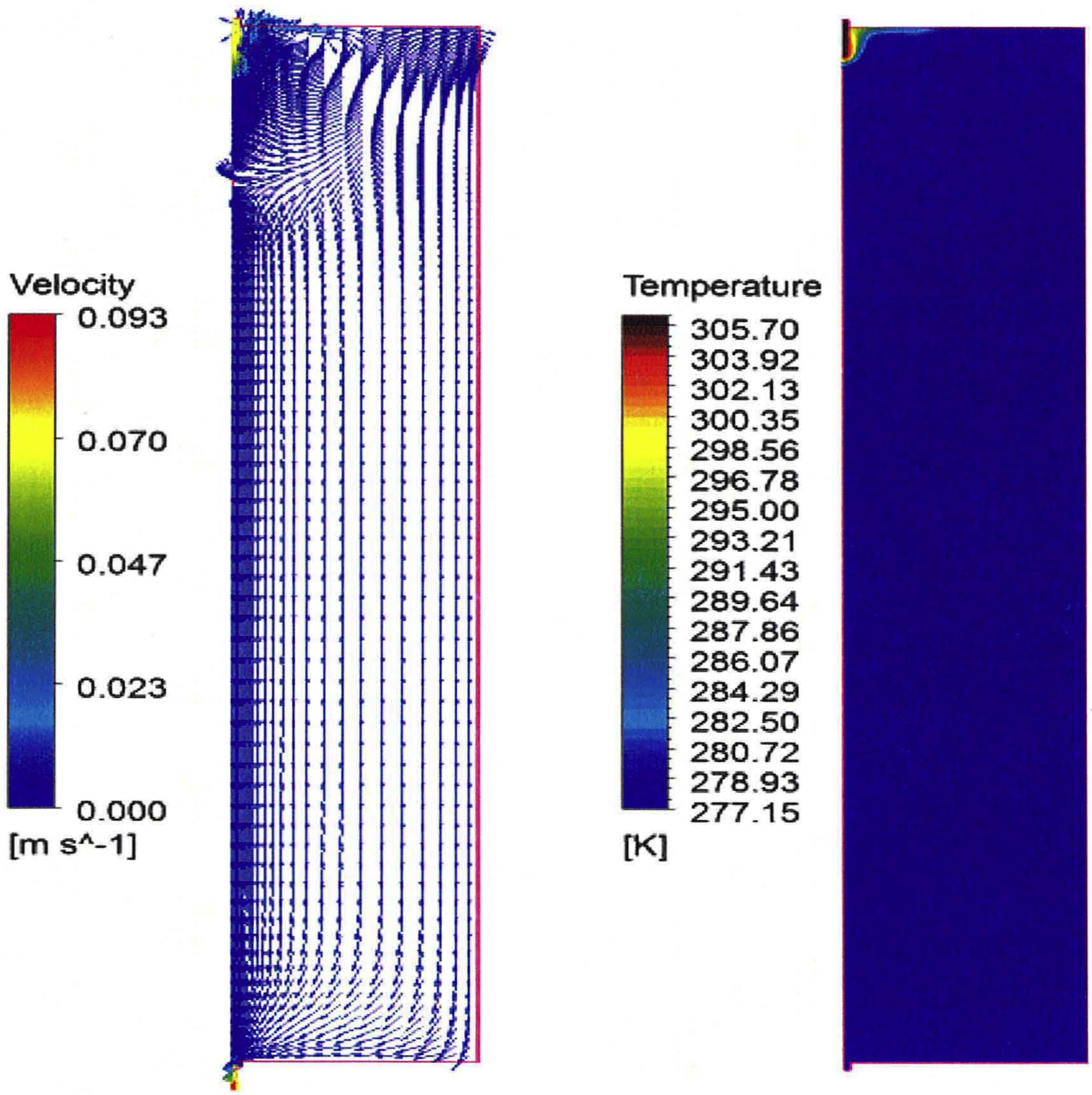

(a) (b)

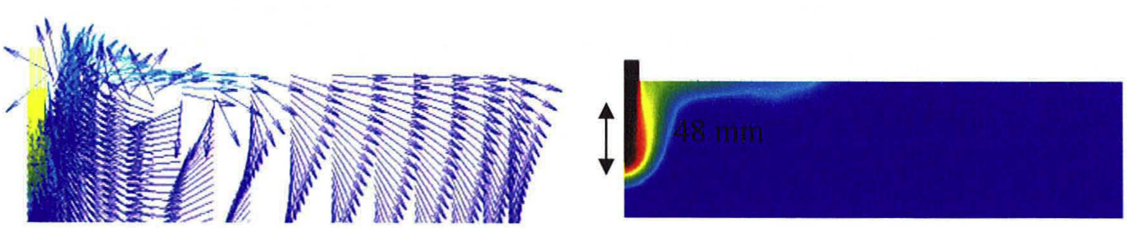

Figure 5.5: (a) Velocity Distribution, (b) Temperature Distribution after 300 s Case II.

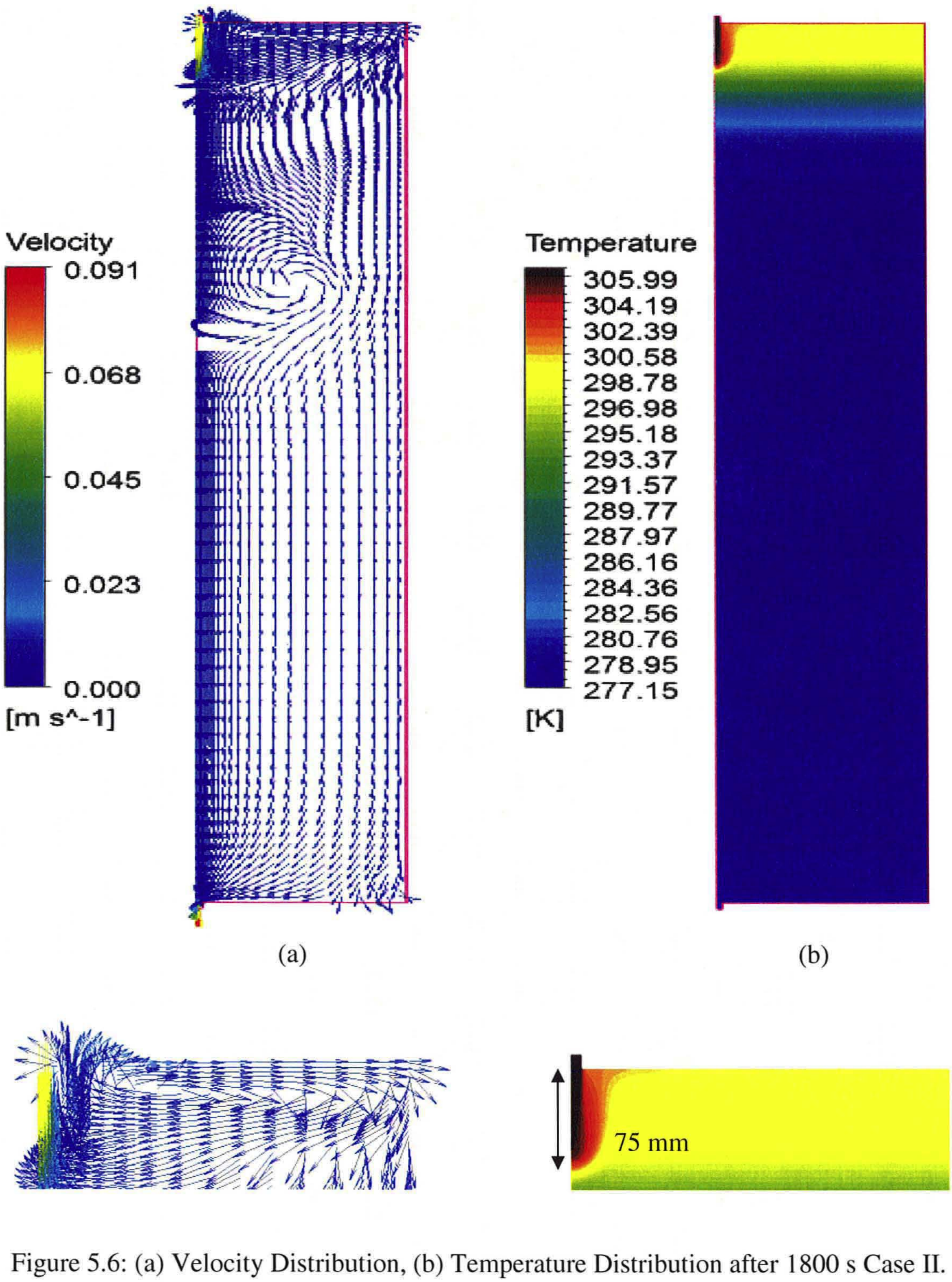

Figure 5.6: (a) Velocity Distribution, (b) Temperature Distribution after 1800 s Case II.

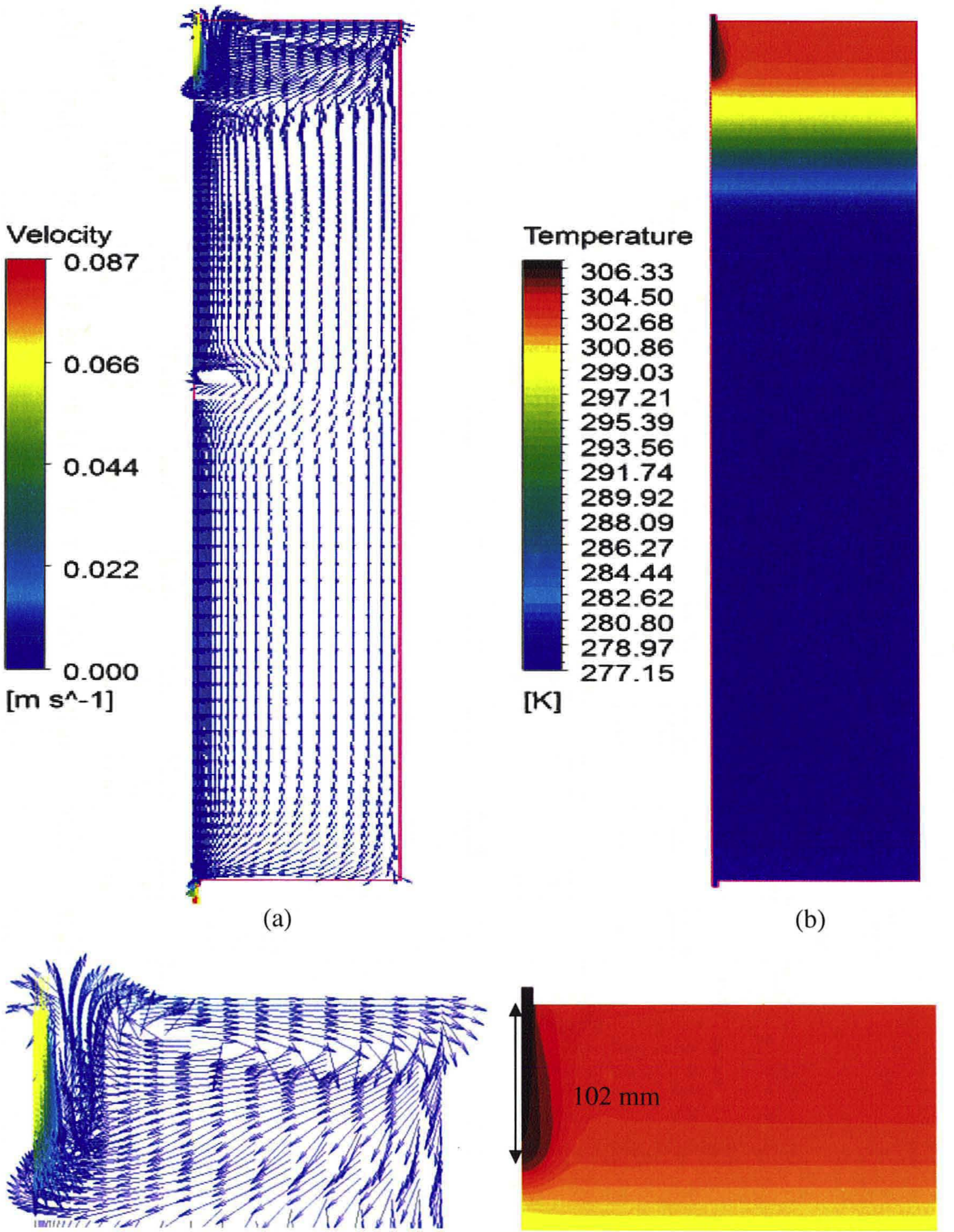

Figure 5.7: (a) Velocity Distribution, (b) Temperature Distribution after 3600 s Case II.

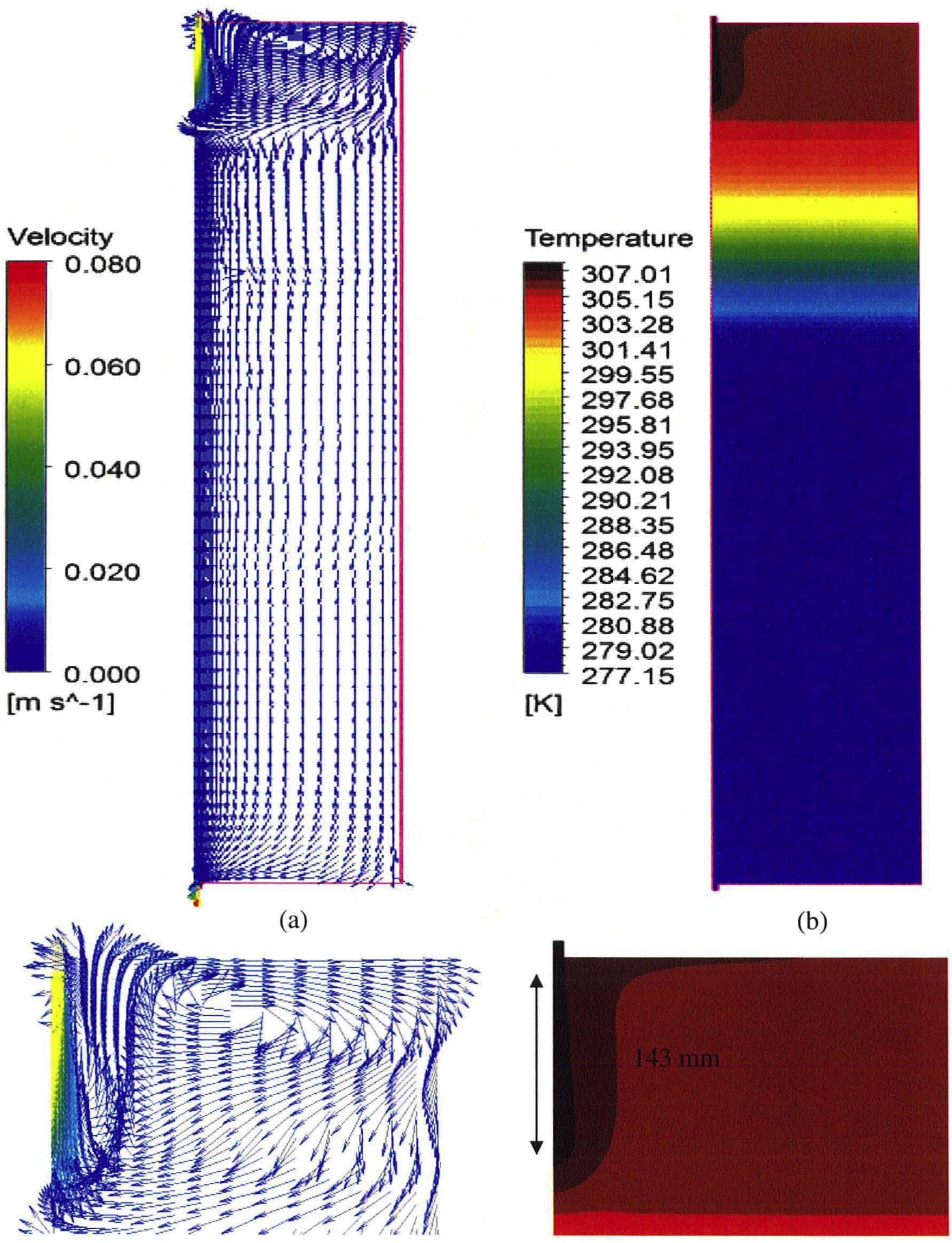

Figure 5.8: (a) Velocity Distribution, (b) Temperature Distribution after 7200 s Case II.

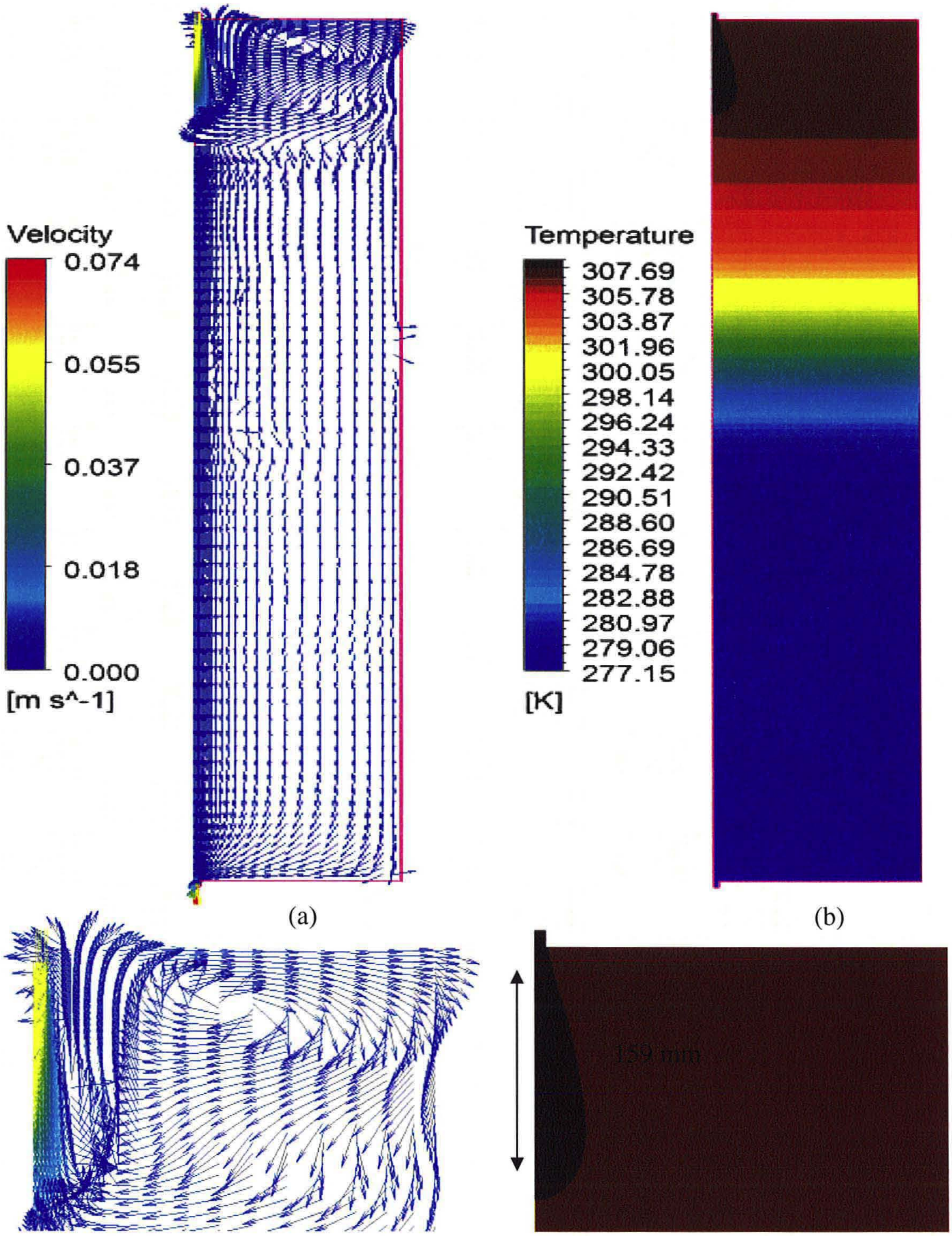

Figure 5.9: (a) Velocity Distribution, (b) Temperature Distribution after 10800 s Case II.

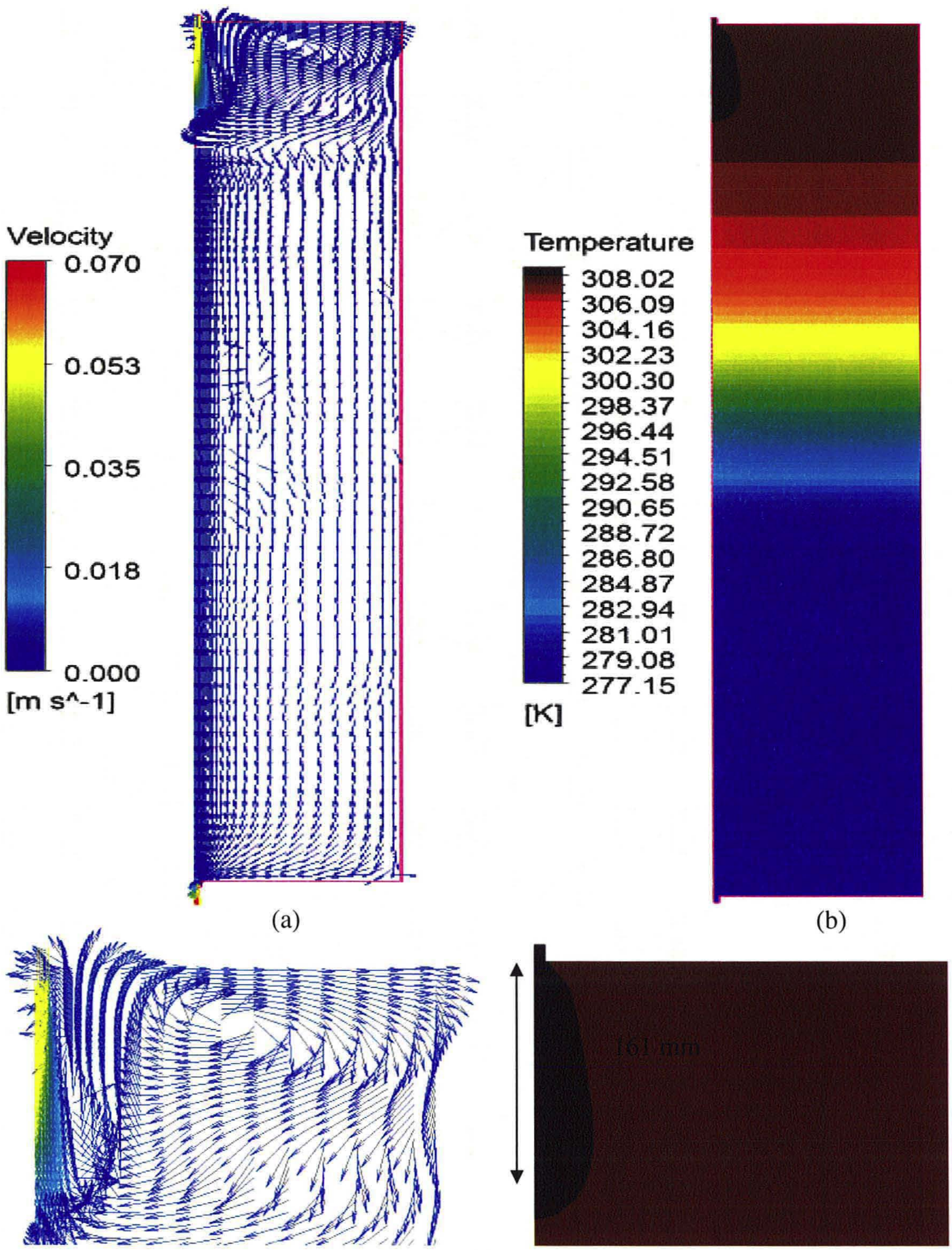

Figure 5.10: (a) Velocity Distribution, (b) Temperature Distribution after 12600 s Case II.

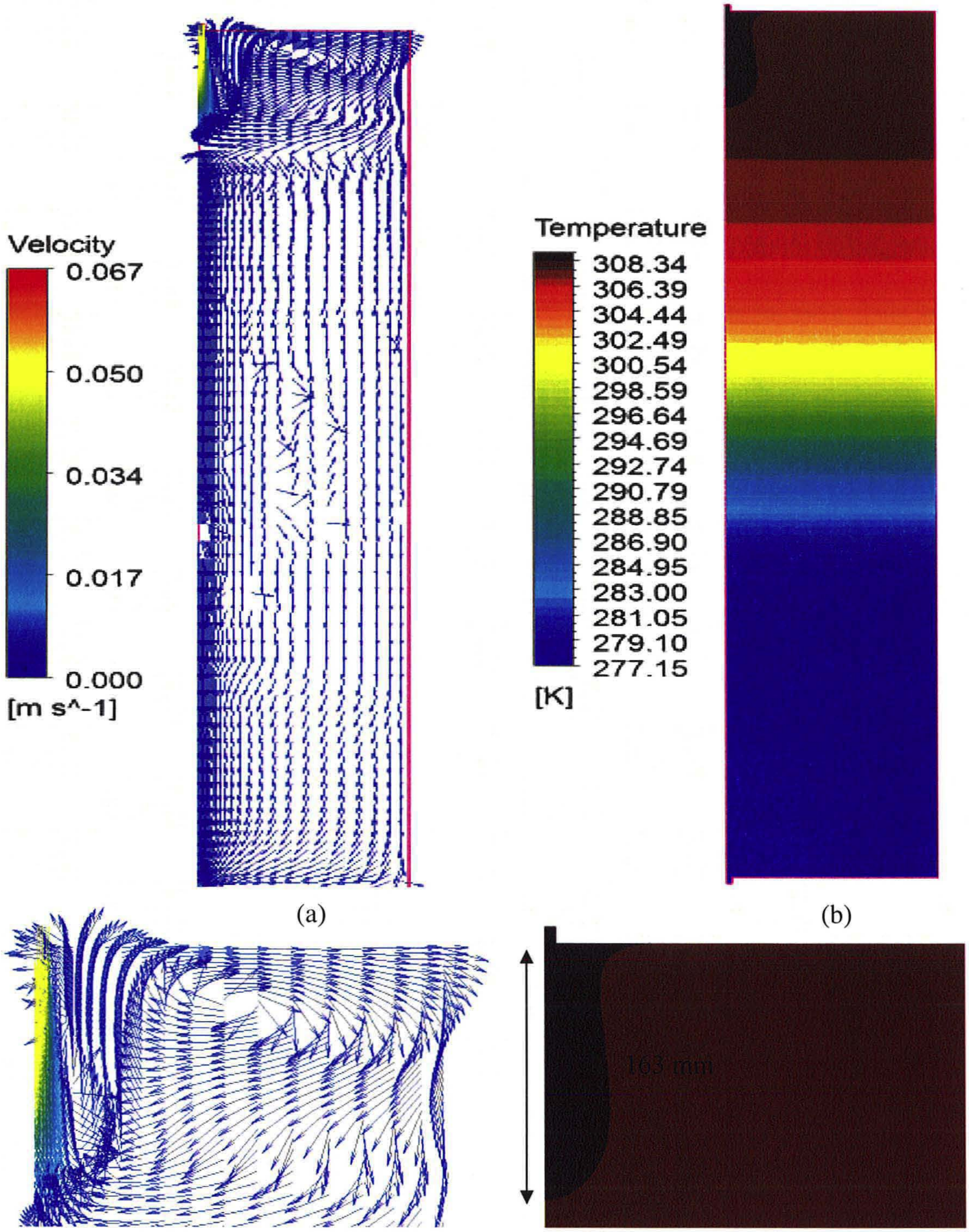

Figure 5.11: (a) Velocity Distribution, (b) Temperature Distribution after 14400 s Case II.

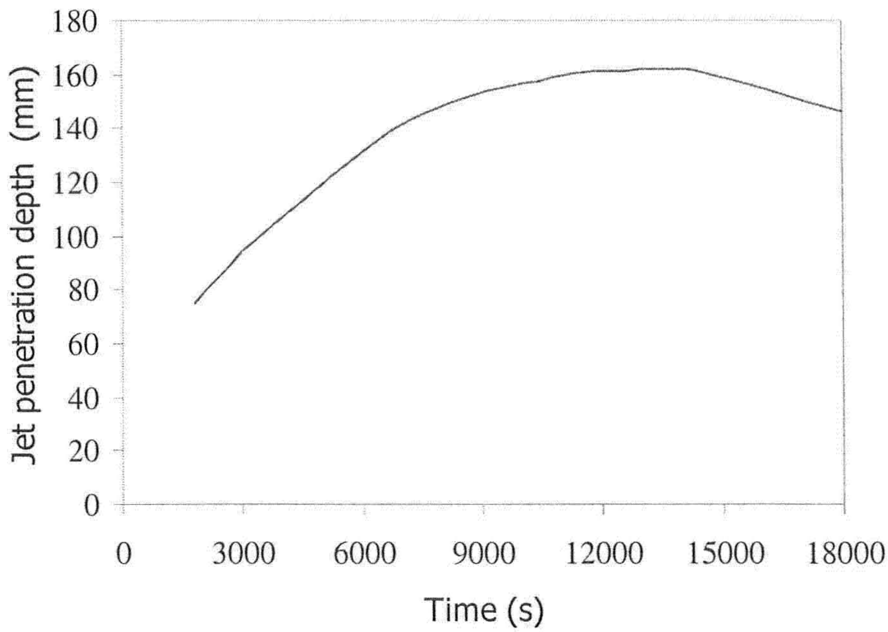

Figure 5.12: (a) Jet Penetration depth as a Function of Time Case II.

5.3 One Dimensional Modelling Concept

The modelling concept proposed in this work is explained in figure 5.13. The figure shows a schematic of temperature contours and velocity vectors, similar to those shown in previous section. Due to the nature of the flow associated with the negative buoyant plume the tank can be broadly divided into two regions. The "jet affected region" δ and the flat temperature profile region δ_4. The regions are shown in figure 5.13 (a).

The region δ has a radial temperature distribution. It can be further sub-divided in three regions as shown in figure 5.13 (b). The region δ_1 is the plume region. It receives the fluid from the inlet ($\dot{m}_{in}$) and it entrains fluid ($\dot{m}_{ent}$) from the region δ_3 adjacent to the plume. The fluid mixes in the region δ_1 and due to the buoyancy force, the fluid ($\dot{m}_p$) moves to the top of the tank to the region δ_2. The fluid from the region δ_2 moves to the

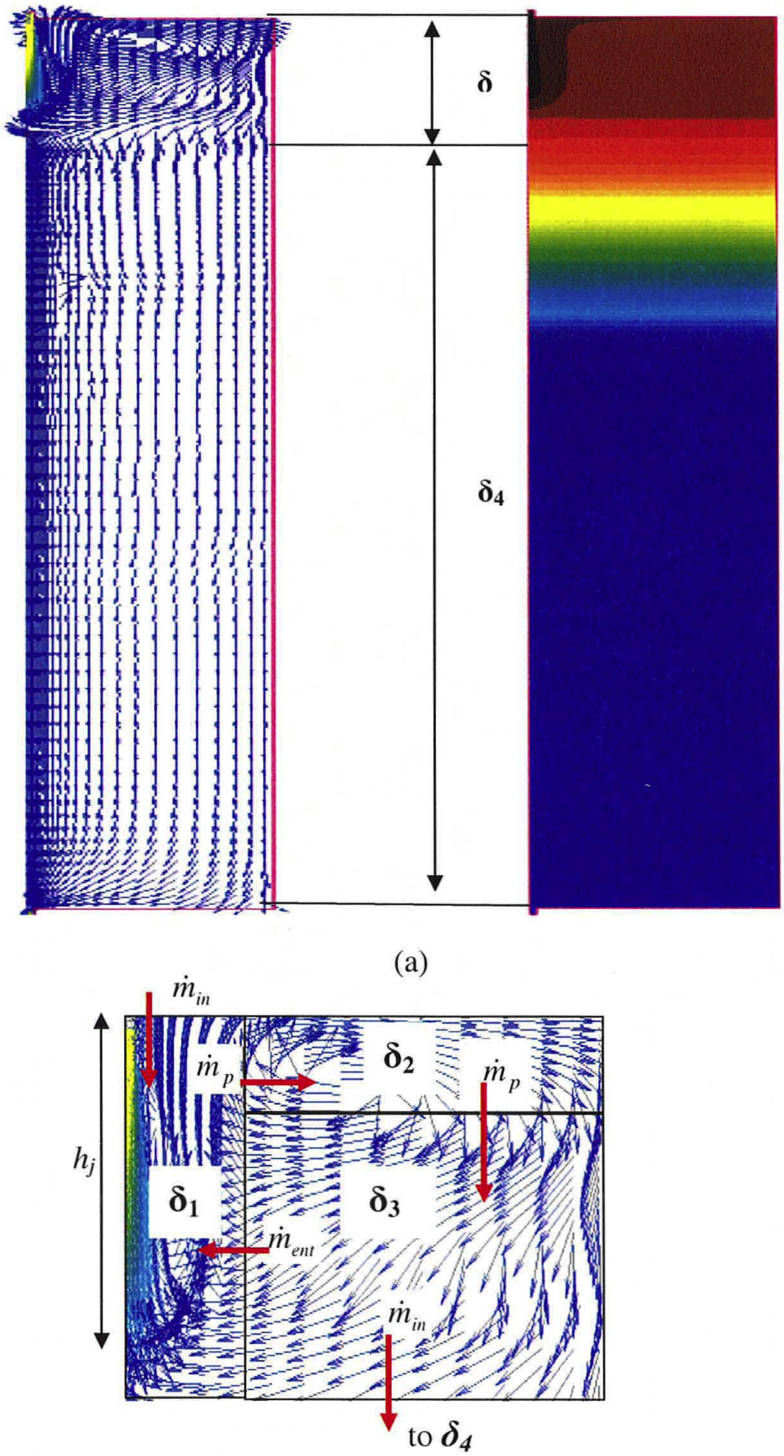

(a)

(b)

Figure 5.13 (a and b): Schematic of the Modelling Concept.

region δ_3 due to the flow in the axial direction. Fluid from the region δ_3, equal to the volume of the fluid coming from the inlet, flows to the region δ_4 and volume of fluid equal to the volume of the fluid entrained into the plume is discharged into the region δ_1, thus law of conservation of mass is maintained.

As per the description of the flow described above, the one dimensional model can be applied to the TST under the presumed approximation that the temperature in the plume (δ_1) region is spatially uniform whereas the temperature in other three regions (δ_2, δ_3 and δ_4) is presumed to vary axially (but is uniform radially). However, the following parameters should be known.

1. The extent of the regions δ_1 δ_2, and δ_3 and the width of the region δ_1. It was observed in the CFD results that the extent of the region δ_1 is nearly equal to h_j. Difference of approximately 18.0 mm to 22.0 mm was observed between h_j and the extent of the region δ_1 throughout the simulation time. The extent of the region δ_2 was observed to be approximately 20 mm for Case II and for Case I, it was equal to the length of the pipe (50.0 mm) which was submerged in the tank. Hence, if h_j is known, the extent of all the regions can be determined. In both cases studied, the width of the plume is observed to be negligible compared to the diameter of the tanks. It was observed to be approximately two to three times the inlet pipe diameter.

2. Flow Rates: The flow rate $\dot{m}_{in}$ coming through the inlet is a known quantity, Hence if the mass flow rate $\dot{m}_{ent}$ into the region δ_1 from the region δ_3 due to the mass entrainment is known, the mass flow rate out of the plume ($\dot{m}_p$) into the region δ_2 and the mass flow rate to the region δ_4 can be determined by the law of conservation of mass.

3. Eddy Diffusivity (α'): There is a wide spread in the literature on the effect of the diffusion term of the energy equation on the temperature distribution inside the tank. Lightstone *et al.* [64] ignored the diffusion term in the one dimensional modelling of the TST. Authors [35, 36, 37, 57, 58, 59] considered it for the one dimensional modelling of the TST but they did not consider the effect of the eddy diffusivity. Authors [13, 14, 41, 53, 54, 55] included the eddy diffusivity in their one dimensional analysis of the TST. However, in chapter 4 it was shown that the prediction of eddy viscosity in the jet affected region outside the plume affects the smearing of the thermal front. Therefore, in this work, the diffusion term was considered for the regions δ_2, δ_3 and δ_4 and the eddy diffusivity was determined for the regions δ_2, and δ_3. Hence, the challenge in this work is to determine the h_j and $\dot{m}_{ent}$ and α'. The next section focuses on determining these quantities.

5.4 Parametric Study on the behavior of the Negative Buoyant Plume

As presented in chapter 2, the dimensionless numbers which are generally associated with the characterization of negative buoyant plumes are the Reynolds number and the Richardson number. The definitions of these numbers are given in Eqs. (5.1) and (5.2), respectively. This section will examine the effect of the Reynolds and Richardson numbers on the behavior of the negative buoyant plume. The Case II geometry was used for the parametric study. The inlet velocity was varied to achieve a Reynolds number in the range of 600 to 1200. The inlet temperature was varied in the range of 10^0 C to 40^0 C. The initial TST temperature was kept constant at 5^0 C. The inlet pipe diameter was varied from approximately 15.0 mm to 30 mm. The SST turbulence model without the buoyancy term was used to capture the turbulence. All other simulation details were kept similar to the previous simulations in Case II. The simulations were carried out by changing the parameters as mentioned above. The flow parameters (inlet velocity and inlet temperature) were chosen to cover a wide range of inlet conditions which are practically achieved in NCHE SDHW systems. The geometric parameter (inlet pipe diameter) was chosen to cover the practical range of pipe diameters in SDHW TST systems.

$$Re = \rho_{in}\overline{u}_{in}d / \mu \tag{5.1}$$

$$Ri = \Delta\rho g d / \rho_r \overline{u}_{in}^{\,2} \tag{5.2}$$

As mentioned before, the penetration depth of the jet is affected by the thermal condition of the fluid in the vicinity of the jet. Therefore in order to allow the developed jet to interact with surrounding fluid at uniform temperature, initial simulations for every parametric change were carried out for ten minutes and the resulting velocity distributions for each case were used as initial conditions for the final simulations in which the temperature distribution inside the TST was again set back to initial temperature of 5^0 C. The procedure eliminates the effects arising from the initial flow development and transient change in the density of the fluid in the circulation region. As a result of this procedure, the exact depth of penetration of the jet based on the temperature difference between the fluid at the inlet and the initial condition of the fluid in the TST can be determined at the time interval when the velocity reverses.

Three different quantities were chosen for the characterization of the negative buoyant plume; namely, the jet penetration depth (h_j), which was defined previously, the non-dimension fluid entrainment ($\dot{m}$), defined as the ratio of $\dot{m}_p$ and $\dot{m}_{in}$ and the eddy diffusivity (α') in the TST region outside the plume but within the circulation region (δ_2 and δ_3). Figures 5.14 (a) and (b) show the h_j–Ri relationship. It is clear from figure 5.15 (a) that the effect of the Reynolds number on the jet penetration depth is negligible. From figure 5.14 (b), it can be concluded that the jet penetration is a function of the inlet pipe diameter. The penetration of the jet increases with an increase in the inlet pipe diameter within the range considered in this study. A regime appears to exist between Richardson numbers of 0.1 to 0.2 above which the buoyancy force dominates over inertia of the incoming jet. While below this range the inertia force of the jet dominates the flow causing deeper penetration and more mixing in the TST.

Figures 5.15 shows the $\dot{m}$-Ri relationship, and figure 5.16 shows the α'-Ri relationship. The y axis in figure 5.16 (α'-Ri relationship) has been non-dimensionalized by thermal diffusivity (α). The trend in both the relationships was similar to the h_j-Ri relationship. Figure 5.15 suggests that the inlet Reynolds number has a negligible effect on the mass flow entrained inside the plume; while figure 5.16 suggests that the eddy diffusivity is a function of the inlet Reynolds number.

The general trend of all the three quantities as functions of the Richardson number was determined mathematically of the form given in Eqs. (5.3) to (5.5). The $\Delta\rho$ term of the Richardson number for the relationship with h_j and α' was defined based on the density difference between the fluid at the inlet and the density of the fluid in the region δ

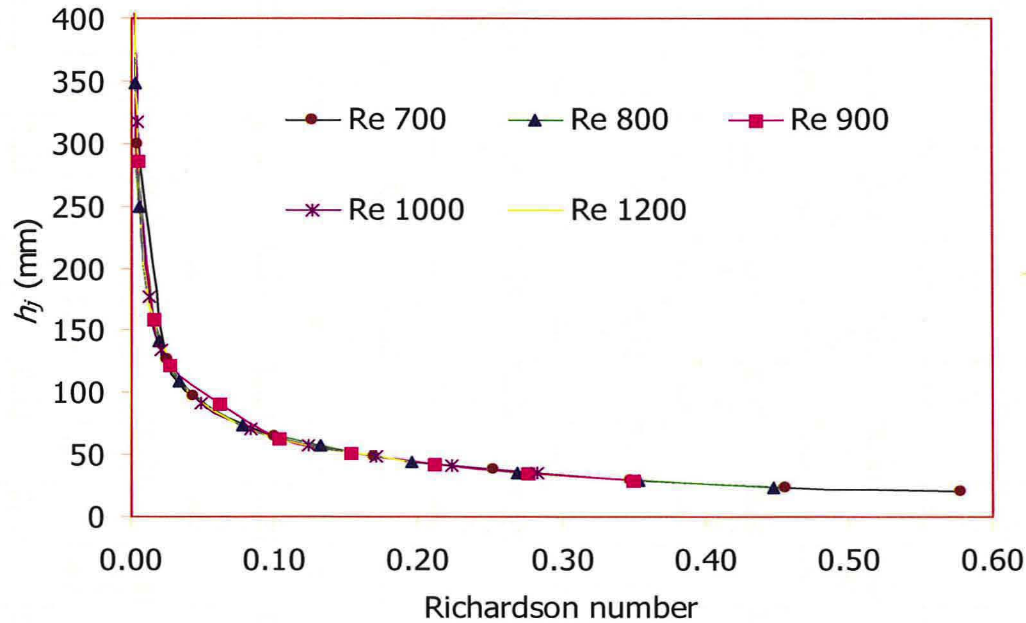

(a)

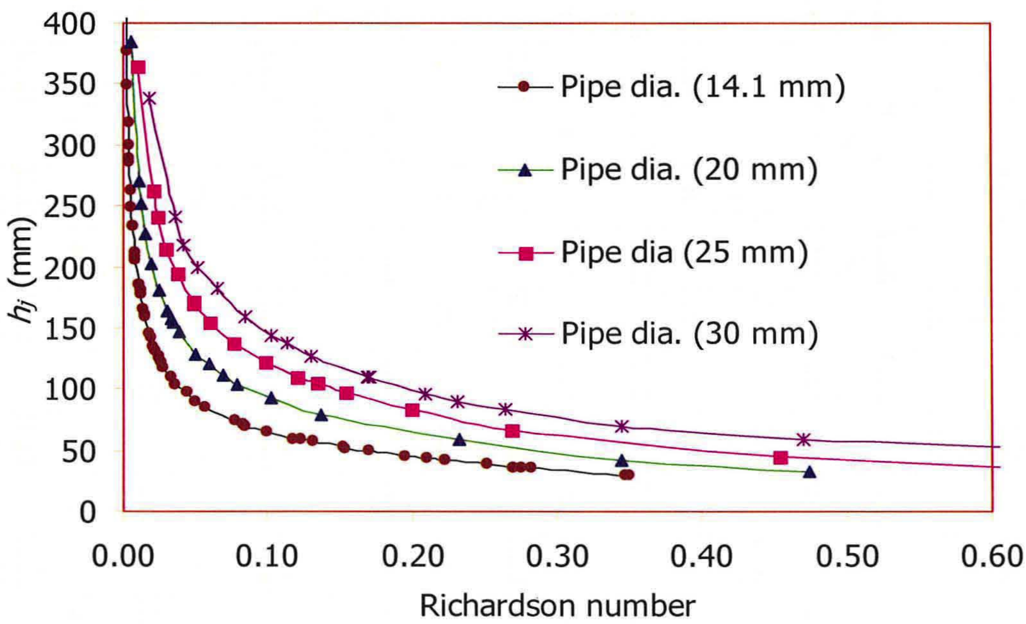

(b)

Figure 5.14: h_j–Ri Relationship (a) at different Re, (b) at different Pipe Dia.

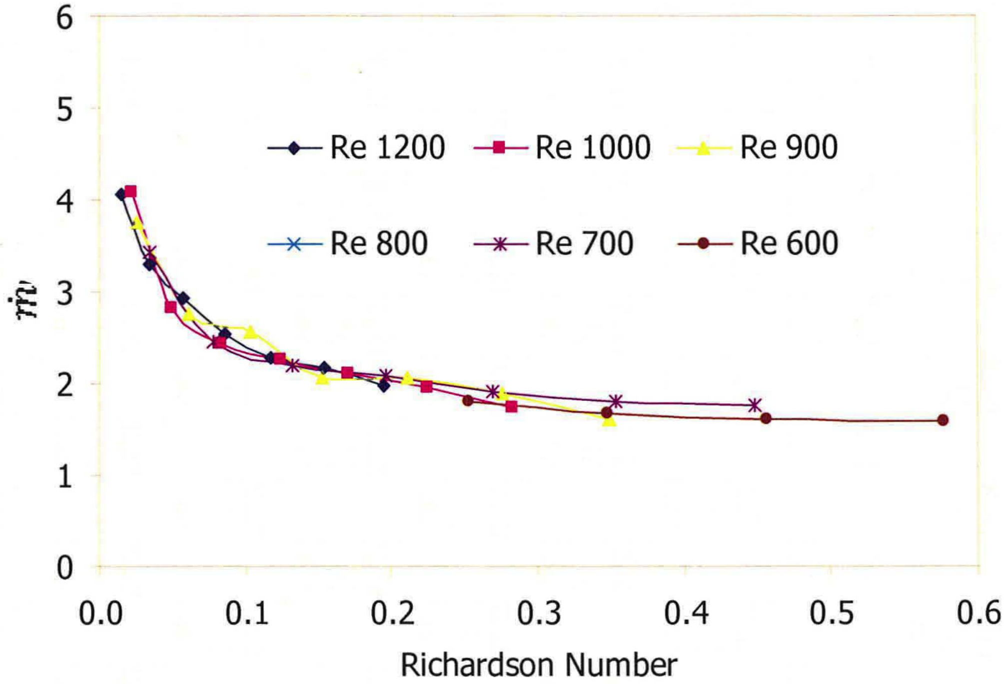

Figure 5.15: $\dot{m}$ –Ri Relationship.

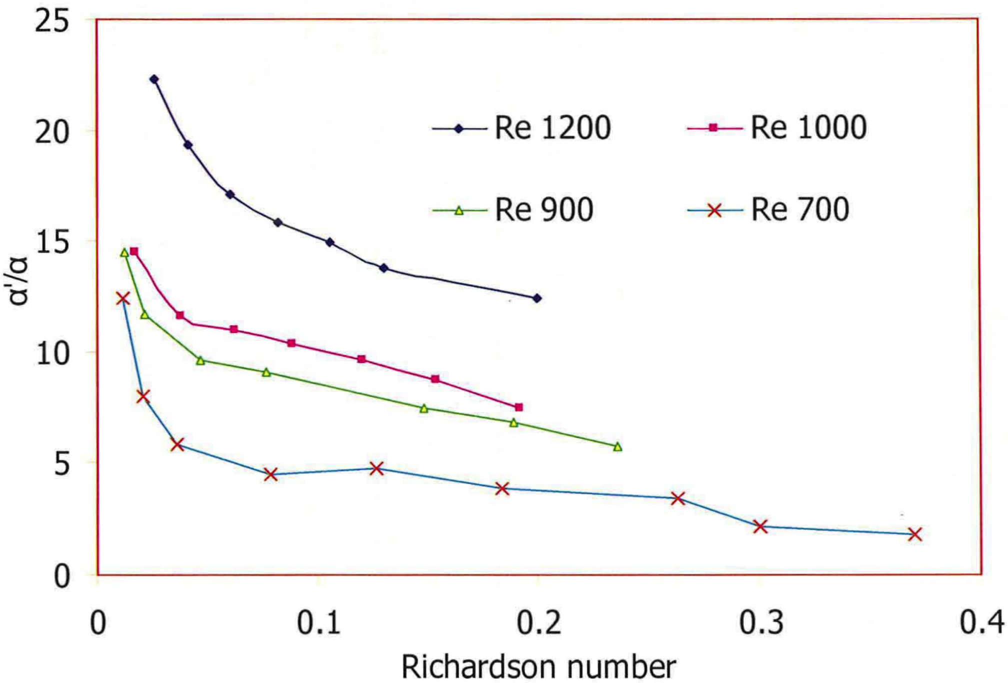

Figure 5.16: α' –Ri Relationship.

while for $\dot{m}$ it was defined based on the density difference between the fluid at the inlet and the region δ_l. The term a and b in the equations are constants. The functional relationships of a determined in this work for h_j, $\dot{m}$ and α' are given in Eqs. (5.6), (5.8) and (5.10), respectively and the functional relationships of b determined in this work are given in Eqs. (5.7), (5.9) and (5.11), respectively.

$$h_j = a_{h_j} Ri^{-b_{h_j}} \tag{5.3}$$

$$\dot{m} = a_m Ri^{-b_{\dot{m}}} \tag{5.4}$$

$$\alpha' = a_{\alpha'} Ri^{-b_{\alpha'}} \tag{5.5}$$

$$a_{h_j} = -0.0257d^2 + 2.128d - 3.4657 \tag{5.6}$$

$$b_{h_j} = 0.525 \tag{5.7}$$

$$a_m = 1.062 \tag{5.8}$$

$$\mathrm{b}_m = 0.278 \tag{5.9}$$

$$a_{\alpha'} = 1.6 \times 10^{-9} (Re) - 8.42 \times 10^{-7} \tag{5.10}$$

$$\mathrm{b}_{\alpha'} = 0.2905 \tag{5.11}$$

As discussed in Chapter 2, various authors have proposed different regimes based on the Richardson number to explain whether the incoming jet will mix with the fluid in the TST or will flow directly to the top of the TST without mixing. However, in this study we conclude that such regime cannot be defined solely on the Richardson number as it is clear from figure 5.14 (b) that for the same Richardson number the depth of penetration is different for different inlet pipe diameters.

5.5 Governing Equations

The models proposed in the previous section for the characterization of the negative buoyant plume can be incorporated into the one dimensional energy equation to solve for the temperature distribution inside the tank. The energy equation in the different regions of a well insulated TST can be simplified as given below. Note that in the equations below the extent of the regions are represented by the regions itself. For example, δ_1 represents its vertical extent in the tank.

For δ_1, the energy equation can be written as:

$$\rho A_{\delta_1} \delta_1 \frac{dT_{\delta_1}}{dt} = \dot{m}_{in} T_{in} - (\dot{m}_{in} + \dot{m}_{ent}) T_{\delta_1} + \dot{m}_{ent} T_{\delta_3} \tag{5.12}$$

Solving Eq. (5.12) and applying initial condition $T_{\delta_1} = T_{ini}$ (initial) at $t = 0$, gives:

$$T_{\delta_1} = \frac{\dot{m}_{in} T_{in} + \dot{m}_{ent} T_{\delta_3} + ((\dot{m}_{in} + \dot{m}_{ent}) T_{ini} - \dot{m}_{in} T_{in} - \dot{m}_{ent} T_{\delta_3}) e^{-\left(\frac{(\dot{m}_{in} + \dot{m}_{ent})}{\rho A_{\delta_1} \delta_1}\right) t}}{\dot{m}_{in} + \dot{m}_{ent}} \tag{5.13}$$

The flow rate $\dot{m}_p$ is calculated from Eqs. (5.4), (5.8) and (5.9). It was discussed in the previous section that the extent of the region δ_1 varied approximately from 18.0 mm to 22.0 mm more than the penetration depth of the jet. For simplification, a constant value of 20 mm is considered. Hence, δ_1 is 20.0 mm more than h_j. The extent of h_j is calculated from Eqs. (5.3), (5.6) and (5.7). It was also discussed in section 5.3 that the width of the plume was observed two to three times the inlet pipe diameter. The pipe diameters were 25.4 mm and 14.2 mm for Case I and Case II, respectively. Therefore a constant value of

60 mm was assumed for both cases. The cross section area $A_{\delta 1}$ was calculated based on this constant value for both the cases.

For δ_2 an assumption is made that fluid from the plume region (δ_1) enters the region δ_2 from the top of the region, i.e. $\dot{m}_p$ is the flow rate across any cross section area in the region δ_2. The energy equation for δ_2 can be written as:

$$\rho A_{\delta_2} \frac{\partial T_{\delta_2}}{\partial t} = -\dot{m}_{\delta_2} \frac{\partial T_{\delta_2}}{\partial x} + \rho A_{\delta_2} (\alpha + \alpha') \frac{\partial^2 T_{\delta_2}}{\partial x^2} \tag{5.14}$$

where, $\dot{m}_{\delta_2} = \dot{m}_p$. The extent of the region δ_2 is considered 20 mm as observed in the CFD study of Case II. For Case II, it is equal to the length of the pipe submerged in the tank (i.e. 50 mm).

For δ_3, the energy equation can be written as:

$$\rho A_{\delta_3} \frac{\partial T_{\delta_3}}{\partial t} = -\frac{\partial \dot{m}_{\delta_3} T_{\delta_3}}{\partial x} + T_{\delta_3} \frac{\partial \dot{m}_{\delta_3}}{\partial x} + \rho A_{\delta_3} (\alpha + \alpha') \frac{\partial^2 T_{\delta_3}}{\partial x^2} \tag{5.15}$$

for δ_4, the energy equation can be written as:

$$\rho A_{\delta_4} \frac{\partial T_{\delta_4}}{\partial t} = -\dot{m}_{\delta_4} \frac{\partial T_{\delta_4}}{\partial x} + \rho A_{\delta_4} (\alpha) \frac{\partial^2 T_{\delta_4}}{\partial x^2} \tag{5.16}$$

The thermal diffusivity in the regions δ_2, δ_3, and δ_4 is considered constant. The eddy diffusivity for the regions δ_2 and δ_3 is calculated from Eqs. (5.5), (5.10) and (5.11). The first term on the R.H.S of Eq. (5.15) represents the advection into the control volume, while second term represents the advection out of the control volume into the plume region. The quantity $\frac{d\dot{m}_{\delta_3}}{dx}$ is considered constant for simplification. With this simplification, mass flow rate at any cross section in the region δ_3 can be determined by Eq. (5.17).

$$\dot{m}_{\delta_3}\Big|_x = \dot{m}_p - \frac{d\dot{m}_{\delta_3}}{dx}(x-\delta_2) \tag{5.17}$$

Where,

$$\frac{d\dot{m}_{\delta_3}}{dx} = \frac{\dot{m}_{ent}}{\delta_3} \tag{5.18}$$

Numerical Solution of the Governing Equations

For uniform size control volumes in the region δ_3, Eq. (5.12) can be discretized as:

$$T_{\delta_1}\Big|^n = \Bigg[(\dot{m}_{in}T_{in})\Big|^n + \underbrace{(\dot{m}_{\delta_3}\Big|_x^n - \dot{m}_{\delta_3}\Big|_{x+\Delta x}^n)\sum_{x=\delta_2}^{x=\delta_3} T_{\delta_3}\Big|^n}$$
$$+ \left((\dot{m}_{in}+\dot{m}_{ent})\Big|^n T_{\delta_1}\Big|^{n-1} - (\dot{m}_{in}T_{in})\Big|^n - \underbrace{(\dot{m}_{\delta_3}\Big|_x^n - \dot{m}_{\delta_3}\Big|_{x+\Delta x}^n)\sum_{x=\delta_2}^{x=\delta_3} T_{\delta_3}\Big|^n}\right)$$
$$e^{-\left(\frac{(\dot{m}_{in}+\dot{m}_{ent})|^n}{\rho A_{\delta_1}\delta_1}\right)\Delta t}\Bigg] \div (\dot{m}_{in}+\dot{m}_{ent})\Big|^n \tag{5.19}$$

Note that the marked terms in the Eq. (5.19) account for the non uniform temperature distribution in the region $\delta 3$ and are equal to $\dot{m}_{ent}T_{\delta_3}$ in Eq. (5.13).

The convective and the diffusion terms of the energy equations in the regions δ_2, δ_3, and δ_4 (i.e. Eqs. (5.14), (5.15) and (5.16)) are treated with the upwind and the central difference schemes, respectively. The time marching of each term is kept implicit. The use of a fully implicit scheme overcomes the limitation of selecting a small time step, which otherwise causes numerical instabilities in the explicit scheme.

The generalized form of discretized energy equation in the three regions is given in Eq. (5.20) with $\alpha' = 0$ for the region δ_4.

$$\left[\frac{\rho A\,\Delta x^2}{\Delta t} + \dot{m}\Big|^n_{x+\Delta x}\Delta x + 2(\alpha+\alpha')\rho A\right]T\Big|^n_{x+\Delta x} - \left[\dot{m}\Big|^n_{x+\Delta x}\Delta x + (\alpha+\alpha')\rho A\right]T\Big|^n_x - \left[(\alpha+\alpha')\rho A\right]T\Big|^n_{x+2\Delta x} = \left[\frac{\rho A\,\Delta x^2}{\Delta t}\right]T\Big|^{n-1}_{x+\Delta x} \tag{5.20}$$

Figure 5.17 shows the schematic of the node distribution and the pattern of control volume interaction in the domain.

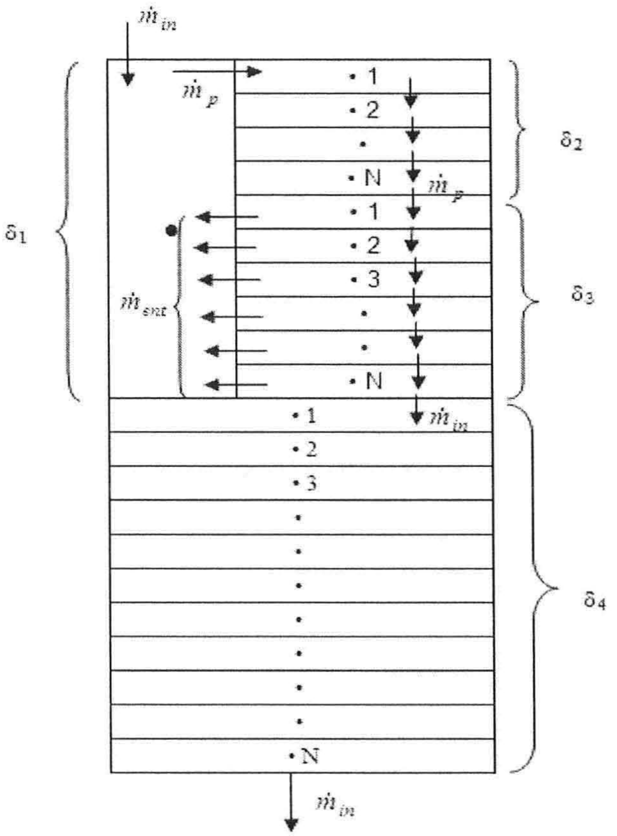

Figure 5.17: Schematic of the Node Distribution Inside the One Dimensional Tank

Boundary Conditions

Initial temperature distribution in the tank (at time step zero) is required. For Case I, it was set to 21^0C and for Case II, it was set to 5^0C. The inlet boundary conditions: the mass flow rate and the temperature at the inlet are required at each time step. For Case I, inlet temperature and flow rate was set to 40^0C and 0.1 kg/s. For Case II, inlet temperature and flow rate were provided in the same manner as it was provided in the two dimensional simulations using ANSYS CFX - 11 (Eqs. (4.7) and (4.12)). $\frac{\partial T}{\partial x} = 0$ was applied at outlet node.

Solution Method

Prior to solving for the temperature, the extent of the various regions must be determined, in particular the region δ. At first time step, the extent of the region δ can be determined based on the uniform density in the tank and the relationship h_j-Ri. However, for the further time steps the relationship cannot be used directly. Consider the flow visualizations which have been presented in figures 5.1 to 5.4 for Case I (fixed inlet condition) and figures 5.5 to 5.12 for Case II (variable inlet condition). It was observed for both the cases that the depth of penetration of the jet increased with time, depending upon the temperature of the fluid in the vicinity of the jet. As the temperature difference between the jet fluid and the fluid in the vicinity of the jet reduces, the buoyancy force exerted on the jet is reduced, resulting in deeper penetration. However in Case II (variable inlet condition), the penetration height also reduces after long times as a result of the reduced flow into the tank (and hence reduced inlet jet momentum). Also, recall that the relationship h_j–Ri was based on the density difference between the fluid at the inlet and in the region δ. Therefore in order to determine the extent of the region δ from the second time step, an iterative procedure is applied to determine the extent of the region in the TST wherein the density of the fluid can predict the extent of that region using the h_j–Ri relationship. The iterative procedure is explained in the algorithm given below.

If the temperature ($T_{\delta 1}$) entering the region δ_2 is known, the discrete equations for the temperature in the regions δ_2, δ_3 and δ_4 form a tridiagonal matrix. Hence, in each time step the temperature of the fluid coming out of the region δ_1 which is also the temperature of the fluid entering the region δ_2 is estimated to solve the tridiagonal matrix for obtaining the temperature distribution in the regions δ_2, δ_3 and δ_4. The convergence was based on the temperature of the fluid which came out of the region δ_1 and entered the region δ_2.

The program for the modeling is written in Compaq Visual FORTRAN V6.6 and is presented in the appendix B. The algorithm for the solution procedure is given below.

1. Initial Condition in the tank is provided.
2. Evaluate $\dot{m}_{in}$ and T_{in} based on the initial condition or on the value from the previous time step.
3. Evaluate δ using the initial density of the fluid in the entire tank for the first time step and for further time steps, if δ is less than or equal to the previous time step, go to step 4. If δ is more than the value in the previous time step then the value of δ based on the average density of the fluid in the region δ from the previous time step is used to set the maximum limit of the δ in the

current time step, while value of δ in previous time step is set as the minimum limit. The procedure iterates from the minimum limit towards the maximum limit until δ is equal to or less than the extent of the region in the tank whose average density is used to calculate δ. Once the criterion is met go to step 4.

4. Evaluate $\dot{m}_p$ and α'
5. Evaluate $\dot{m}_{\delta_3}$ based on $\dot{m}_p$ and $\dot{m}_{in}$.
6. Temperature distribution in the tank is evaluated by marching down the tank, using the discretized equation for respective regions.
7. Average density in the whole tank and in the 'δ' region is calculated.
8. Back to 2.

5.6 Model Validation

The relationships for the characterization of the negative buoyant plume were developed for the low inlet Reynolds number, specifically for the NCHE SDHW systems, where the flow rates developed in the system are low. However, in section 5.2, it was shown that the nature of the negative buoyant plume was similar for the high and the low inlet Reynolds number. Hence, in order to check the range of the validity of the proposed relationships, the predictions of the one dimensional modelling were assessed by comparing the results from the one dimensional modelling to the predictions from the detailed CFD simulations for Case I and Case II. In order to have a comparative study, the existing one dimensional plug flow model was also used. The plug flow model does not consider the mixing caused by the incoming jet and therefore it does not have the region δ. This model presumes that incoming hot is transferred to the top of the tank without mixing. Mixing occurs only as the result of molecular diffusion. The discretized energy equation of the plug flow model is similar to Eq. (5.20) with $\alpha' = 0$ for the entire domain. After assessing the grid independence and time independence (grid independence and time step independence results are presented in appendix C), the domains were divided into uniform grid of size 1.0 mm except in the region δ_l, which was considered as one single volume and time step of one second was set for both the cases. Note that the plug flow model did not have the region δ.

Figures 5.18 to 5.23 show comparison of the results among the one dimensional model developed in this work, the plug flow model and the two dimensional results from ANSYS CFX – 11 at different times. The simulation *2S5* (two dimensional modeling results) was used for the comparison. From the results it is evident that the predictions of the one dimensional modelling from this work have close agreement with the two dimensional modelling. In the top portion of the tank above the thermocline the agreement was within 0.7^0C. However, the one dimensional model predicts a thinner thermocline in comparison to the detailed CFD results. A maximum deviation of 3^0C was observed in the temperature prediction of the thermocline. The rise in the temperature in the region above the thermocline is approximately 11^0C from 23^0C at 15 minutes to 35^0C at 150 minutes; however the rise in temperature for the same region by the plug flow model is approximately 1^0C from 34^0C at 15 minutes to 35^0C at 150 minutes. It is seen that the plug flow model over predicts the temperature at the top portion of the tank for most of the period. It is evident from the results that the model presented in the current

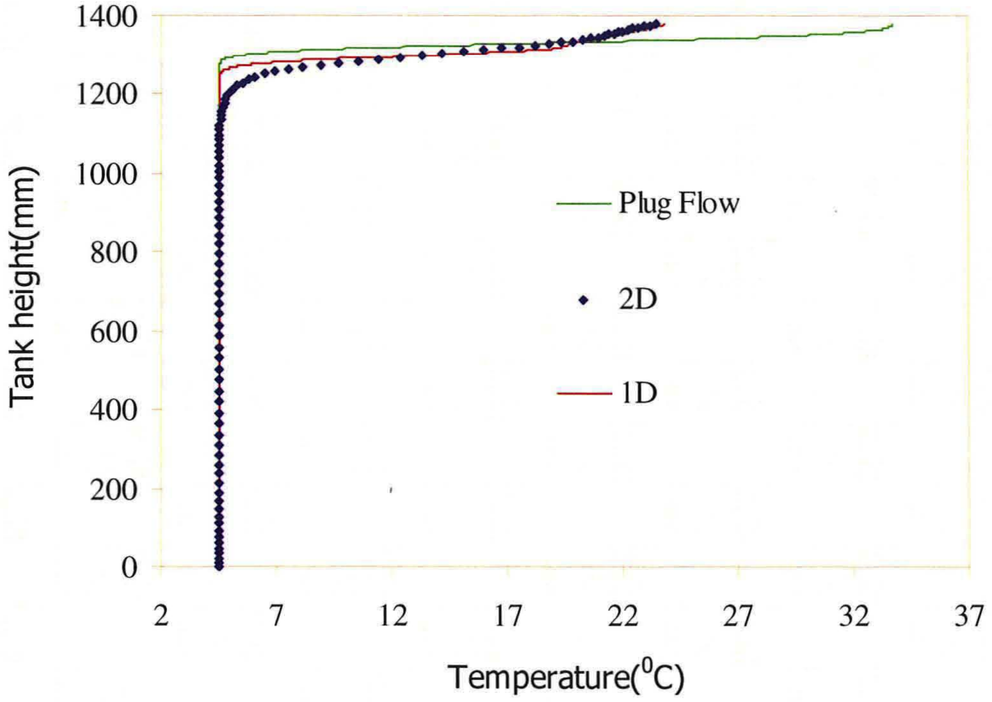

Figure 5.18: Temperature Distribution in the Tank at 16 Minutes- Case II.

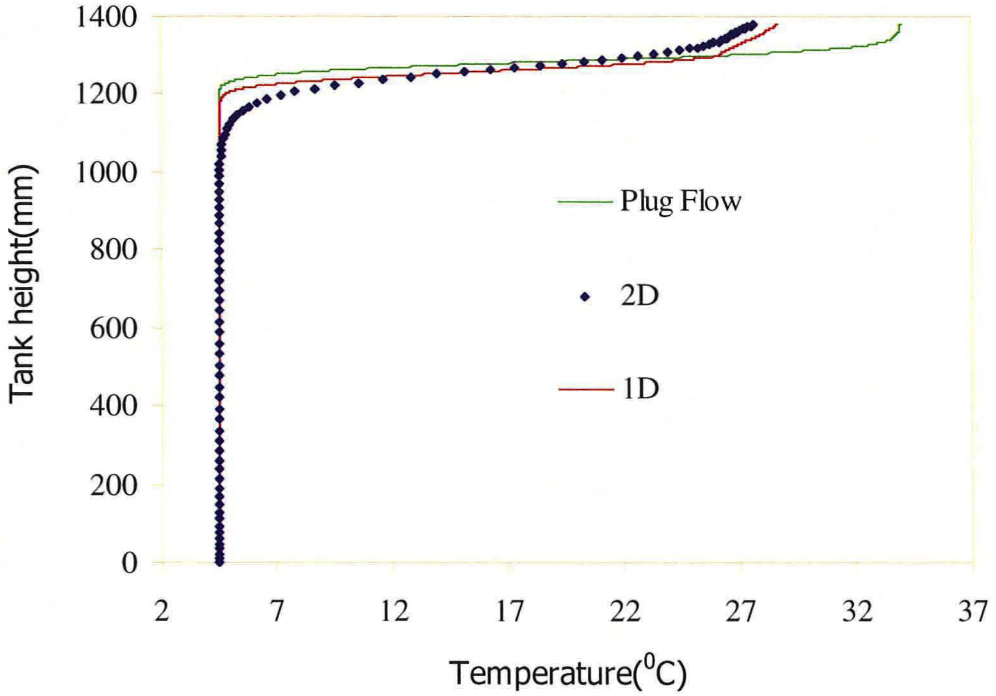

Figure 5.19: Temperature Distribution in the Tank at 30 Minutes- Case II.

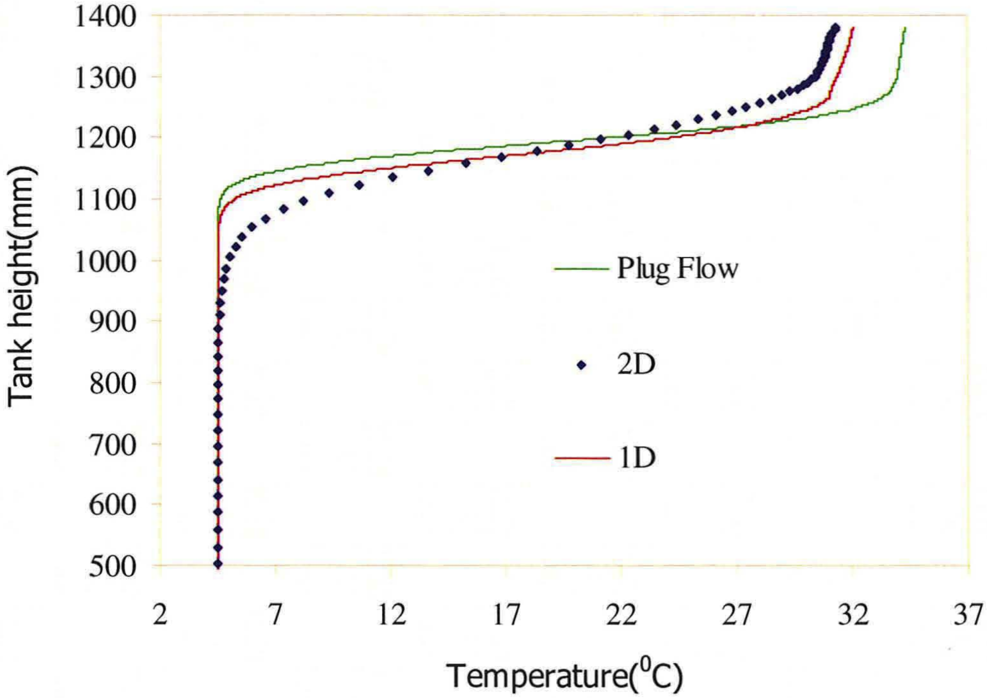

Figure 5.20: Temperature Distribution in the Tank at 60 Minutes- Case II.

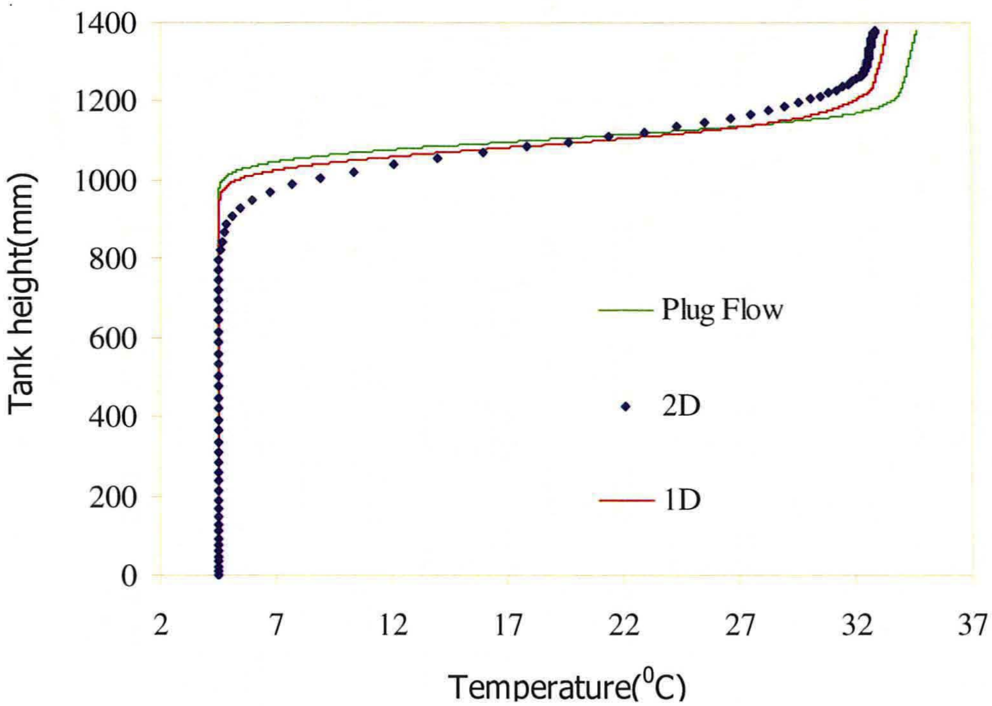

Figure 5.21: Temperature Distribution in the Tank at 90 Minutes- Case II.

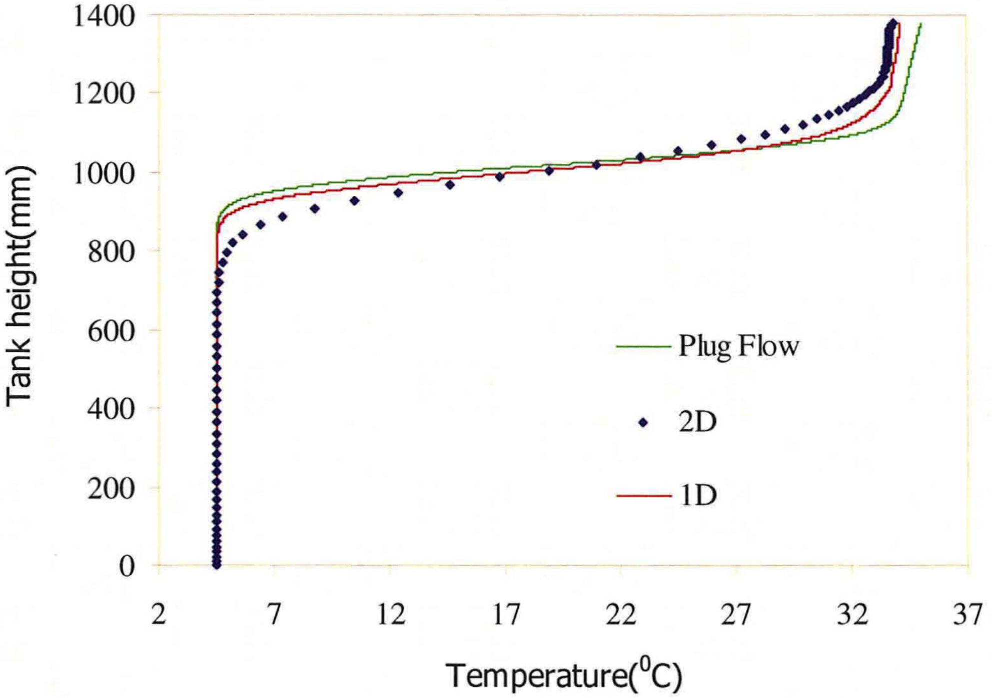

Figure 5.22: Temperature Distribution in the Tank at 120 Minutes- Case II.

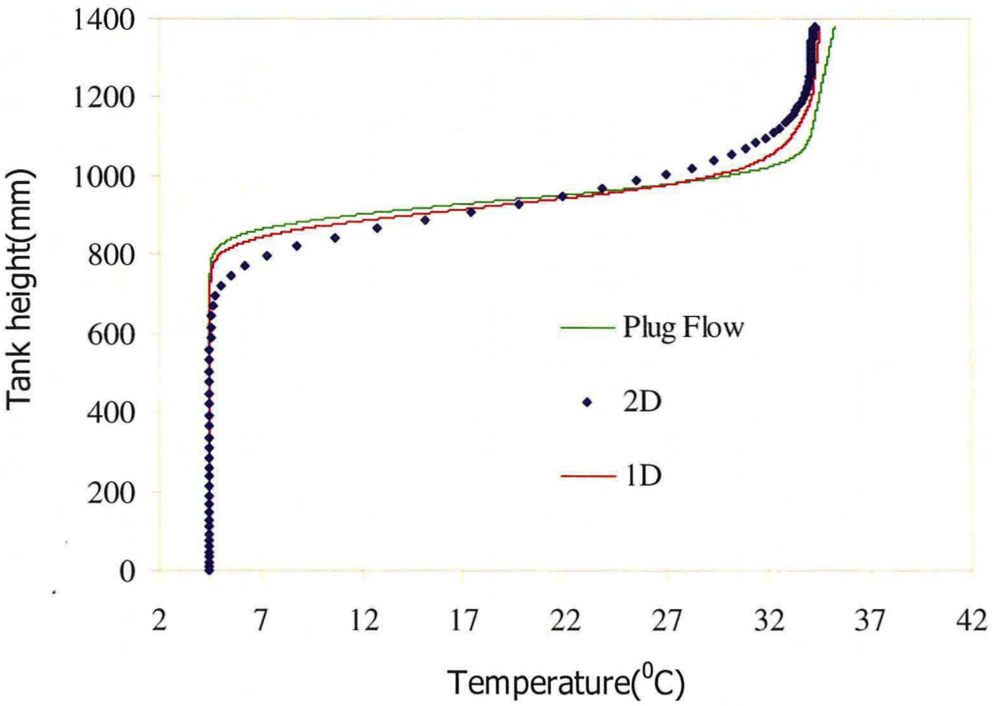

Figure 5.23: Temperature Distribution in the Tank at 150 Minutes- Case II.

study shows better prediction of the temperature distribution inside the tank. However, as the temperature of the fluid in the top portion of the tank slowly reaches the temperature of the fluid at the inlet, the change in temperature slowly reduces in that region and there is apparent reduction in the difference among the three results.

Figures 5.24 to 5.31 show the comparison of the temperature prediction inside the tank for Case I at different times. The simulation *1S3* (two dimensional results) was used for the comparison. In general, the prediction of the one dimensional modelling proposed in this work are smeared in the regions δ_2 and δ_3 due to the consideration of the average α' in the region δ_2 and δ_3. The shape of the thermal front is distorted. However the temperature predictions with respect to the deviation from the two dimensional results are less. The agreements in the predictions were within 1^0C. In comparison with the plug flow model, it is evident that the results from this work are better. From the results, it can be concluded that the model presented in this work is capable of predicting the mixing caused by the buoyant plume for the high Reynolds number cases reasonably well.

Considering the deviation in the temperature prediction and the computational time, the one dimensional modelling of such systems are supported. The difference in computational time is of the order of 100.

5.7 Conclusion

This chapter presented the relationships which were developed to characterize the behavior of the negative buoyant plume in terms of the jet penetration depth, the mass entrained inside the plume and the eddy diffusivity in the jet affected region as a function of the Richardson number. The relationships were developed based on the CFD results. It was also confirmed that for such a flow structure, the depth of jet penetration is independent of the Reynolds number at the inlet. A one dimensional system model to predict the temperature distribution inside the TST of the SDHW tank system was also developed. Results were compared to the CFD results presented earlier. It was found that the new model predicts the CFD results fairly well. The advantage of the new model is the significant reduction in computational effort that is required for the temperature prediction inside the storage tank. Results were also compared to those from the simple plug flow model and were shown to provide improved predictions of the temperature profile.

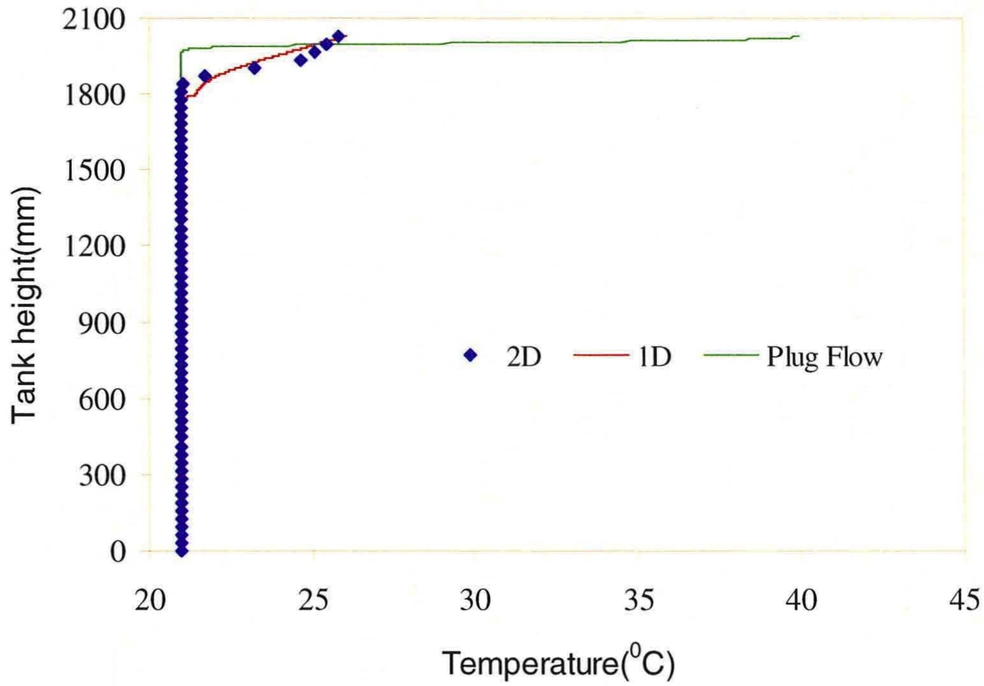

Figure 5.24: Temperature Distribution in the Tank at 5 Minutes- Case I.

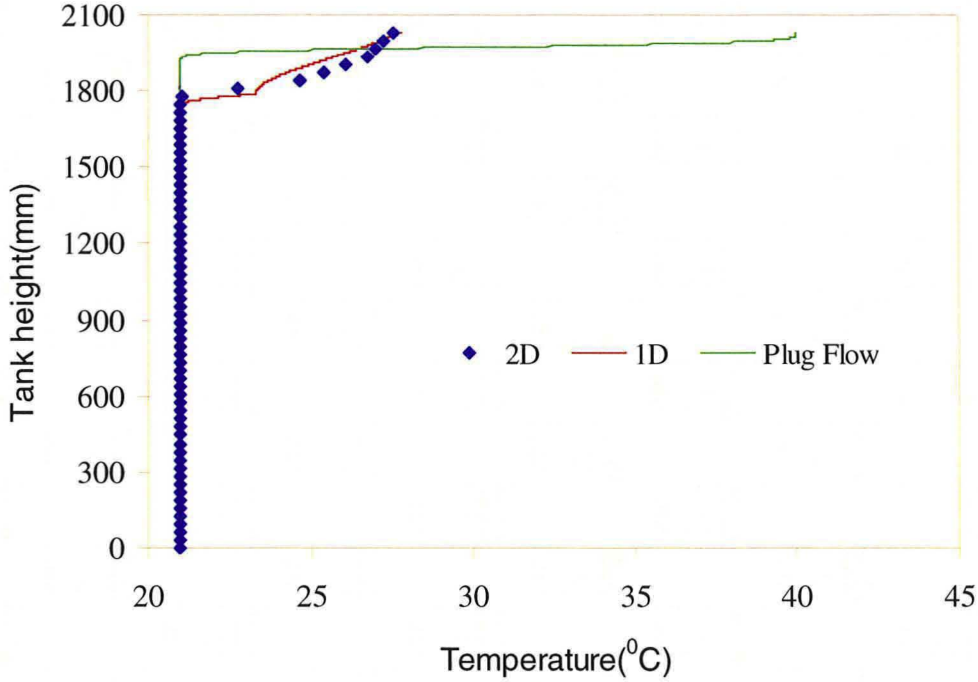

Figure 5.25: Temperature Distribution in the Tank at 10 Minutes- Case I.

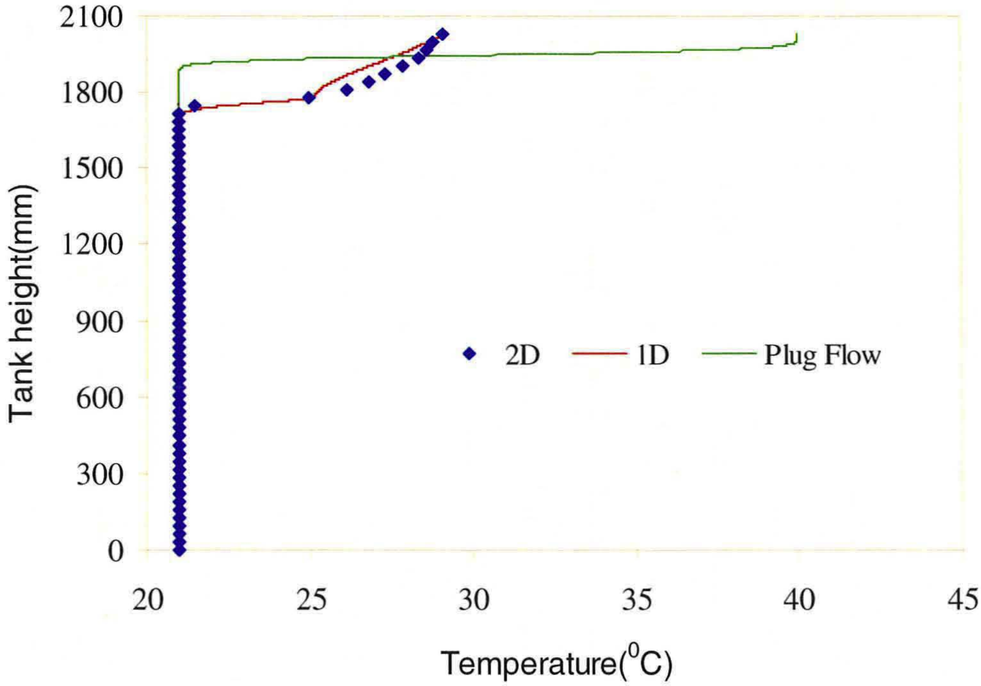

Figure 5.26: Temperature Distribution in the Tank at 15 Minutes- Case I.

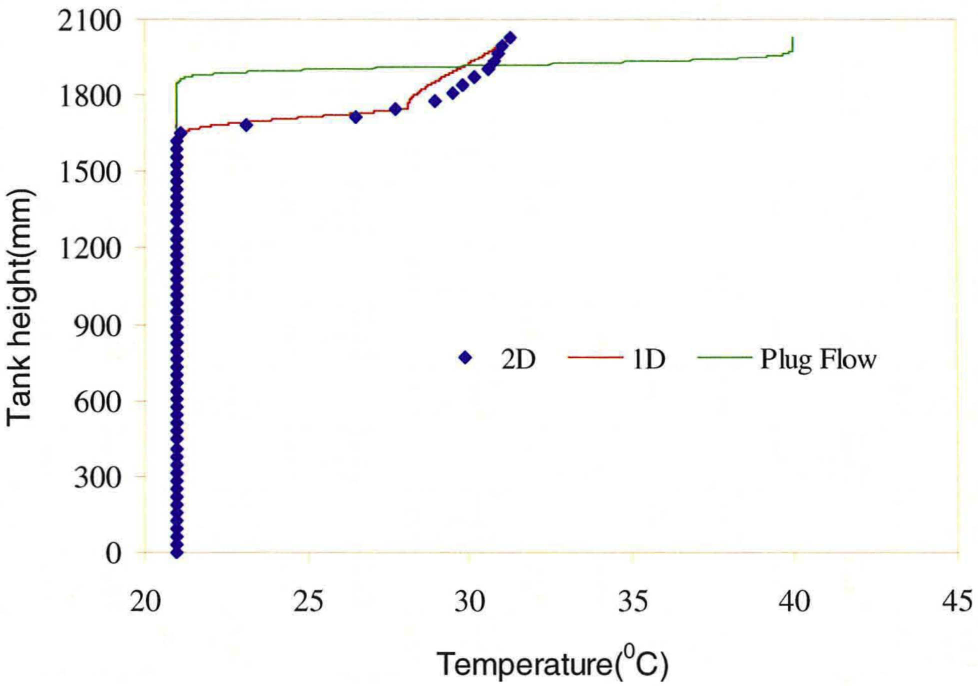

Figure 5.27: Temperature Distribution in the Tank at 25 Minutes- Case I.

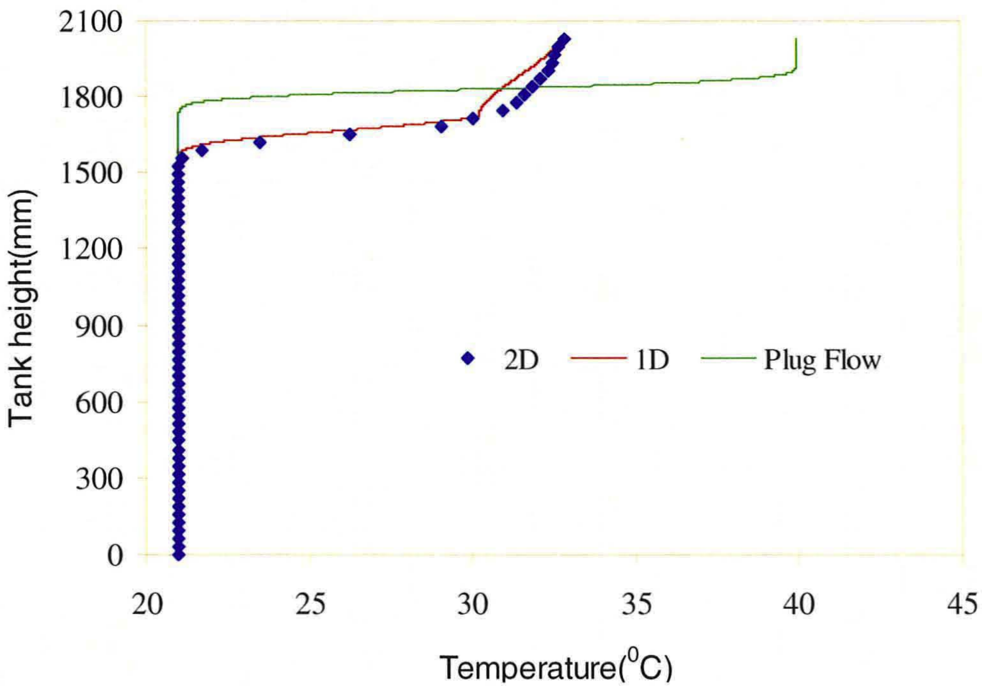

Figure 5.28: Temperature Distribution in the Tank at 35 Minutes- Case I.

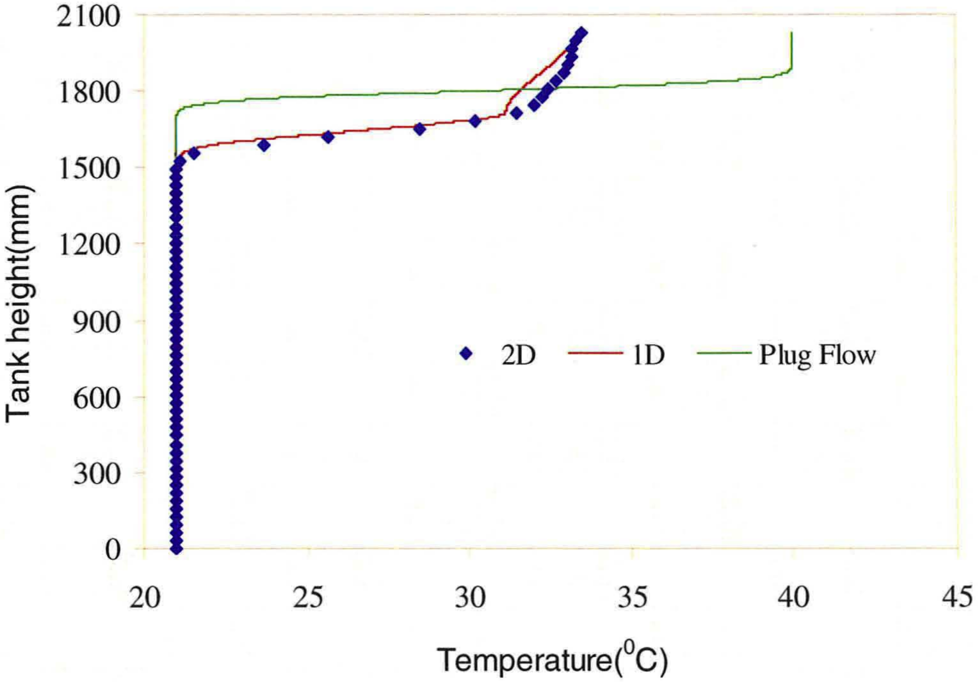

Figure 5.29: Temperature Distribution in the Tank at 40 Minutes- Case I.

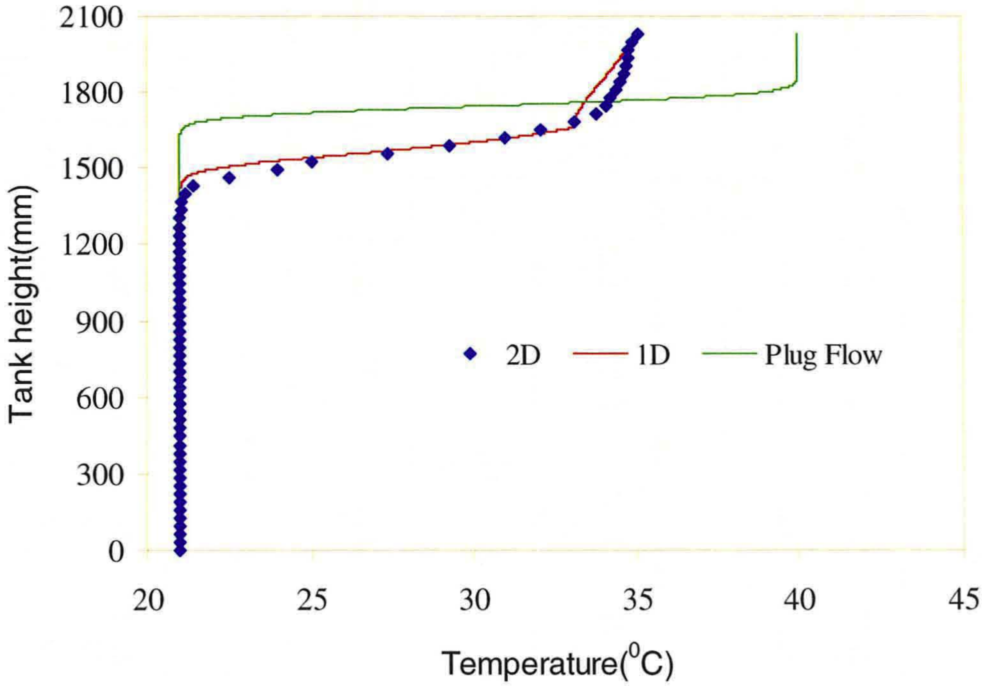

Figure 5.30: Temperature Distribution in the Tank at 55 Minutes- Case I.

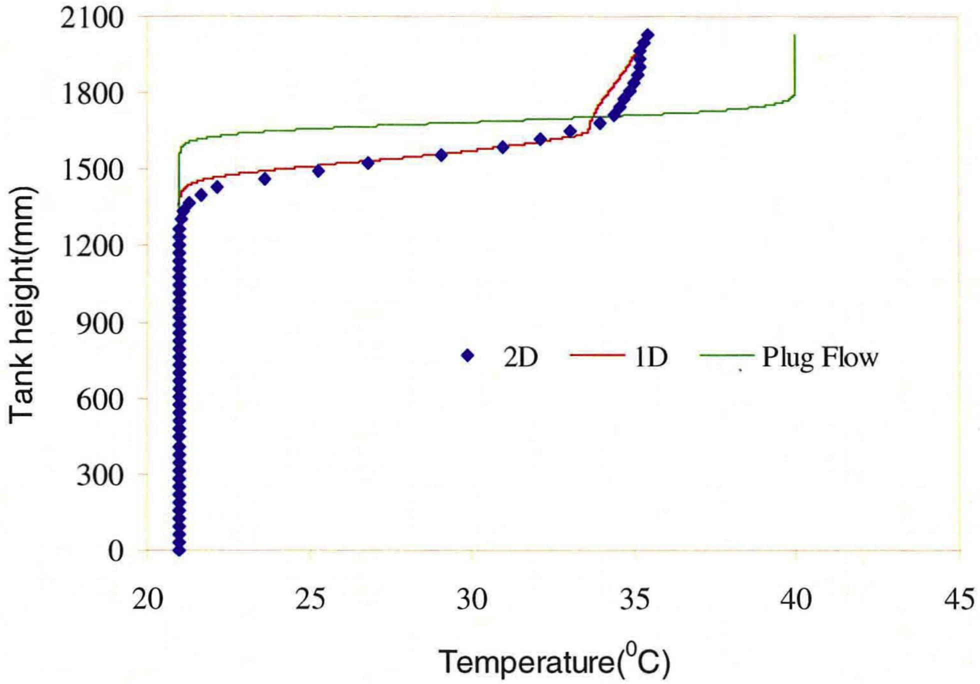

Figure 5.31: Temperature Distribution in the Tank at 60 Minutes- Case I.

CHAPTER 6

Closure

6.1 Summary and Conclusions

This thesis has been concerned with modelling the heat transfer and fluid flow in a thermal storage tank with a vertical inlet. The goal of the research was to use computational fluid dynamics to gain an understanding of the underlying flow physics in order to develop a simple 1D model for incorporation into system codes. The commercial CFD code ANSYS CFX - 11 was used in this work.

CFD results were validated by comparing the predictions with published experimental solutions of the vertical inlet SDHW systems. Two different vertical inlet systems were studied. A fixed inlet condition (i.e., constant temperature and mass flow rates) and unsteady conditions that simulate the tank interacting with a natural convection heat exchanger. Different turbulence models were considered and it was found that for the low inlet velocity case, the SST model without the turbulence buoyancy term in the turbulence equations gave good predictions of the temperature distribution inside the tank. While for the high inlet velocities all the three eddy viscosity based turbulence models: k-ε, k-ω, and SST, gave better prediction with the turbulence buoyancy model included. The use of second order or high resolution advection scheme gave better prediction when compared to the first order upwind.

A parametric study of the TST was performed by varying the inlet temperature, the inlet velocities and the diameter. The results revealed that the mixing mechanism in the fixed inlet condition and the varying inlet condition are similar. The result confirmed that the vertical inlet mixing is mainly dominated by the depth of penetration of the jet. The mixing occurs in the plume region of the negative buoyant plume. Outside of the plume region, the temperature is essentially constant in the radial direction and varies only axially. The parametric study also revealed that the depth of the penetration of the jet is only the function of the Richardson number and inlet pipe diameter. The mass entrainment inside the plume is a function of the Richardson number. The relationship between the eddy diffusivity in the jet affected region but outside the plume was also studied. It was found to be a function of the inlet Reynolds number and the Richardson number.

The relationships developed for the jet penetration depth, mass entrainment and the turbulence eddy diffusivity were used to develop a one dimensional system model for the TST using the energy equation. Predictions of temperature from the new one dimensional model were compared to two dimensional CFD results obtained using ANSYS CFX – 11. Good agreement was obtained. The new one dimensional model was much more computationally efficient than the 2D CFD approach with computational effort reduced by about two orders of magnitude.

6.2 Recommendations for Future works

- A similar CFD study can be performed for a system which is subjected to both charging and discharging.

- The physics of mixing will be entirely different for the horizontal inlet configuration. Therefore a similar study to develop simple physical models based on the real physics of the horizontal jet mixing is recommended.
- Mixing due to positive buoyant plume is more detrimental when compared to the negative buoyant plume. This type of mixing will occur when cool water compared to the fluid at the top of the tank, enters the TST and typically occurs for SDHW systems in late afternoon. CFD study of such system and development of a physical model is also recommended.

References

[1] C.A. Cruickshank. Evaluation of a stratified multi-tank thermal storage for solar heating applications. Queen's University. Ph.D Thesis, 2009.

[2] Y.M. Han, R.Z. Wang and Y.J. Dai. Thermal stratification within the water tank. *Renewable and Sustainable Energy Rev*, doi: 10.1016/j.rser.2008.03.001.

[3] J.M. Purdy, S.J.Harrison and P.H.Oosthuizen. Thermal evaluation of compact heat exchangers in a natural convection application. *Proceedings of the 11th IHTC International Heat Transfer Conference*, *Korea*, Vol. 6, 305-310, 1998.

[4] R. Shyu, J. Lin and L. Fang. Thermal analysis of stratified storage tanks. *Journal of Solar Energy Engineering*, 111:54–61, 1989.

[5] C.A. Cruickshank, S.J. Harrison. Experimental characterization of a natural convection heat exchanger for solar domestic hot water systems. *Proceedings of ISEC 2006 International Solar Energy Conference,* July 8-13, Denver, Colorado USA, 2006.

[6] D.J. Nizami, M.F. Lightstone, S.J. Harrison and C.A. Cruickshank. Simulation of the interaction of a solar domestic hot water tank system with a compact plate heat exchanger. *Proceedings of the Joint Conference of the Canadian Solar Building Research Network and Solar Energy Society of Canada Inc.*, 2008.

[7] K.G.T. Hollands and M.F. Lightstone. A review of low-flow, stratified-tank solar water heating systems. *Solar Energy*, 43(2):97–105, 1989.

[8] M.A. Rosen. The exergy of stratified thermal energy storages. *Solar Energy*, 71(3):173–185, 2000.

[9] V. Panthalookaran, W. Heidemann and H. Muller-Steinhagen. A new method of characterization for stratified thermal energy stores. *Solar Energy*, 81:1043–1054, 2007.

[10] L.F. Cabeza, A.He Castell and M. Medrano. Dimensionless parameters used to characterize water tank stratification. *International Energy Agency: Solar Heating and Cooling Programme,* Task 32: Advanced storage concepts for solar and low energy buildings, 2006.

[11] Z. Lavan and J. Thompson. Experimental study of thermally stratified hot water tanks, *Solar Energy*, Vol. 19, No. 5, 1977.

[12] B.J. Silwinski, A.R. Mech and R.S. Shih. Stratification in thermal storage during charging. *6th International Heat Transfer Conference, Toronto,* Vol. 4, pp. 149-54, 1978.

[13] Y.H. Zurigat, P.R. Liche and A.J. Ghajar. Influence of inlet geometry on mixing in thermocline thermal energy storage. *International Journal of Heat and Mass Transfer*, 34(1):115–125, 1991.

[14] Y.H. Zurigat, A.J. Ghajar and P.M. Moretti. Stratified thermal storage tank inlet mixing characterization. *Applied Energy*, 30:99–111, 1988.

[15] A.J. Ghajar and Y.H. Zurigat. Numerical study of the effect of inlet geometry on stratification in thermal energy storage. *Numerical Heat Transfer*, 19(A):65–83, 1991.

[16] M.W. Wildin and C.R. Truman. Performance of stratified vertical cylindrical thermal storage tanks, Part I: Scale model tank. *Journal of the Electrochemical Society*, 106(9):827–833, 1959.

[17] J.H. Davidson, D.A. Adams and J.A. Miller. A coefficient to characterize mixing in solar water storage tanks. *Journal of Solar Energy Engineering*, 116:94–99, 1994.

[18] D.E. Adams and J.H. Davidson. Tank stratification with a flexible manifold. *The 1993 American Solar Energy Society Annual Conference*, 1993.

[19] E. Hahne and Y. Chen. Numerical study of flow and heat transfer characteristics in hot water stores. *Solar Energy*, 64(1-3):9–18, 1998.

[20] H. Yoo and E.T. Pak. Analytical solutions to a one-dimensional finite-domain model for stratified thermal storage tanks. *Solar Energy*, 56(4):315–322, 1996.

[21] R.E. Spall. A numerical study of transient mixed convection in cylindrical thermal storage tanks. *International Journal of Heat and Mass Transfer*, 41(13):2003–2011,1998.

[22] Y. Mo and O. Miyatake. Numerical analysis of the transient turbulent flow field in a thermally stratified thermal storage water tank. *Numerical Heat Transfer, A,* 30, 649-667, 1996.

[23] L. Cai and W.E.Jr. Stewart. Turbulent buoyant flows into a two dimensional storage tank. *International Journal of Heat and Mass Transfer*, 36:4247–4256, 1993.

[24] J.Van Berkel, C.C.M. Rindt and A.A. Van Steenhoven. Modelling of two-layer stratified stores. *Solar Energy*, 67(1-3):65–78, 1999.

[25] C.K.Yee, F.C. Lai. Effects of a porous manifold on thermal stratification in a liquid storage tank. *Solar Energy*, 7(4):241–254, 2001.

[26] K.L. Guo and S.T. Wu. Numerical study of flow and temperature stratification in a liquid thermal storage tank. *J. Solar Energy Eng.* 107, 15-20, 1985.

[27] M.W. Wildin and C.R. Truman. Evaluation of stratified chilled water storage technique . Report EM-4352, Electric Power Research Institute, Palo Alto, CA, 1985.

[28] E. Anderson, S. Furbo. Thermal destratification in small standard solar tanks due to mixing during tapping. *ISES Solar World Congress 1999*, Jerusalem, Israel, Proceedings, pp. 1197-1206, 1999.

[29] S. Knudsen. Consumer's influence on the thermal performance of small SDHW systems-theoretical investigations. Proceedings, NorthSun 2001, Leiden, Holland, 2001.

[30] L.J. Shah and S. Furbo. Entrance effects in solar storage tanks. *Solar Energy*, 75:337–348, 2003.

[31] K.O. Homan. Internal entropy generation limits for direct sensible thermal storage. *Journal of Energy Resources Technology*, 125:85–93, 2003.

[32] Y. Jaluria and S.K. Gupta. Decay of thermal stratification in a water body for thermal energy storage. *Solar Energy,* Vol. 28, pp. 137-143, 1982.

[33] M.A. Abdoly and D. Rapp. Theoretical and experimental studies of stratified thermocline storage of hot water. *Energy Conversion Management*, 22:275–285, 1982.

[34] R. Shyu, J. Lin and L. Fang. Thermal analysis of stratified storage tanks. *Journal of Solar Energy Engineering*, 111:54–61, 1989.

[35] J.E.B. Nelson, A.R. Balakrishnan and S. Srinivasa Murthy. Experiments on stratified chilled-water tanks. *International Journal of Refrigeration*, 22:216–234, 1999.

[36] J.E.B. Nelson, A.R. Balakrishnan and S. Srinivasa Murthy. Parametric studies on thermally stratified chilled water storage systems. *Applied Thermal Engineering*, 19:89–115, 1999.

[37] J.E.B Nelson, A.R. Balakrishnan and S. Srinivasa Murthy. Transient analysis of energy storage in a thermally stratified water tank. *International Journal of Energy Research*, 22:867–883, 1998.

[38] C.W. Miller. Effect of a conducting wall on a stratified fluid in a cylinder, heat transfer and thermal control system. *Progress in Astronautics and Aeronautics*, Vol. 60, pp.190-208, 1977.

[39] C. Sherman, B.D. Wood and J. Mason. Effect of vertical wall conduction on temperature relaxation in thermally stratified liquid thermal storage tanks. *Sun II, Proceedings of The International Solar Energy Society Silver Jubilee Congress, Atlanta,* pp. 591-595, Pergamon Press, 1979.

[40] R.L. Cole and F.O. Bellinger. Thermally stratified tanks. *Journal of the Electrochemical Society*, 106(9):827–833, 1959.

[41] N.K. Ghaddar and A.M. Al-Maarafie. Study of charging of stratified storage tanks with finite wall thickness. *International Journal of Energy Research*, 21:411–427, 1997.

[42] M. F. Lightstone. A numerical study of thermal stratification in solar energy storage tanks. University of Waterloo, M.A.Sc Thesis, 1987.

[43] M.A. Al-Nimr. Temperature distribution inside a solar collector storage tank of finite wall thickness. *Journal of Solar Energy Engineering*, 115(9):112–116, 1993.

[44] A. Bouhdjar and A. Harhad. Numerical analysis of transient mixed convection flow in storage tank: influence of fluid properties and aspect ratios on stratification. *Renewable Energy*, 25:555–567, 2002.

[45] M.F. Lightstone, G.D. Raithby and K.G.T. Hollands. Numerical simulation of the charging of liquid storage tanks: Comparison with experiment. *Journal of Solar Energy Engineering*, 111:225–231, 1989.

[46] M. Shin, H. Kim, D. Jang, S. Lee, Y. Lee and H. Yoon. Numerical and experimental study on the design of a stratified thermal storage system. *Applied Thermal Engineering*, 24:17–27, 2004.

[47] R.D.C. Oliveski. A. Krenzinger and H.A. Vielmo. Comparison between model for simulation of hot water storage tanks. *Solar Energy*, 75:121–134, 2003.

[57] N. Nakahara, K. Sagara and M. Tsujimoto. Water thermal storage tank: Part 2 – Mixing model and storage estimation for temperature-stratified tanks. *Journal of the Electrochemical Society*, 106(9):371–, 1959.

[58] N. Atabaki and M. Bernier. A semi-empirical model for residential electric hot water tanks. *ASHRAE Transactions*, 111:159, 2005.

[59] S. Alizadeh. An experimental and numerical study of thermal stratification in a horizontal cylindrical solar storage tank. *Solar Energy*, 66(6):409–421, 1999.

[60] TRNSYS 13.1 User's Manual, 1990.

[61] R. Franke. Object-oriented modeling of solar heating systems. *Solar Energy* 60, 171-180, 1997.

[62] J.S. Caldwell and W.P. Bahnfleth. Identification of mixing effects in stratified chilled-water storage tanks by analysis of time series temperature data. *ASHRAE Transactions* 104(2):366-376, 1998.

[63] R.A. Pate. A thermal storage tank model for solar heating. Ph.D. Thesis, Utah State Univ., Logan, UT, 1977.

[64] G.F. Csordas, A.P. Brunger, K.G.T. Hollands and M.F. Lightstone. Plume entrainment effects in solar domestic hot water systems employing variable-flow-rate control strategies. *Solar Energy*, 49(6):497–505, 1992.

[65] W.C Reynolds. Computation of turbulent flows. *Annu. Rev. Fluid Mech*, Vol 8, pp 183-208, 1976.

[66] C.G Speziale. Analytical methods for the development of reynolds stress closures in turbulence. *Annu. Rev. Fluid Mech*, Vol 23, pp 107-157, 1991.

[67] J. Mathieu, J. Scott. An introduction to turbulent flows. Cambridge University Press, 1999.

[68] ANSYS CFX-11.0. 2007. Solver theory guidelines. *ANSYS, Inc.,* USA.

[69] T.J. Barth, and D.C Jesperson. The design and application of upwind schemes on unstructured meshes. *AIAA Paper* 89-0366, 1989.

[70] R.I. Leohrke and J.C. Holzer. Stratified thermal storage experiments. *Technical Report HT-TS793, Prepared for the Boeing Computer Services Company,* 1979.

APPENDIX A

Analysis of the Experimental Correlation

Figure A.1 compares the prediction of the flow rate using boundary condition *B2* (*2S5*) with the experiment. From the prediction of the flow rate, it is evident that as hot water is delivered to the TST, the hydrostatic pressure in the TST reduces with time, resulting in gradual decrease in the flow rate at the inlet. However, the correlations under-predict the flow rate by approximately 10 to 15%. Figure A.2 compares the predicted inlet temperature for the same simulation to the experiment. It can be observed that the prediction of the inlet temperature is in good agreement with the experiment. The under-prediction of the flow rate with the experimental correlation could be attributed to the fact that the correlations considered the hydrostatic pressure difference in the system and the inertia of the fluid which may have influenced the developed flow rate across the heat exchanger was neglected.

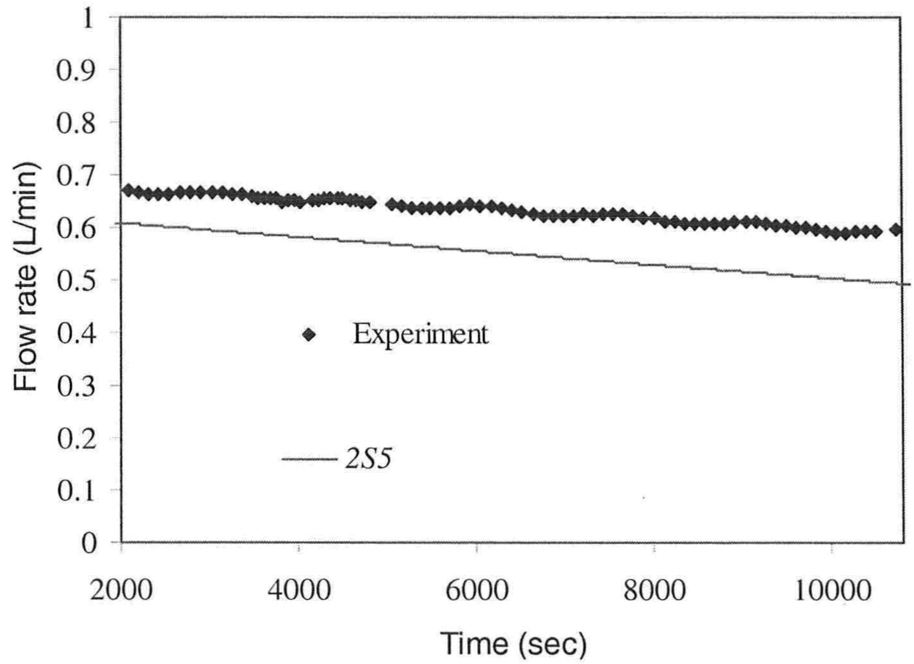

Figure A.1: Flow Rate Comparison Case II.

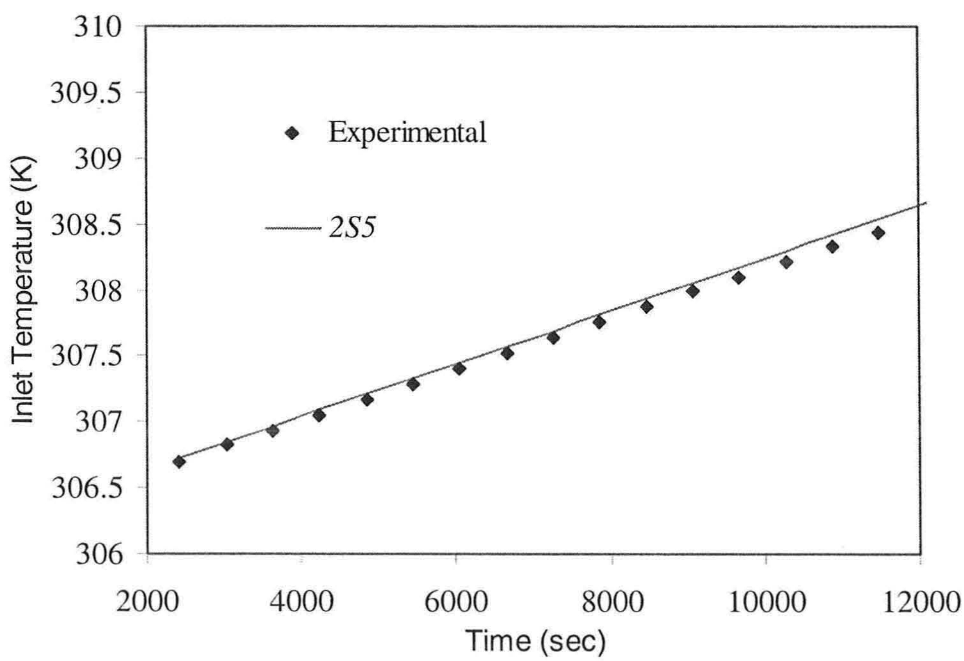

Figure A.2: Inlet Temperature Comparison Case II.

Appendix B

```
Program Tank

Implicit none

c***** Variable Declaration*************************************************

Double Precision C(4100),COF1(4100),COF2(4100),COF3(4100),
*      Dum(4100), TempDelta1(1,5), TnkTemp(4100,5)
Double Precision Accmtim, AcsDelta1, AcsDelta2, AcsDelta4, AlfPrm,
*      ConstA, Cp, Delta2, DeltaRegAvgTemp, DeltaRegTempWtCl, Diff1,
*      DifHtJtAndDelta, dt, dx, DiaPipe, DiaTnk, DmDelta3, g, HtTnk, HtJt, i6,
*      M11, MsflInlt, Msflplum, Re, Ri, Row, RowDeltaReg, SumTempOutDelta3,
*      TempDelta1Dmy, TempTnkInitl, TempWtCl, TimIntrvlWrt, TInlt,TnkVol,
*      Tout, RowInlt, TnkAvgTemp, TotTim, v2, v4, v22, v44, v444, v22a, Visc
Integer indx(4100)
Integer Delta2Np, DeltaNp, DeltaNpPrevTim,
*      DifCurntTimJtHtNpAndPrevTimJtHtNp, DifHtJtAndDeltaNp, i,
*      InltCondn, j, JtHtNp, JtHtNpDmy, k, Numeq, TimCntr, TnkSys, TotJtHt,
*      TotNpTnk, WrtCntr

c***** Result File**********************************************************

       open (1,File='Result.txt')

c***** Tank Geometry, Mesh Generation, Fluid Properties, Initialization and Model
Declaration****************************************************************

       Write(*,*)'Dia of Tank in Meters'
```

```
Read(*,*)DiaTnk
Write(*,*)'Length of Tank in Millimeters'
Read(*,*)HtTnk
Write(*,*)'No. of Nodes ='
Read(*,*)TotNpTnk
Write(*,*)'Time Step in sec'
Read(*,*)dt
Write(*,*)'Simulation Time in sec'
Read(*,*)TotTim
Write(*,*)'Time Intervals for Transient Result in sec'
Read(*,*)TimIntrvlWrt
Write(*,*)'Density of Water in Kg/m^3'
Read(*,*)Row
Write(*,*)'Specific Heat Capacity of Water in J/KgK'
Read(*,*)Cp
Write(*,*)'Dynamic Viscosity of Water in Ns/m^2'
Read(*,*)Visc
Write(*,*)'Gravitational Constant in m/sec^2'
Read(*,*)G
Write(*,*)'Modelling, Enter 3 for Plug Flow Model or,'
Write(*,*)'enter 1, if Inlet Pipe is submerged or,'
Write(*,*)'enter 2, Otherwise'
```

```
      Read(*,*)TnkSys
      If(TnkSys.eq.3)goto 1
      Write(*,*)'Dia of Inlet Pipe in Meters'
      Read(*,*)DiaPipe
      If(TnkSys.eq.1)then
      Write(*,*)'Length of Inlet Pipe Submerged in mm'
      Read(*,*)Delta2
      Else
      Delta2 = 20.0
      End If
      dx = HtTnk/TotNpTnk
      Delta2Np = Delta2/dx
      DifHtJtAndDelta = 20.0
      DifHtJtAndDeltaNp = DifHtJtAndDelta/dx
      AcsDelta1 = 3.141592654*(.060)**2
      AcsDelta2 = 3.141592654* ((DiaTnk/2.0)**2-(0.06)**2)
1     AcsDelta4 = 3.141592654*(DiaTnk/2.0)**2
      TnkVol = (AcsDelta4*HtTnk)/1000.0
      Write(*,*)'Initial Temperature in Tank In Kelvin'
      Read(*,*)TempTnkInitl
      If(TnkSys.eq.3)AcsDelta2=AcsDelta4
      Do 2, i = 1,TotNpTnk
```

```
      TnkTemp(i,1) = TempTnkInitl
2     End Do
      TempDelta1(1,1) = TempTnkInitl
      Tout = TempTnkInitl
      TnkAvgTemp = TempTnkInitl
      DeltaRegAvgTemp = TempTnkInitl
      TimCntr = 1
      WrtCntr = 1
c******Start of the transient loop******************************************
3     Do 17 j = 2,5
      Accmtim = TimCntr*dt
c******Further declaration of the inlet conditions*******************************
      If(TimCntr.eq.1)then
      Write(*,*)'Enter 1 for Fixed Inlet Condition'
      Write(*,*) 'or 2 for Variable Inlet Condition'
      Read(*,*)InltCondn
      End If
      If((InltCondn.eq.1).and.(TimCntr.eq.1))then
      Write(*,*)'Temperature at Inlet in Kelvin'
      Read(*,*)TInlt
      Write(*,*)'Mass Flow Rate in kg/sec'
      Write(*,*)0.008333*12.0
```

```
      Read(*,*)MsflInlt
      Elseif(InltCondn.eq.2)then
      TInlt = (0.0002*Accmtim)+306.2487
      MsflInlt = -(0.0000002110*Accmtim)+0.0105538841
      End If
c******Conditions for the Plug Flow Model ***********************************
      If(TnkSys.eq.3)then
      Msflplum = MsflInlt
      AlfPrm = 0.0
      DmDelta3 = 0.0
      Delta2Np = 5
      DeltaNp = 20
      TempDelta1(1,j) = TInlt
      goto 7
      End If
c******Modelling concept proposed in this work starts here*******************
c******Determination of the jet penetration depth****************************
      RowInlt = -0.0035868*((TInlt-273.15)**2)-
     *             (0.0670346*(TInlt-273.15))+1000.31
      If(TimCntr.ne.1)DeltaNpPrevTim = DeltaNp
      Re = (RowInlt*MsflInlt*DiaPipe)/(Visc*RowInlt*3.14*((DiaPipe/2)**2))
      RowDeltaReg = -0.0035868*((DeltaRegAvgTemp-273.15)**2)-
```

```
     *                  (0.0670346*(DeltaRegAvgTemp-273.15))+1000.31
          Ri = (abs(RowDeltaReg-RowInlt)*DiaPipe*g*(RowInlt**2)*
     *         (3.14**2)*(DiaPipe/2)**4)/((MsflInlt**2)*RowDeltaReg)
          If(TnkSys.eq.1)then
          HtJt = 25.33*Ri**(-0.618)
          Else
          HtJt = 21.59*Ri**(-0.4777)
          End If
          JtHtNp = (HtJt/dx)
          If(TimCntr.eq.1)goto 6
          If(JtHtNp.le.DeltaNpPrevTim)goto 6
          DifCurntTimJtHtNpAndPrevTimJtHtNp = JtHtNp-DeltaNpPrevTim
          Do 5 k = 1,DifCurntTimJtHtNpAndPrevTimJtHtNp
          JtHtNp = DeltaNpPrevTim+k
          JtHtNpDmy = JtHtNp
          TempWtCl = 0
          Do 4 I = DeltaNpPrevTim+1,JtHtNp
      TempWtCl = (TempWtCl+(TnkTemp(i,j-1)*(dx*AcsDelta4/1000.0)))
 4        End Do
          TempWtCl = (TempWtCl+(DeltaRegAvgTemp*
     *                (dx*DeltaNpPrevTim*AcsDelta4/1000.0)))
          DeltaRegAvgTemp = TempWtCl/((JtHtNp)*dx*AcsDelta4/1000.0)
```

```
      RowDeltaReg = -0.0035868*((DeltaRegAvgTemp-273.15)**2)-
     *               (0.0670346*(DeltaRegAvgTemp-273.15))+1000.31
      Ri = (abs(RowDeltaReg-RowInlt)*DiaPipe*g*(RowInlt**2)*(3.14**2)*
     *     (DiaPipe/2)**4)/((MsflInlt**2)*RowDeltaReg)
      If(TnkSys.eq.1)then
      HtJt = 25.33*Ri**(-0.618)
      Else
      HtJt = 21.59*Ri**(-0.4777)
      End If
      JtHtNp = (HtJt/dx)
      If(JtHtNp.le.JtHtNpDmy)goto 6
5     End Do
c******Determination of the eddy diffusivity ********************************
6     ConstA = .0016*Re-.8424
      AlfPrm = ConstA*Ri**(-0.29)
      TempDelta1(1,j) =TempDelta1(1,j-1)
      If(TnkSys.eq.1)then
      DeltaNp = JtHtNp+DifHtJtAndDeltaNp+Delta2Np
      Else
      DeltaNp = JtHtNp+DifHtJtAndDeltaNp
      End If
c******Determination of the mass flow entrainment****************************
```

```
      RowDeltaReg = -0.0035868*((TempDelta1(1,j-1)-273.15)**2)-
     *             (0.0670346*(TempDelta1(1,j-1)-273.15))+1000.31
      Ri = (abs(RowDeltaReg-RowInlt)*DiaPipe*g*(RowInlt**2)*(3.14**2)*
     *      (DiaPipe/2)**4)/((MsflInlt**2)*RowDeltaReg)
      Msflplum = 1.288*Ri**(-0.2784)*MsflInlt
      DmDelta3 = (Msflplum-MsflInlt)/(DeltaNp-Delta2Np)
      DmDelta3 = (Msflplum-MsflInlt)/(DeltaNp-Delta2Np)
      Write(13,*)'DeltaNp',DeltaNp,Ri,RowDeltaReg,DeltaRegAvgTemp
      If(DeltaNp.EQ.Delta2Np)PAUSE
c*****Determination of the terms in the discretized equation*********************
7     v2 = ((0.6069/(row*cp))+(0000000.0))*row*AcsDelta4
      v22 = ((0.6069/(row*cp))+(AlfPrm/1000000.0))*row*AcsDelta2
      v22a = ((0.6069/(row*cp))+(AlfPrm/1000000.0))*row*AcsDelta2
      v4 = (row*AcsDelta4*(dx/1000.0)**2)/dt
      v44 = (row*AcsDelta1*((DeltaNp*dx)/1000.0)**2)/dt
      v444 = (row*AcsDelta2*(dx/1000.0)**2)/dt
c*****Formation of the constant terms matrix**********************************
8     numeq = TotNpTnk
      C(1) = v444*TnkTemp(1,j-1)+(Msflplum*(dx/1000.0)*TempDelta1(1,j))
      Do 9 I = 2,numeq
      If(i.le.DeltaNp)then
      C(i) = v444*TnkTemp(i,j-1)
```

```
      Else
      C(i) = v4*TnkTemp(i,j-1)
      End If
9     End Do
      i6 = 0.0
c*****Formation of Co-efficient tridiagonal matrix*****************************
      Do 10 I = 1,numeq
      If(i.eq.1)then
      COF1(i) = v444+Msflplum*(dx/1000.0)+v22
      COF3(i) = -v22
      Elseif((i.gt.(1)).and.(i.le.(Delta2Np)))then
      COF1(i) = v444+((Msflplum-(i6*DmDelta3))*
     *            (dx/1000.0))+(2*v22)
      COF2(i) = -(((Msflplum-(i6*DmDelta3))*(dx/1000.0))+v22)
      COF3(i) = -v22
      Elseif((i.gt.(Delta2Np)).and.(i.lt.(DeltaNp/2)))then
      COF1(i) = v444+((Msflplum-(i6*DmDelta3))*
     *            (dx/1000.0))+(2*v22)
      COF2(i) = -(((Msflplum-(i6*DmDelta3))*(dx/1000.0))+v22)
      COF3(i) = -v22
      Elseif(i.eq.(DeltaNp/2))then
      COF1(i) = v444+((Msflplum-(i6*DmDelta3))*
```

```
     *           (dx/1000.0))+(v22a+v22)
        COF2(i) = -(((Msflplum-(i6*DmDelta3))*(dx/1000.0))+v22)
        COF3(i) = -v22a
        Elseif((i.gt.(DeltaNp/2)).and.(i.lt.(DeltaNp)))then
        COF1(i) = v444+((Msflplum-(i6*DmDelta3))*
     *           (dx/1000.0))+(2*v22a)
        COF2(i) = -(((Msflplum-(i6*DmDelta3))*(dx/1000.0))+v22a)
        COF3(i) = -v22a
        Elseif(i.eq.DeltaNp)then
        COF1(i ) = v444+((Msflplum-(i6*DmDelta3))*
     *           (dx/1000.0))+(v22a+v22a)
        COF2(i) = -(((Msflplum-(i6*DmDelta3))*(dx/1000.0))+v22a)
        COF3(i) = -v22a
        Elseif(i.eq.DeltaNp+1)then
        COF1(i) = v4+(MsflInlt*(dx/1000.0))+(v22a+v2)
        COF2(i) = -(MsflInlt*(dx/1000.0)+v22a)
        COF3(i) = -v2
        Elseif((i.gt.(DeltaNp+1)).and.(i.lt.numeq))then
        COF1(i) = v4+(MsflInlt*(dx/1000.0))+(2*v2)
        COF2(i) = -(MsflInlt*(dx/1000.0)+v2)
        COF3(i) = -v2
        Elseif(i.eq.numeq)then
```

```
      COF1(i) = v4+(MsflInlt*(dx/1000.0))+v2
      COF2(i) = -(MsflInlt*(dx/1000.0)+v2)
      End If
      If(i.gt.(Delta2Np))i6 = i6+1.0
10    End Do
c*****Solution for the tridiagonal martrix [72]**********************************
      If(COF1(1).eq.0.0)pause
      M11 = COF1(1)
      TnkTemp(1,j) = C(1)/M11
      Do 11 i = 2,numeq
      Dum(i) = COF3(i-1)/M11
      M11= COF1(i)-COF2(i)*Dum(i)
      If(M11.eq.0.0)pause
      TnkTemp(i,j) = (C(i)-COF2(i)*TnkTemp(i-1,j))/M11
11    End Do
      Do 12 i= numeq-1,1,-1
      TnkTemp(i,j) = TnkTemp(i,j)-Dum(i+1)*TnkTemp(i+1,j)
12    End Do
c*****Determination of the temperature advected into the region delta 1************
      If(TnkSys.ne. 3)then
      SumTempOutDelta3 = 0.0
      Do 13 i = (Delta2Np)+1,DeltaNp
```

```
      SumTempOutDelta3 = SumTempOutDelta3+TnkTemp(i,j)
13    End Do
c*****Determination of the temperature in the region delta 1*********************
      TempDelta1Dmy = (MsflInlt*TInlt+DmDelta3*SumTempOutDelta3+
     *               (Msflplum*TempDelta1(1,j-1)-MsflInlt*TInlt-DmDelta3
     *               *SumTempOutDelta3)*exp(-Msflplum*dt/(v44*dt)))/
     *               Msflplum
      Diff1 = TempDelta1Dmy-(TempDelta1(1,j))
      If(abs(Diff1).ge.0.000005)then
      TempDelta1(1,j) = TempDelta1Dmy
      goto 8
      End If
c*****Determination of the avg. temp. in the tank and in the delta region*************
      TempWtCl = 0
      DeltaRegTempWtCl = 0
      Do 14 i = 1,TotNpTnk
      If(i.le.DeltaNp)then
      TempWtCl = (TempWtCl+(TnkTemp(i,j)*(dx*AcsDelta2/1000.0)))
      If(TnkSys.eq.2)then
      DeltaRegTempWtCl = (DeltaRegTempWtCl+
     *                  (TnkTemp(i,j)*(dx*AcsDelta2/1000.0)))
      Elseif((TnkSys.eq.1).and.(i.gt.Delta2Np))then
```

```
      DeltaRegTempWtCl = (DeltaRegTempWtCl+(TnkTemp(i,j)*
     *                         (dx*AcsDelta2/1000.0)))
      End If
      Else
      TempWtCl = (TempWtCl+(TnkTemp(i,j)*(dx*AcsDelta4/1000.0)))
      End If
14    End Do
      TempWtCl = (TempWtCl+(TempDelta1(1,j)*
     *                 (DeltaNp*dx*AcsDelta1/1000.0)))
      TnkAvgTemp =TempWtCl/TnkVol
      If(TnkSys.eq.1)then
      DeltaRegTempWtCl = (DeltaRegTempWtCl+(TempDelta1(1,j)*
     *                         ((DeltaNp-Delta2Np)*dx*AcsDelta1/1000.0)))
      DeltaRegAvgTemp = (DeltaRegTempWtCl/
     *                         ((DeltaNp-Delta2Np)*dx*AcsDelta4/1000.0))
      Else
      DeltaRegTempWtCl = (DeltaRegTempWtCl+(TempDelta1(1,j)*
     *                         ((DeltaNp)*dx*AcsDelta1/1000.0)))
      DeltaRegAvgTemp = (DeltaRegTempWtCl/
     *                         ((DeltaNp)*dx*AcsDelta4/1000.0))
      End If
      End If
```

```
      TimCntr = TimCntr+1
c*****Determination of the condition for the result output************************
      If(Accmtim.eq.TimIntrvlWrt*WrtCntr)then
      Write(1,*) 'Accmtim',Accmtim
      Write(1,*)0,TnkTemp(1,j)
      Do 15 i = 1,TotNpTnk
      Write(1,*)(i)*dx,TnkTemp(i,j)
15    End Do
      WrtCntr = WrtCntr+1
      End If
      If(Accmtim.ge.TotTim)exit
      If(j.eq.5)then
      Do 16 I = 1,TotNpTnk
      TnkTemp(i,1) = TnkTemp(i,j)
16    End Do
      If(TnkSys.ne.3)then
      TempDelta1(1,1) = TempDelta1(1,j)
      End If
      End If
17    End Do
      If(Accmtim.lt.TotTim)goto 3
      End
```

APPENDIX C

Examination of Grid and Time Step Dependence for One Dimensional Model

For the purpose of grid independence test, the number of nodes in the domains was doubled. Domain for Case I had 4064 nodes and Case II had 2760 nodes. For time step independence, the time step of 0.5 second was set for both cases, with 2032 grids for Case I and 1380 grids for Case II. Figures C.1 to C.6 show the results for Case II and figures C.7 to C.14 show the results for Case I at different time intervals. The legend, 1D represents the base case with 1380 grids for Case II and with 2032 grid for Case I with time step of 1 second in the respective graphs.

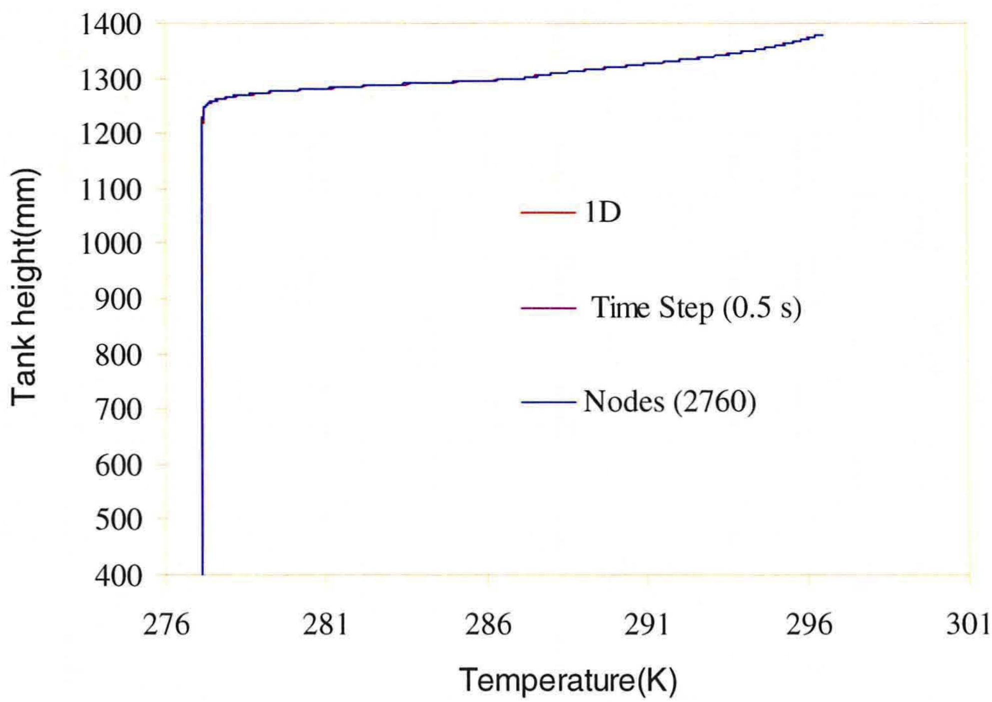

Figure C.1: Temperature Distribution in the Tank at 16 Minutes- Case II.

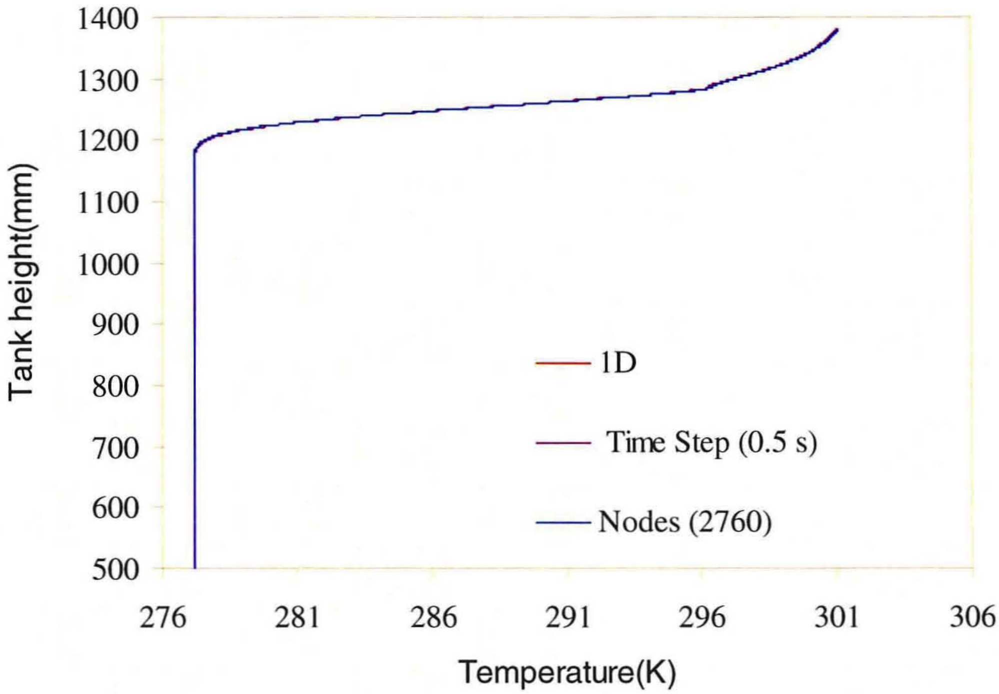

Figure C.2: Temperature Distribution in the Tank at 30 Minutes- Case II.

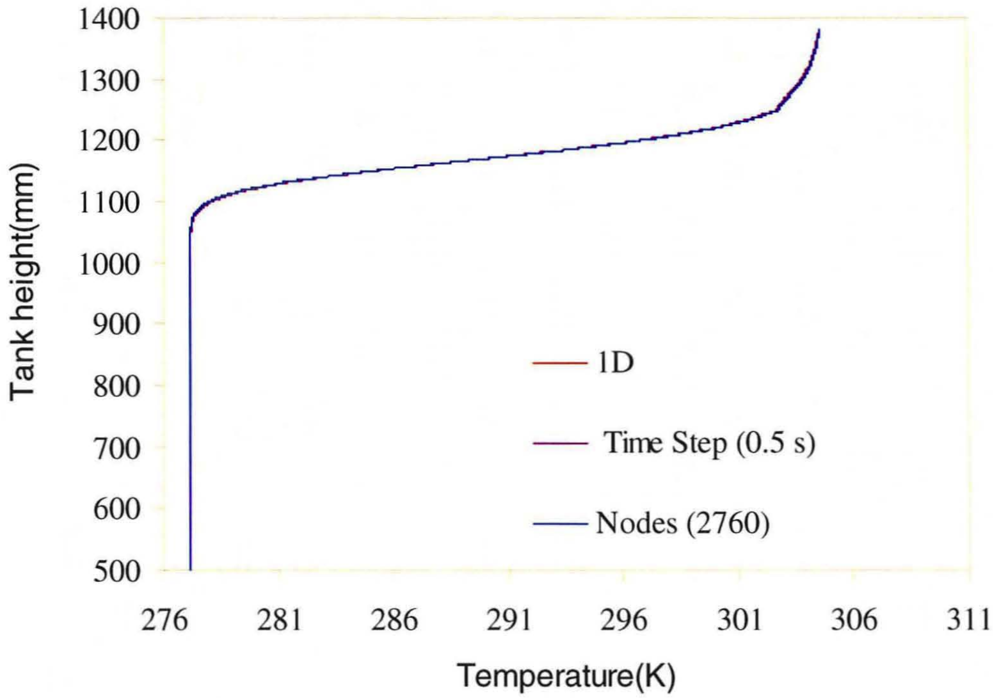

Figure C.3: Temperature Distribution in the Tank at 60 Minutes- Case II.

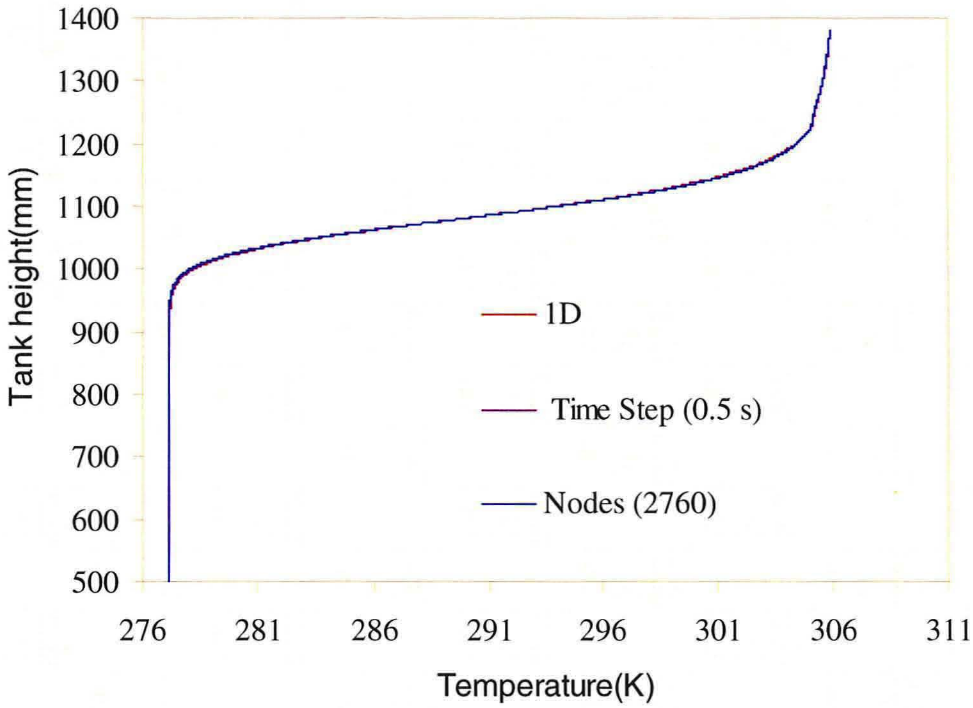

Figure C.4: Temperature Distribution in the Tank at 90 Minutes- Case II.

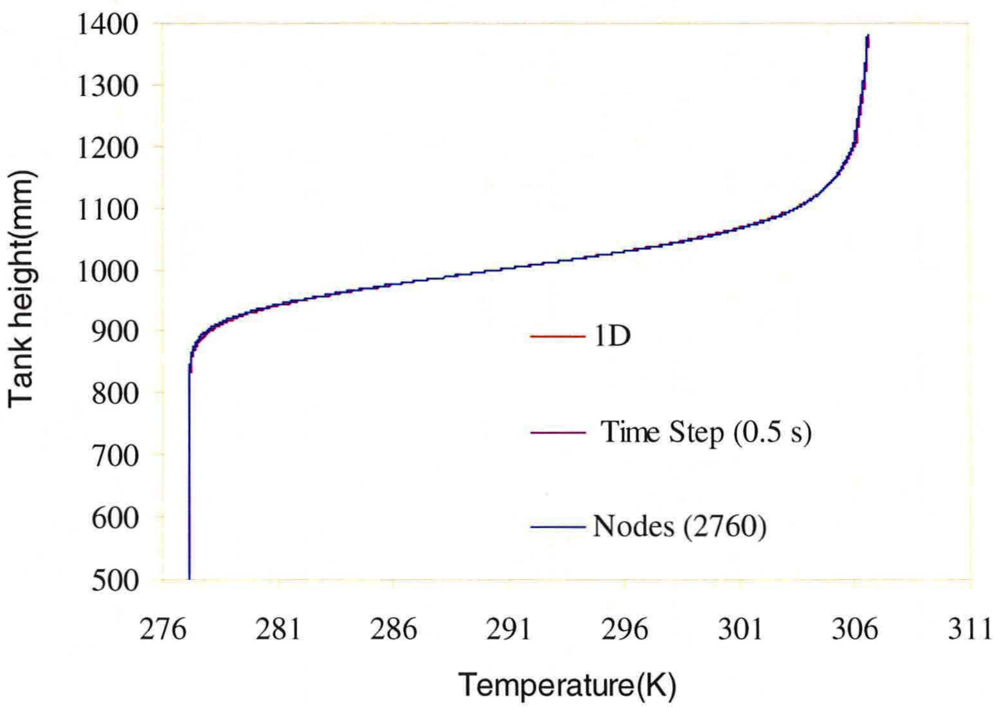

Figure C.5: Temperature Distribution in the Tank at 120 Minutes- Case II.

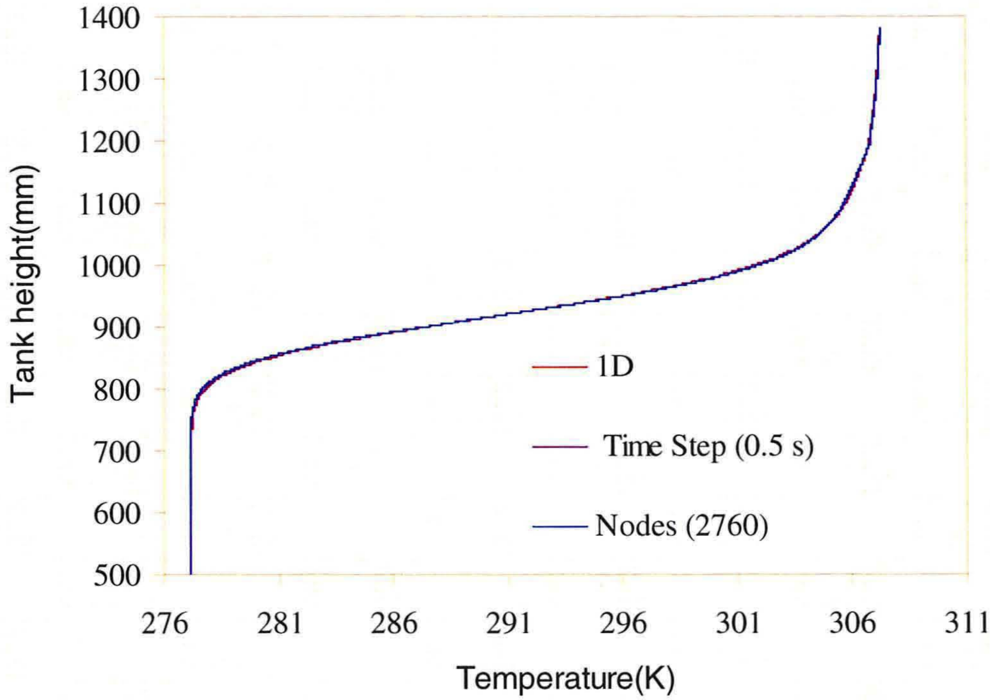

Figure C.6: Temperature Distribution in the Tank at 150 Minutes- Case II.

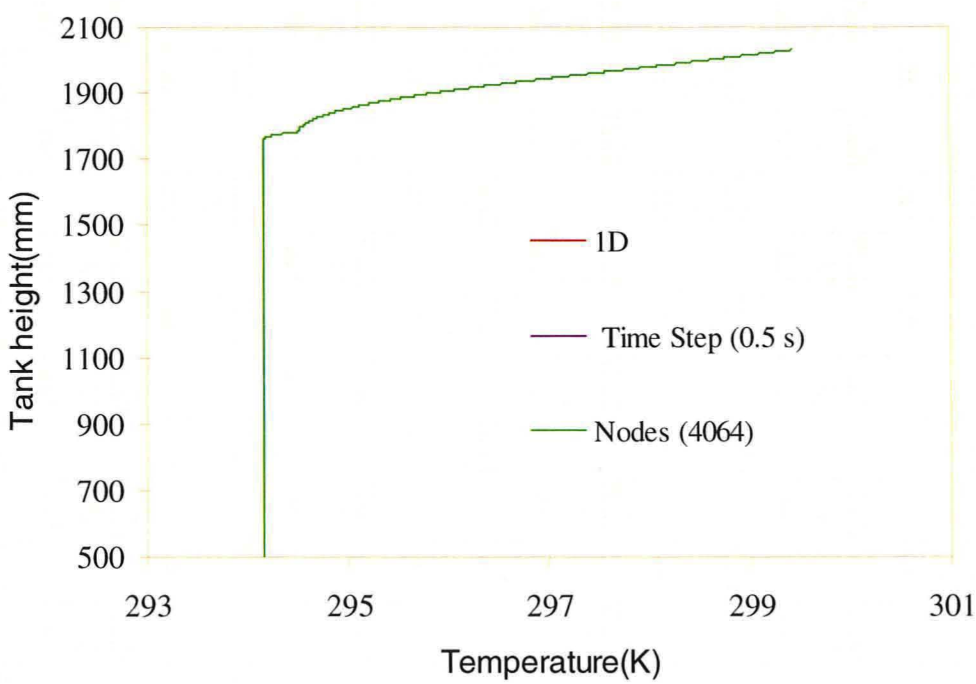

Figure C.7: Temperature Distribution in the Tank at 5 Minutes- Case I.

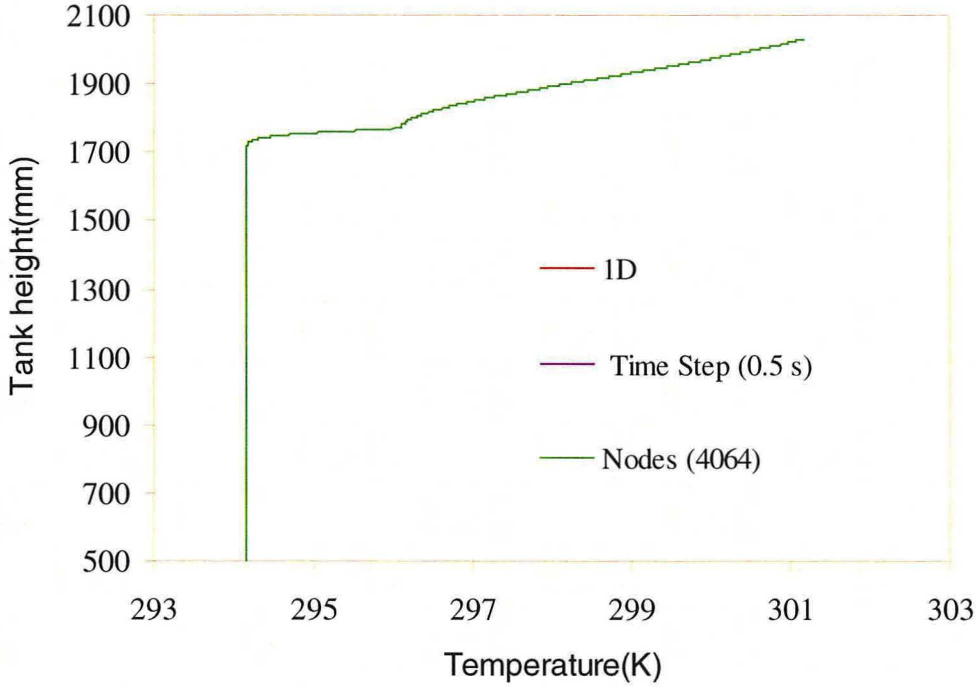

Figure C.8: Temperature Distribution in the Tank at 10 Minutes- Case I.

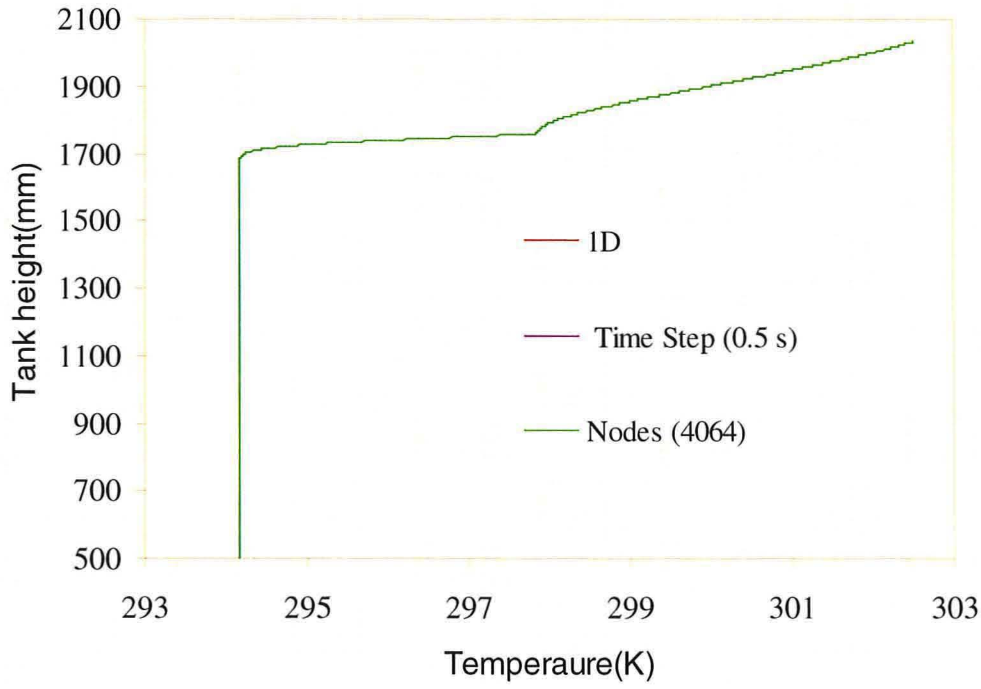

Figure C.9: Temperature Distribution in the Tank at 15 Minutes- Case I.

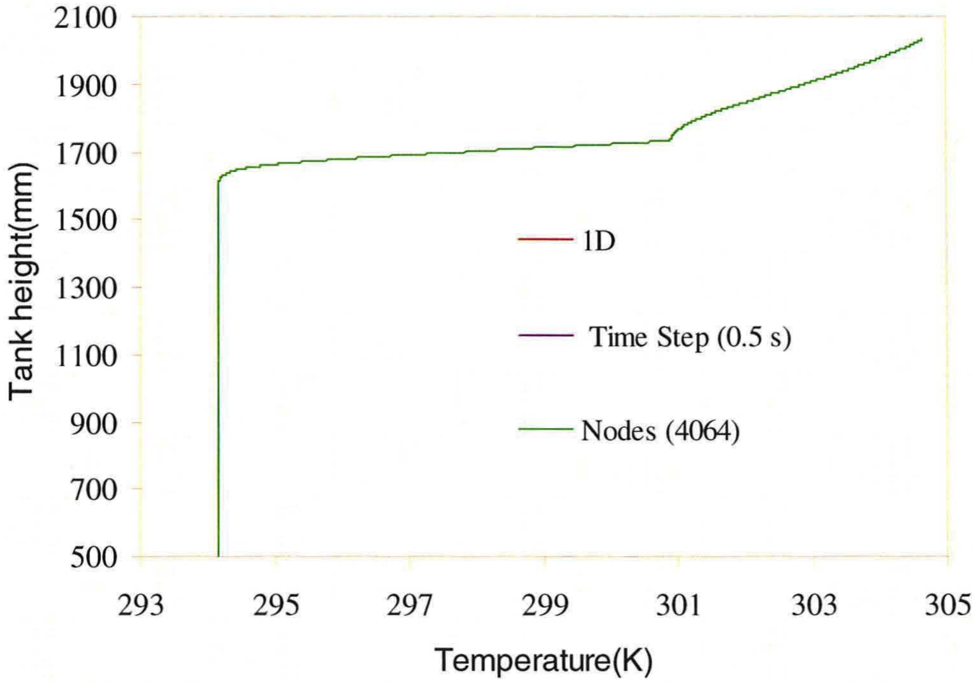

Figure C.10: Temperature Distribution in the Tank at 25 Minutes- Case I.

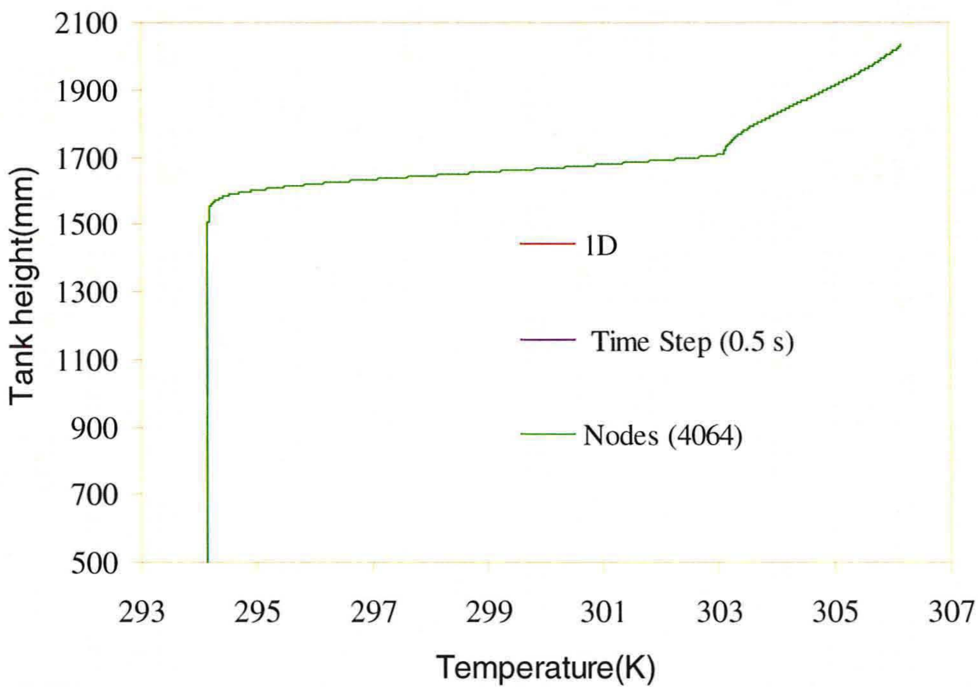

Figure C.11: Temperature Distribution in the Tank at 35 Minutes- Case I.

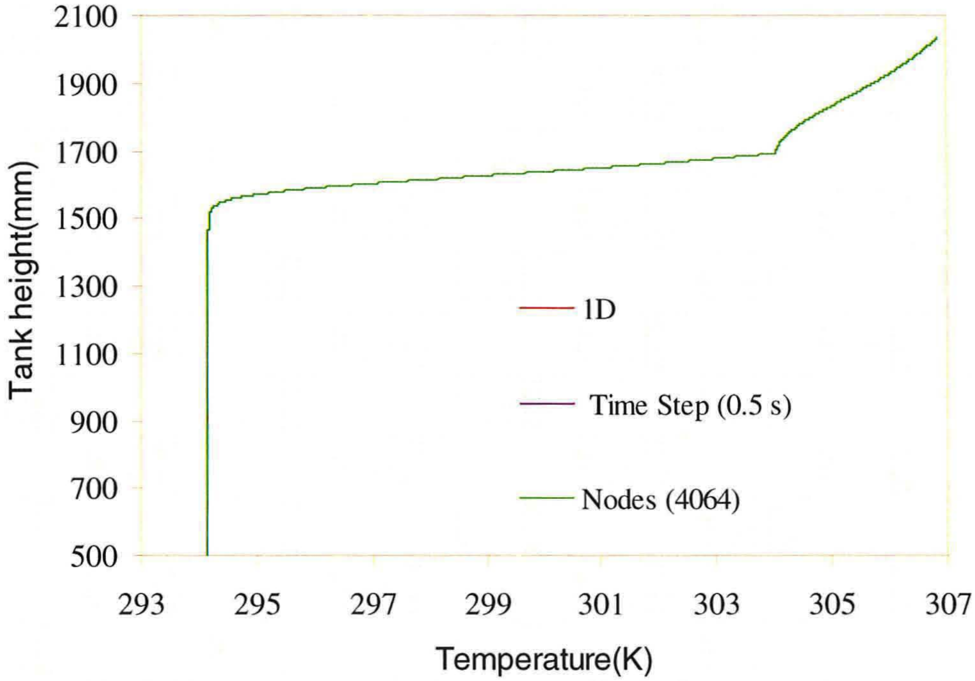

Figure C.12: Temperature Distribution in the Tank at 40 Minutes- Case I.

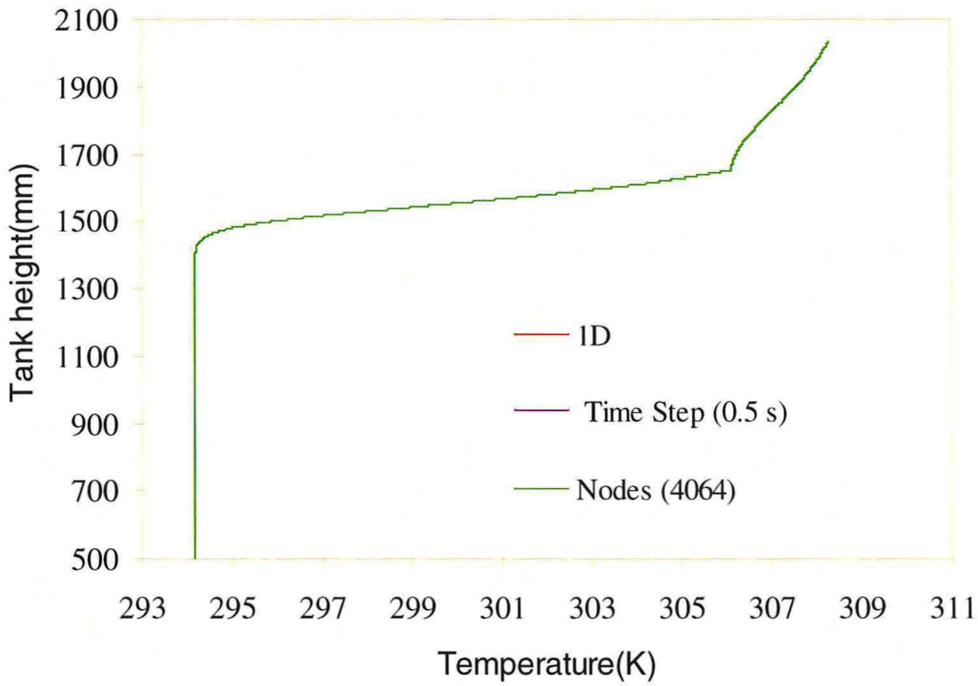

Figure C.13: Temperature Distribution in the Tank at 55 Minutes- Case I.

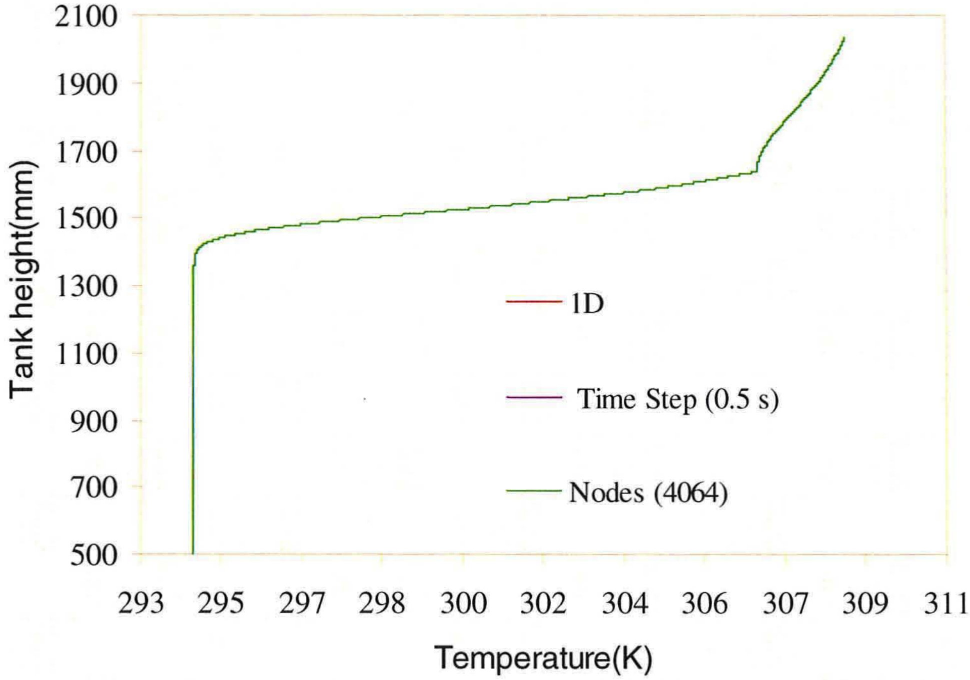

Figure C.14: Temperature Distribution in the Tank at 60 Minutes- Case I.